Title

A MEASUREMENT OF THE COSMIC BACKGROUND RADIATION TEMPERATURE AT 3.3 mm WAVELENGTH

Author

Witebsky, C.

Publication Date

1985-05-01

Lawrence Berkeley Laboratory
UNIVERSITY OF CALIFORNIA

Physics Division

A MEASUREMENT OF THE COSMIC BACKGROUND RADIATION TEMPERATURE AT 3.3 mm WAVELENGTH

C. Witebsky
(Ph.D. Thesis)

May 1985

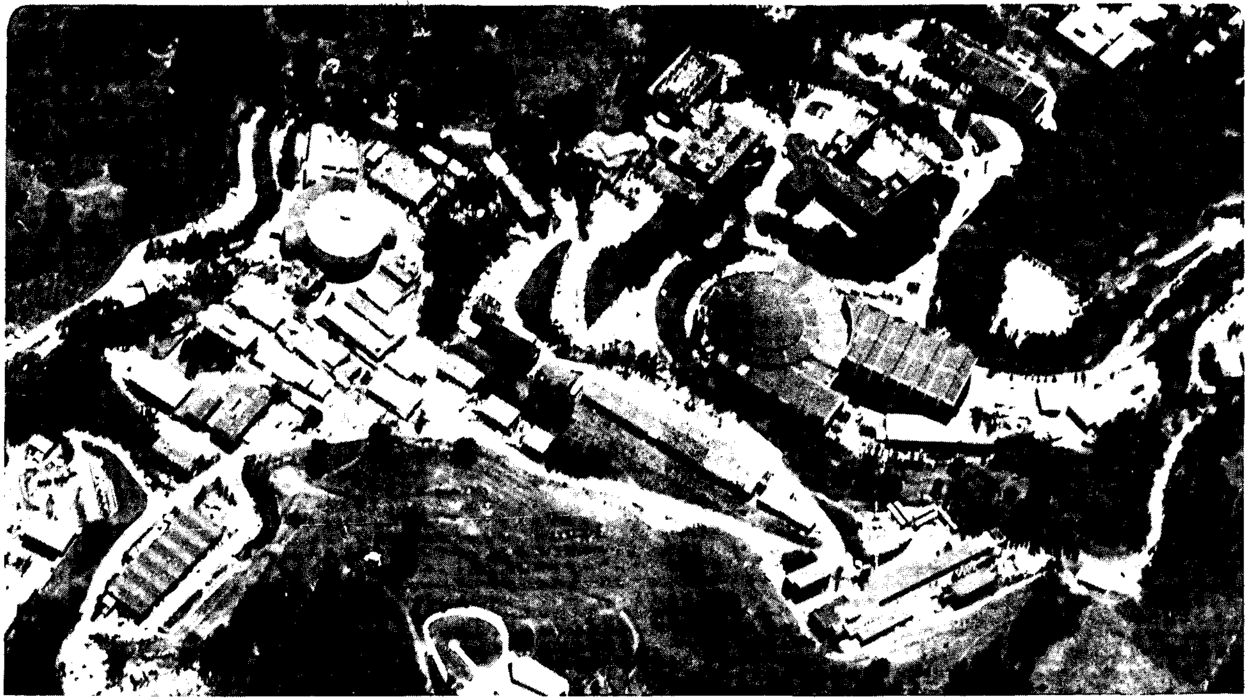

Prepared for the U.S. Department of Energy under Contract DE-AC03-76SF00098

LBL-18746

A MEASUREMENT OF THE COSMIC BACKGROUND RADIATION TEMPERATURE AT 3.3 mm WAVELENGTH

Chris Witebsky
(Ph.D. Thesis)

Lawrence Berkeley Laboratory
University of California
Berkeley, California 94720

May 1985

This work was supported by the Director, Office of Energy Research, Division of High Energy Physics of the Office of High Energy and Nuclear Physics of the United States Department of Energy under Contract Number DE-AC03-76SF00098 and NSF Grants PHY80-15694 and AST 800737.

A Measurement of the Cosmic Background Radiation Temperature at 3.3 mm Wavelength

Chris Witebsky

Abstract

Measurements of the cosmic background radiation (CBR) at 3.3 mm wavelength (90 GHz) have yielded a brightness temperature of 2.57 K with a 1σ uncertainty of ± 0.12 K. The observations were made from the Barcroft Laboratory of the White Mountain Research Station, at an altitude of 3800 m, initially on 5 and 6 July 1982 and again on 4, 5, and 6 September 1983, as part of a program to measure the spectrum of the CBR at five wavelengths from 12.0 cm to 3.3 mm (Smoot *et al.* 1985; Smoot, De Amici, Levin, and Witebsky 1985). The weighted mean of the temperature measurements at all five wavelengths is 2.72 ± 0.04 K.

The instrument used for the 3.3-mm measurements is a differential, dual-antenna, Dicke-switched, superheterodyne radiometer with an RF bandwidth of 1.9 GHz and a sensitivity of 125 mK/$\sqrt{\text{Hz}}$. The radiometer is mounted on bearings which allow it to rotate. Either antenna can view a large, liquid-helium-cooled absolute reference load while the other antenna views the zenith. The antenna temperature of the reference load, 2.083 ± 0.037 K, is added to the measured zenith/cold-load temperature difference to yield the zenith antenna temperature, typically 9 to 12 K. The atmospheric contribution to the zenith temperature is measured by means of zenith scans.

Simultaneous zenith scans at 9.1 mm and 3.3 mm have been used to check the atmospheric models of Waters (1976) and Liebe (1981; 1985). Neither model predicts the correct relationship between atmospheric emission at 9.1 mm and 3.3 mm.

When our results are combined with other measurements of the CBR temperature, including recent measurements by Meyer and Jura (1985) and Peterson, Richards, and Timusk (1985) but excluding the results of Woody and Richards (1981), the resulting spectrum is consistent with a 2.72 ± 0.02 K blackbody. When the combined data are fit to a Bose-Einstein spectrum, they set a 1σ upper limit on the chemical potential μ_0 of 4×10^{-3} if the universe is flat $[\Omega(H/50\ \text{km/sec/Mpc})^2 = 1]$, or less if it is open. The combined data also restrict the Compton-distortion parameter u to a value less than 4×10^{-3} to 7×10^{-3} at the 68% confidence level.

For Valeria Evans,

without whose love and support I might never have finished.

There is a theory which states that if ever anyone discovers exactly what the Universe is for and why it is here, it will instantly disappear and be replaced by something even more bizarre and inexplicable.

There is another which states that this has already happened.

—Douglas Adams,
The Hitchhiker's Guide to the Galaxy

Contents

List of Figures

List of Tables

Chapter 1

Introduction

The origin, history, and fate of the universe are subjects that have long fascinated mankind. Speculations about the universe have existed for millenia, but firm evidence on the subject has been meager. For this reason, those few clues that do exist about the nature of the early universe are scrutinized with great care. Among the most important of these is the cosmic background radiation, or CBR, a nearly isotropic radiation field in the microwave and far-infrared regions of the electromagnetic spectrum with a spectrum closely approximating that of a blackbody at 2.7 Kelvins. This radiation, believed to be the redshifted remnant of thermal radiation given off by hot material soon after the Big Bang, is one of the very few surviving indicators of the physical conditions of that early epoch.

1.1 Cosmology and the Hot Big Bang

1.1.1 Big-Bang Cosmology

Our understanding of the universe has progressed steadily since the time of Copernicus, but it was not until the early part of this century that cosmology in the modern sense began. The first clue as to the true scale of the cosmos came in 1923, when Edwin Hubble observed Cepheid variable stars in the M31 spiral nebula in Andromeda (Hubble 1925). From the period-luminosity relationship for Cepheids, Hubble was able to obtain a distance to the nebula, proving for the first time that M31 and other, similar spiral nebulae were not members of our galaxy but instead were galaxies themselves.

During the next few years, Hubble made systematic measurements of the redshifts of distant galaxies in order to study the distribution of their radial velocities. even more important contribution to observational cosmology. The redshift parameter z is a measure of the fractional difference between the wavelength of electromagnetic radiation when it is emitted from its source and the wavelength of the same radiation when viewed by an observer. It is defined by the equation:

$$z \equiv \frac{\lambda_0 - \lambda_e}{\lambda_e} ,$$

or equivalently

$$\frac{\nu_e}{\nu_0} = \frac{\lambda_0}{\lambda_e} = 1 + z , \tag{1.1}$$

where λ_e and λ_0 are the wavelengths of the emitted and observed radiation, and ν_e and ν_0 are the corresponding frequencies. Redshifts may result from the Doppler effect: Radiation from objects receding at a velocity v is redshifted by an amount

$$\begin{aligned} z &= \frac{[1-(v/c)^2]^{1/2}}{1-(v/c)} - 1 \\ &\simeq \frac{v}{c} \qquad\qquad (v << c) \end{aligned} \tag{1.2}$$

where c is the speed of light.

Hubble was able to show that on the average, the recessional velocity of a galaxy as viewed from our reference frame is linearly proportional to its distance, obeying the equation $v = H_0 s$, s being the distance to the galaxy. His measured value of the proportionality constant (now known as the Hubble parameter, or H_0) was approximately 500 km/sec/Mpc (Hubble 1929). Although the original value of H_0 is now known to be high by a factor of five to ten, the nearly linear relationship between galactic distance and recessional velocity has been verified by many observers.

Concurrent with these discoveries were developments in theoretical physics that helped to put them into perspective. Einstein's development of general relativity stimulated cosmologists to devise dynamical models of the universe compatible with observations that satisfied the Einstein field equations. The set of solutions most commonly used in modern cosmological theories were originally derived by A. Friedmann. These Friedmann models are the solutions to Einstein's field equations without a cosmological constant which satisfy the Cosmological Principle, which states that on large scales the universe is homogeneous and isotropic. This simplifying assumption is well justified by observations of the distribution of distant galaxies, and on an even larger scale by the observed isotropy of the cosmic background radiation.

The dynamics of the universe are governed in the Friedmann model by the equation:

$$\dot{R}^2 + Kc^2 = \frac{8\pi G}{3}\rho R^2 \tag{1.3}$$

(Weinberg 1972, § 15.3) where K is proportional to the difference between the density of gravitational and kinetic energy (positive, negative, or zero), G is the gravitational constant, $R(t)$ is the cosmic scale parameter, and ρ, the effective mass density, is the sum of ρ_M, the density of ordinary matter, and ρ_R, the equivalent mass density due to the thermal and kinetic energies of massive particles and photons.

The cosmic scale parameter $R(t)$, as its name implies, is a measure of the scale of the universe. The distance s between two points comoving with the overall motion of the universe is approximately equal to $R(t)r$, where r is the distance between the points in comoving (time-independent) coordinates. Their velocity of separation v is thus equal to $\dot{R}r$, proportional to their separation r. Since $r \simeq s/R$, their separation velocity can be expressed in non-comoving coordinates as

$$v \simeq \frac{\dot{R}}{R}s\,, \tag{1.4}$$

which is simply Hubble's relationship with H_0 set equal to $\dot{R}/R$. This relationship in fact defines H_0:

$$H_0 \equiv \frac{\dot{R}_0}{R_0}\,,$$

where R_0 and $\dot{R}_0$ are the present value of the scale parameter and its time derivative. At large redshifts ($z \gtrsim 1$) the simple linear relationships of equations (1.2) and (1.4) break down and the meanings of velocity and distance become ambiguous, but z and R are still related by the formula

$$1 + z = \frac{R(t_0)}{R(t_e)}\,, \tag{1.5}$$

where t_e is the time at which the radiation is emitted and t_0 is the present (e.g. Weinberg 1972, § 14.3).

In the Friedmann model, the value of R is time-dependent, so the universe is not static. If the universe is expanding, the time derivative of R is positive. If K is also positive, self-gravitation ultimately reverses the expansion, causing the universe to collapse back upon itself. The expansion continues indefinitely if K is zero or negative, since self-gravitation is not strong enough to stop it. (This behavior is not confined to general relativity: A classical self-gravitating system may expand to infinity, collapse, or expand first and then collapse, depending upon its initial direction of motion and its total energy.)

The redshift relation observed by Hubble can thus be interpreted as the result of an overall expansion of the universe. One can project the observed expansion rate backward to a time when all the matter in the universe (and space-time itself) was compressed to a singularity. The expansion of the universe from this initial, highly dense state is the fundamental postulate of the Big Bang model.

To understand the dynamics of the expansion, one must know how the density ρ varies with $R(t)$. As the scale parameter evolves from an initial value R at time t to a later value R' at time t', the volume $V(t)$ enclosed by a comoving sphere changes by a ratio

$$\frac{V(t')}{V(t)} = \left(\frac{R'}{R}\right)^3 .$$

In a homogeneous universe, the total amount of rest-mass enclosed by the sphere remains unchanged, so the rest-mass density ρ_M varies as $V(t)^{-1}$. In a matter-dominated universe, most of the effective mass comes from the rest masses of non-relativistic particles, so

$$\rho \approx \rho_M \sim V(t)^{-1} \sim R(t)^{-3} .$$

The effective mass of relativistic particles, on the other hand, comes mainly from their kinetic energy. If most of the effective mass density is derived from such particles, the universe is termed radiation-dominated. For photons, one can derive the relation between R and the photon energy from equations (1.1) and (1.5) together with Planck's equation $E = h\nu$:

$$\frac{E_{photon}(t)}{E_{photon}(t')} = \frac{\nu(t)}{\nu(t')} = \frac{1+z}{1+z'} = \frac{R(t')}{R(t)} ,$$

or

$$E_{photon}(t) \propto R(t)^{-1} . \tag{1.6}$$

(z and z' are the redshifts of radiation emitted at times t and t' and observed now.) The energy density of the collection of photons is the product of the number density of photons ($\sim R^{-3}$) and the photon energy ($\sim R^{-1}$), so the scaling relation for the effective mass density in a radiation-dominated universe is

$$\rho \approx \rho_R \sim R(t)^{-4} . \tag{1.7}$$

Although equation (1.7) was derived for photons, it is valid for the kinetic (or thermal) energy density of relativistic particles in general.

To derive the relationship between R and the temperature T of the relativistic gas, consider the occupation number η:

$$\eta(E) = \frac{1}{\exp(\frac{E}{kT}) \pm 1} , \tag{1.8}$$

where the sign in the denominator is positive for fermions and negative for bosons, and where E, the total energy of a given particle, is primarily kinetic. (The chemical potential can be neglected since the relativistic particles are able to pair-produce and annihilate freely.) As the universe expands, the scale factor increases from R at time t to R' at time t' and the energy of the particle decreases from E to $E' = ER/R'$. Since the expansion is adiabatic, the occupation number η for particles at time t with energy E is equal to the occupation number η' at time t' and energy E', so

$$\eta'(E') = \eta'(ER/R') = \eta(E) = \frac{1}{\exp(\frac{E}{kT}) \pm 1} = \frac{1}{\exp(\frac{ER/R'}{kTR/R'}) \pm 1} = \frac{1}{\exp(\frac{E'}{kTR/R'}) \pm 1} .$$

The temperature at time t' is therefore TR/R', and in general

$$T(t) \propto R(t)^{-1} . \tag{1.9}$$

According to the Stefan-Boltzmann law, the energy density for blackbody radiation is given by $\rho_R = a/c^2T^4 \sim R^{-4}$, in agreement with equation (1.7). Although equation (1.9) has been derived for a relativistic gas (e.g. photons), it is also valid for non-relativistic particles in thermal contact with the photons as long as the photons possess most of the thermal energy. This condition is satisfied long after the universe has ceased to be radiation dominated.

At redshifts greater than a few hundred, the second term in equation (1.3), Kc^2, is small enough compared to the other two terms that it can be neglected. Under these circumstances, equation (1.3) reduces to

$$\dot{R}^2 = \frac{8\pi G}{3}\rho R^2 ,$$

with solutions $R(t) \sim t^{1/2}$ in a radiation-dominated universe and $R(t) \sim t^{2/3}$ in a matter-dominated one.

1.1.2 The Hot Big Bang

The hot big bang model has its origins in Gamow's studies of nucleosynthesis in the early universe (Gamow 1946; Alpher *et al.* 1948; Gamow 1949). Gamow assumed that matter in the universe started out in the form of neutrons, some of which were ultimately incorporated into nuclei while the rest β-decayed into protons and electrons. If the universe were cold, the newly formed protons would quickly capture neutrons to form heavier nuclei. To reproduce the observed hydrogen abundance, Gamow postulated that the temperature of the universe remained high enough to photo-dissociate deuterium until the density of nucleons had dropped to the point where deuterium formation could readily occur. Those deuterons that did form fused with one another or with nucleons, ultimately yielding He^4 with trace amounts of He^3 and H^3. The majority of neutrons, not being bound, simply decayed to protons.

The modern hot big bang model bears a strong resemblance to the one put forward by Gamow, although our increased understanding of the physics of the early universe has enabled us to fill in many of the missing details and to correct some errors present in the early versions. According to the modern picture, the universe started out at a definite time, some ten to twenty billion years ago. Its earliest stages are poorly understood, but its density and temperature were both very high, and baryons, leptons, and perhaps more exotic particles were pair-produced in large numbers. In the temperature range from $\sim 10^{27}$ to $\sim 10^{12}$ Kelvins (10^{14} GeV to 10^{-1} GeV), the physics is still somewhat uncertain because of our incomplete understanding of the behavior of the strong force at high energies and also because of the large number of particle types that can exist in equilibrium at such high temperatures. The development of "Inflationary" models within the past few years has provided interesting and potentially important insights into the early part of this period, although the properties of these models are somewhat speculative (Brandenberger 1985). As expansion progressed, the temperature of the universe dropped. When it dropped below the pair-production threshold for a given particle type, new particles were no longer produced to replace those that decayed or annihilated, and that particle type quickly disappeared. When the temperature crossed the thresholds for muons and pions at $\sim 10^{12}$ K, these particles disappeared. The disappearance of the muons meant that muon neutrinos, although still present, were effectively decoupled from the rest of the matter in the universe. The only particles generally believed to have remained were electrons and positrons, neutrinos, photons, gravitons (which had long since ceased to interact with other particles or each other), and the small number of protons and neutrons that remained after the vast majority of these particles had annihilated.

Members of the residual population of protons and neutrons could convert freely from one particle type to the other by means of reactions such as

$$p + e^- \leftrightarrow n + \nu$$

and

$$p + \overline{\nu} \leftrightarrow n + e^+ \ .$$

The rates of these reactions were rapid compared to the expansion rate of the universe, so the ratio of neutron to proton densities during this period was just the equilibrium value

$$n_n/n_p = e^{-Q/kT} \ ,$$

where Q, the energy difference between the neutron and the proton, is 1.29 MeV, equivalent to a temperature of 1.5×10^{10} K. Note that at $T >> 10^{10}$ K, n_n/n_p approaches one rather than infinity, as Gamow had assumed.

The universe continued to expand, with $R(t)$ increasing as $t^{1/2}$. When the temperature fell to about 10^{10} K, the electron neutrinos could no longer maintain thermal contact with their surroundings, and so they, like the muon neutrinos and gravitons, became decoupled. At about 3×10^{10} K, the ratio of neutrons to protons departed from equilibrium due to the decreasing efficiency of the conversion reactions. By the time the temperature dropped to 1.3×10^{10} K, two-body reactions had virtually ceased and only neutron decay ($n \rightarrow p + \overline{\nu} + e^-$) was still active. The temperature continued to decrease until it reached $\sim 5 \times 10^9$ K ($z \sim 2 \times 10^9$), at which point $e^\pm$ production ceased and nearly all the electrons annihilated.

In order for He^4 or other complex nuclei to have formed from the free baryons, the neutrons first had to fuse with protons to form deuterium. At temperatures above approximately 1×10^9 K ($z \sim 4 \times 10^8$), any deuterons that happened to form were quickly photo-dissociated, so helium production was inhibited. Once the temperature dropped below that point, the deuterium concentration rapidly rose to a level where helium formation could commence, and almost all of the neutrons that had survived to that time were bound up into α-particles.

The expansion continued, and the temperature continued to decrease. At a temperature somewhere between $\sim 10^3$ K and $\sim 10^4$ K, the photon energy density fell below the matter density and the universe became matter-dominated, with $R(t)$ scaling as $t^{2/3}$. Another important transition occurred at a temperature of approximately 4000 K ($z \simeq 1500$), roughly 7×10^5 years after the big bang, when the free electrons combined with the protons and α-particles to form neutral atoms. Because Compton scattering could no longer promote energy and momentum transfer between matter and radiation, this event effectively decoupled the photons from the matter.

Since decoupling, the radiation has been more or less free to propagate through the universe without any major changes except for the cooling caused by the expansion of the universe. The matter, in the mean time, has undergone processes that have profoundly altered its distribution and composition from what they were at the time of decoupling. It is because the radiation preserves information from the time prior to decoupling that it provides such a useful tool for the study of the early universe.

1.1.3 The Cosmic Background Radiation

1.1.3.1 Prediction and Discovery

The cosmic background radiation, a thermal remnant left over from the formation of the universe, follows naturally from the Hot Big Bang model. Alpher and Herman were among the first to predict the existence of the CBR. Extending the work done by Gamow on the hot big bang model, they pointed out that the observed helium abundance could be explained if the helium had been produced in the presence of a cosmological radiation field with a current thermodynamic temperature of roughly 5 K (Alpher and Herman 1950).

Why their prediction did not spur experimentalists to try to detect the radiation is a subject for speculation. Addressing this question, Weinberg (1977) expresses the opinion that it was overlooked and ignored partly as a result of poor communications between theoreticians and experimentalists, but primarily because of scientific prejudices against cosmogenic theories of nucleosynthesis and against cosmogenic theories in general. In any event, the prediction was lost in the literature. Astronomers remained generally unaware of the notion that a hot big bang could give rise to observable radiation until the mid-1960's, when a number of theoreticians reinvestigated the properties of nucleosynthesis in the hot big bang (e.g. Hoyle and Tayler 1964; Peebles 1966).

Among the theoreticians was P. J. E. Peebles at Princeton, who began studying the subject at the suggestion of R. K. Dicke. Dicke was interested in both the theoretical and observational aspects of the hypothetical remnant radiation, and besides encouraging Peebles in his calculations, he also set D. Wilkinson and P. G. Roll to building a low-noise radiometer to try to detect the radiation if it should be present.

Before Roll and Wilkinson could complete their measurements, A. Penzias and R. W. Wilson of Bell Laboratories made their now-famous observations of the sky brightness temperature at 7.35 cm using the 20-foot horn-reflector antenna at Holmdel, New Jersey. These measurements were not motivated by cosmological considerations, but were intended principally to determine the noise characteristics of the antenna and receiver as a prelude to a planned program of galactic measurements. Penzias and Wilson observed an unexplained, isotropic source of noise at a temperature of 3.5 ± 1.0 K, apparently external to the antenna and receiver, which puzzled them until they learned of Peebles' work and the possibility of a cosmic background radiation. Companion papers on the subject were published by Penzias and Wilson (1965) and by Dicke, Peebles, Roll, and Wilkinson (1965), the first describing the observed temperature excess and the second suggesting the CBR as a possible source of the excess.

1.1.3.2 Observed Characteristics

As one of the only relics of the very early universe still available for study, the CBR has had its various properties measured in detail, sometimes to excruciating levels of precision. Among the properties of the CBR that have been studied are its polarization, its anisotropy on various angular scales, and its spectrum. Weiss (1980) provides a fairly current review of the state of these observations. Both the polarization and the anisotropy were first studied by Penzias and Wilson, who reported in their original paper that the radiation was "isotropic, unpolarized, and free from seasonal variations" within the limits of their observations.

Their crude upper limits on the polarization and anisotropy have been greatly improved on during the past twenty years. The current upper limit on the linearly polarized component of the radiation is 0.2 mK at a 95% confidence level at 9 mm wavelength (Lubin, Melese, and Smoot 1983).

A dipole anisotropy of approximately 3 mK was first observed in 1976–1977 by M. Gorenstein, R. Muller, and G. Smoot of the University of California, Berkeley (Smoot *et al.* 1977) and by Wilkinson and his coworkers at Princeton (Corey and Wilkinson 1976; Corey 1978). Both groups made their measurements from the air to avoid signal contamination by the atmosphere, the Berkeley measurements from a U2 aircraft and Princeton measurements from a balloon gondola. More recent measurements by these groups have established a dipole anisotropy of 3.6 ± 0.2 mK at 3.3 mm (Lubin, Epstein, and Smoot 1983) and 3.1 ± 0.2 mK at 1.2 cm (Fixen *et al.* 1983), and set a 90% C. L. upper bound of approximately 0.2 mK on any quadrupole anisotropy present in the radiation. The observed dipole anisotropy may simply be the result of the Doppler shift caused by the earth's motion with respect to the average rest frame of the surface of last scattering. The required velocity, approximately 350 km/sec, is on the same scale as both the sun's orbital velocity around the galaxy and the peculiar motion of the galaxy itself relative to the Hubble flow (Davis and Peebles 1983). The lack of an observable quadrupole anisotropy adds weight to the contention that the dipole anisotropy is primarily a Doppler effect rather than being due to variations in the distribution of the radiation itself.

Researchers have also searched for anisotropies on smaller scales, so far without success. Upper limits on observed intrinsic anisotropies range from approximately 10^{-3} to 5×10^{-5} on angular scales from 3 arc-minutes to 30° (Smoot 1980; Partridge 1980; Uson and Wilkinson 1984).

The spectrum of the CBR has been subjected to scrutiny almost from the beginning. A prime motivation for the early CBR temperature measurements was to see if the spectrum approximated that of a blackbody, as would be the case if the radiation were the remnant of a hot big bang. In particular, measurements were made at shorter and shorter wavelengths in an effort to determine whether or not the spectrum had the downturn in the Wien region that characterizes a blackbody.

Radiometric measurements from the ground and the air, as well as observations of interstellar CN molecules, have all yielded brightness temperatures of about 2.5 to 3.5 K, thus establishing the general blackbody nature of the spectrum. However, the CBR measurements made prior to this project do not rule out spectral distortions of up to 20% in the Rayleigh-Jeans region, and they provide positive evidence for distortions at the 10% level in the Wien region. This research project and other recent CBR measurements have set tighter bounds on the possible distortions in both the Rayleigh-Jeans and Wien regions. These recent results, and their interpretation, are the subject of this work.

1.2 The Spectrum of the CBR

1.2.1 The Physics of Spectral Distortions

The possible presence of distortions in the CBR spectrum is scientifically interesting because the distortions record the thermal history of the universe from $z \sim 10^6$ to the present. The spectrum of the background radiation observed today is the result of interactions between the radiation and matter throughout the history of the universe. The nature of these interactions altered as the temperature and the matter density have changed, but their primary effect has been to maintain thermal contact between the matter and the radiation, either by the creation and absorption of photons or by means of energy transfer between matter (primarily free electrons) and existing photons.

These processes, if allowed to run to completion, would cause the CBR to have a blackbody spectrum at the equilibrium temperature of both the matter and radiation. However, if energy initially associated with the matter is transferred to the radiation at a relatively late epoch, there may not be time enough to re-establish a Planck spectrum. The energy transferred to the radiation may either be thermal, as is the case if the matter is heated by the decay of unstable particles, or kinetic, if the material has a large bulk velocity. If the matter and radiation are out of equilibrium, simple (non-radiative) Compton scattering shifts the photons in the radiation field to shorter wavelengths, but bremsstrahlung, the primary mechanism for creating new photons, may not be efficient enough to increase the photon population to its equilibrium value in the time available. The resulting spectrum is roughly Planckian but with distortions whose characteristics depend upon the amount of energy transferred to the radiation, the redshift at which the transfer occurred, and to some extent the mechanism of energy transfer.

1.2.1.1 The Initial Spectrum

At redshifts greater than a few times 10^9, the conversion of photons to electron-positron pairs and back again maintains a tight coupling between the matter and the radiation field. The high density of leptons also promotes bremsstrahlung ($2e^{\pm} \rightarrow 2e^{\pm} + \gamma$), whose efficiency is proportional to $n_e{}^2$, and Compton scattering (both simple, $\gamma + e^{\pm} \rightarrow \gamma + e^{\pm}$, and radiative, $\gamma + e^{\pm} \rightarrow 2\gamma + e^{\pm}$), proportional to n_e, where n_e is the lepton density. Photon production can take place on timescales short compared to the expansion time, and any non-blackbody spectral features are quickly erased.

As the universe expands, the temperature drops below the point where e^+e^- pair production can be sustained and the vast majority of the electrons and positrons annihilate. Despite the disappearence of most of the electrons, their density is still high enough so that photon-producing processes remain active. Bremsstrahlung is able to maintain a blackbody spectrum until a redshift of $\sim 10^8$ (Illarionov and Sunyaev 1975). Even after bremsstrahlung loses its effectiveness, radiative Compton scattering continues to maintain the spectrum until a redshift z_T, which ranges from 1 to 7 times 10^6 depending on the value of the density parameter Ω (Danese and De Zotti 1982; Lightman 1981). Early treatments of the formation of possible distortions neglected radiative Compton scattering in the redshift range $z \sim 10^6 - 10^8$ with the result that the survival of distortions formed during this period was overestimated.

1.2.1.2 The Spectrum from z_T to Recombination

When the redshift drops below about z_T, the steep energy dependence of radiative Compton scattering causes it to turns off sharply, and only the relatively inefficient bremsstrahlung process is available to produce new photons. If the matter and the radiation go out of equilibrium, non-radiative Compton scattering quickly restores the energy balance and causes the radiation spectrum to assume a Bose-Einstein distribution with a chemical potential μ determined by the fractional energy transferred from matter to radiation. Bremsstrahlung is still active but it can only generate photons efficiently at long wavelengths, so a blackbody spectrum is reestablished only at wavelengths longer than some minimum value. At shorter wavelengths, the spectrum maintains a Bose-Einstein form, although bremsstrahlung-produced photons, Compton scattered upward in energy from longer wavelengths, gradually fill in the spectrum, causing μ to diminish with time.

At redshifts smaller than $z_a \sim 10^5$, the electron density is no longer high enough for Compton scattering to establish a true Bose-Einstein spectrum. The spectrum assumes a mathematically more complex form, but its main characteristics are an increased brightness temperature in the far Rayleigh-Jeans region due to bremsstrahlung emission by relatively hot electrons, a reduced temperature in the middle Rayleigh-Jeans region where the photons are depleted by Compton scattering, and a high temperature in the Wien region, where the Compton-scattered photons from long wavelengths have accumulated. The distortion shows up as an increase in temperature with decreasing wavelength in the Wien region and a sharp temperature rise in the Rayleigh-Jeans spectrum going from the Compton-depleted region to the bremsstrahlung-augmented region. The wavelength at which the rise occurs is determined by the electron density at the time of energy injection, and the amount of the rise depends upon the electron temperature, so this type of distortion conveys a good deal of information about the time and mechanism of energy injection.

1.2.1.3 The Present Spectrum

Neither Compton scattering nor bremsstrahlung can take place in an unionized medium, so in simple cosmological models, the spectrum at recombination is more or less preserved until the present, though redshifted by a factor of a thousand or so. More complex cosmological models may call for substantial energy injection resulting from the formation of galaxies, quasars, or first-generation stars, which could produce observable distortions.

Galaxy or quasar formation may reionize the intergalactic or intercluster medium, creating conditions somewhat like those at redshifts between 10^3 and 10^5 but with a lower electron density and a higher ratio of electron temperature to radiation temperature. The effect of these conditions on the CBR spectrum would again be to raise the brightness temperature in the Wien region and at very long wavelengths.

Other models postulate the presence of dust at redshifts of ~10 to 100, created in and heated by massive Population III stars. Infrared radiation from the warm dust would add to the CBR, causing spectral distortions in the 0.1 to 1 mm range whose features would depend on the temperature and chemical composition of the dust and the redshift at which dust formation occurred (Negroponte *et al.* 1981).

1.2.2 Previous Measurements of the CBR Spectrum

1.2.2.1 Heterodyne Measurements

In the five years following Penzias and Wilson's original discovery, numerous researchers, starting with Roll and Wilkinson (1966) measured the CBR temperature from the ground using microwave receivers at wavelengths ranging from 73 cm to 3.3 mm. These measurements are well summarized in the review article by Weiss (1980). The precision of the measurements varied considerably from one to another, due to the difficulties inherent in measuring the CBR temperature and to the varying techniques used by different investigators. Uncertainty in the contribution of galactic radio emission to the measured signal limited the accuracy of measurements at long wavelengths, while at short wavelengths the accuracy was limited by the increasing noise-power contribution from the atmosphere and the radiometer components themselves, coupled with a decreasing contribution from the CBR.

After an initial round of rough measurements to verify the presence of the CBR, more precise measurements were made at shorter and shorter wavelengths in an effort to determine whether or not the spectrum had the downturn in the Wien region that characterizes a blackbody. The weighted average of these ground-based measurements was 2.74 ± 0.09 K, but the uncertainties in the individual measurements were large enough so that distortions of as much as 20% from a blackbody spectrum could not be ruled out in the Rayleigh-Jeans region. Ground-based heterodyne measurements at 3.3 mm provided a firm indication of a downturn in the antenna temperature at short wavelengths (Stokes *et al.* 1967; Millea *et al.* 1971).

1.2.2.2 CN Measurements

This trend was reinforced by spectroscopic observations of interstellar CN molecules. McKellar (1941) studied the absorption spectrum of CN molecules in the direction of ζ Ophiuchi and noted that the widths of CN absorption lines near 3875 Å indicated that the molecules were subjected to excitation temperatures of approximately 2.3 K. The significance of this result was realized soon after the discovery of the CBR. Measurements by Field and Hitchcock (1966) and by Thaddeus and Clauser (1966) yielded excitation temperatures of 2.7 K to 4.2 K at 2.64 mm wavelength. Later observations yielded more precise values: Thaddeus (1972), computing the weighted mean of the CBR temperatures obtained from the CN measurements then available, obtained the value $T_{CBR} = 2.78 \pm 0.10$ K at 2.64 mm. Recent measurements of the CN spectrum have yielded more precise values (Meyer and Jura 1984; Meyer and Jura 1985). These are discussed in Chapter 9.

1.2.2.3 Balloon- and Rocket-Borne Bolometric Measurements

Radiometric measurements of the CBR spectrum at wavelengths shorter than 3 mm could not be made from the ground because of atmospheric signal contamination, so the instruments were mounted either on rockets or on balloon gondolas. The detectors used for the first few of these measurements were broadband, liquid-helium cooled bolometers with one or more bandpass filters to define the instrument response. The results of these first measurements were ambiguous and often contradictory—some of them indicated a large radiation flux compatible with a 5–10 K blackbody (e.g. Shivanandan, Houck, and Harwit 1968; Houck and Harwit 1969; Muehlner and Weiss 1970) while others did not (e.g. Blair *et al.* 1971; Muehlner and Weiss 1973a; Muehlner and Weiss 1973b).

By the early 1970's it had become clear that there was not a large flux excess at short wavelengths, but detailed studies of the spectral shape had to wait for the next generation of instruments, especially one built by P. Richards and his coworkers J. Mather and D. Woody. This device used cryogenic bolometer in conjunction with a Fourier spectrometer to map out the spectrum from 4 to 0.4 mm. The second flight of this instrument, in 1978, provided detailed spectral information at wavelengths from 4 mm to 0.7 mm, where atmospheric contamination began to degrade the data substantially (Woody and Richards 1979, 1981).

Although their measurements yielded a spectrum that resembled a blackbody, it differed from a blackbody spectrum at a statistically significant level. The integrated flux was equal to that of a 2.96 K blackbody, but the spectral shape departed from the blackbody curve for that temperature, being somewhat higher than the blackbody curve at wavelengths longer than 1.1 mm and lower than the blackbody curve at shorter wavelengths. Although the data were poorly fit by a blackbody curve, they could be well fit by a "super-blackbody" having a temperature of 2.79 K and an emissivity of 1.27.

Many researchers viewed the details of the spectral shape with skepticism, since a 27% error in the gain calibration could have produced the observed distortion (Weiss 1980). In addition, the brightness temperature observed by Woody and Richards in the region near 3 mm differed from the weighted average of the best radiometric measurements in that region (Millea *et al.* 1971) and the best available CN measurements (Thaddeus 1972) by 1.6σ. Attempts to explain the spectral distortion as the natural result of known physical processes were not convincing; in order to reproduce the observed spectrum, theoreticians either had to postulate departures from currently accepted physical laws (e.g. Georgi *et al.* 1983) or they had to invoke models with several free parameters that could be adjusted to match the spectrum (e.g. the dust model of Negroponte *et al.* 1981).

More recent bolometric measurements of the same part of the spectrum by Peterson *et al.* (1985), do not reproduce the distortions reported by Woody and Richards. The interpretation of these recent results is discussed in Chapter 9.

1.3 The Spectrum Project

1.3.1 Reasons to Remeasure T_{CBR}

By the end of the 1970's it was apparent that existing CBR measurements longward of 3 mm did not rule out potentially observable, cosmologically significant distortions in the Rayleigh-Jeans portion of the spectrum. Such distortions, if observed, might prove important in our understanding of galaxy formation and the small-angular-scale anisotropy of the CBR. When Danese and De Zotti (1978) fitted the existing measurements to model distortions, they found that distortions of up to a Kelvin could exist in the Rayleigh-Jeans region without contradicting the available observations.

Interest in possible Rayleigh-Jeans distortions was further piqued by the puzzling short-wavelength distortions seen by Woody and Richards. It was hoped that the mechanisms responsible for these distortions would alter the spectrum at longer wavelengths as well, and that the Rayleigh-Jeans spectrum might provide some clue as to the nature of the processes responsible.

1.3.2 The Spectrum Collaboration

Prompted by these considerations, we at Berkeley started in 1978 to consider a remeasurement of the CBR Rayleigh-Jeans spectrum. At about the same time, a similar set of measurements was being planned by group of researchers from the U. S. and Italy, consisting of G. Sironi of the Istituto Fisica Cosmica, Consiglio Nazionale delle Ricerche (CNR) at Milano, Italy, N. Mandolesi of the Istituto Tecnologia e Studio della Radiazione Extraterrestre, CNR, at Bologna, Italy, L. Danese and G. De Zotti of the Universitá di Padova, and R. B. Partridge of Haverford College, Haverford, Pennsylvania.

In 1979, the two research efforts were merged, and the tasks and responsibilities were apportioned among the participants. The initial agreement called for three radiometers, at wavelengths of 12 cm, 6.3 cm, and 3 cm, to measure T_{CBR}, and a fourth radiometer at 3.2 cm to monitor atmospheric emission. To minimise spurious temperature variations due to systematic errors, the antennas selected for the three CBR-measuring radiometers were matched, wavelength-scaled corrugated horns with 12.5° half-power beamwidths, and all three radiometers used the same liquid-helium-cooled reference load for absolute calibrations (see § 2.4 and § 3.3). The collaborators decided that Milano would supply the 12-cm radiometer (Sironi *et al.* 1984), Bologna the 6.3-cm instrument, (Mandolesi *et al.* 1984), Berkeley the 3-cm radiometer (Friedman *et al.* 1984; Friedman 1984) and the cryogenic reference load (Smoot *et al.* 1983), and Haverford the atmospheric monitor (Partridge *et al.* 1984), while Padova would provide theoretical support both in the interpretation of results and in the modeling of atmospheric emission.

Initially, Berkeley hoped to build an additional pair of radiometers that could be tuned over a range of wavelengths, one to cover the range from 15 to 70 cm and the other to operate from 2 to 15 cm. It proved impractical to build and test such radiometers in the time available, so we reluctantly postponed that aspect of the project. However, we did build an additional pair of fixed-wavelength radiometers, operating at wavelengths of 9.1 and 3.3 mm, to extend the spectral coverage of our measurements and to span the gap separating our Rayleigh-Jeans measurements at 3 cm and beyond from the bolometric measurements at short wavelengths. De Amici *et al.* (1985) provide a description of the 9.1-mm instrument; the 3.3-mm instrument is described in this work.

Chapter 2

Experimental Concepts and Requirements

2.1 Measurement Concepts

To measure T_{CBR}, one measures the spectral power, or power per unit bandwidth, intercepted by an antenna pointed toward the zenith, then subtracts from it the components contributed by the surroundings, the atmosphere, the galaxy, and other known noncosmological sources. These noncosmological backgrounds, which are reduced to a minimum through careful equipment design, choice of observing times, choice of wavelength, and site selection, are either measured or estimated.

These measurements are performed with a radiometer, a device that measures the spectral power entering its input port. An antenna placed at the input port collects incoming radiation and channels it into the radiometer. Nyquist (1928) showed that the noise power per unit bandwidth available from a resistive load at temperature T is

$$w = \frac{kT_\nu}{\exp(T_\nu/T) - 1} . \tag{2.1}$$

T_ν, defined as

$$T_\nu = h\nu/k , \tag{2.2}$$

characterizes the transition between the Rayleigh-Jeans regime at temperatures $T >> T_\nu$ ($kT >> h\nu$) and the Wien regime at temperatures $T << T_\nu$ ($kT << h\nu$). At 3.3-mm wavelength, its value is 4.32 K. It can be shown from thermodynamic considerations that equation (2.1) also applies to the spectral power collected by a lossless antenna in an isotropic blackbody radiation field with characteristic temperature T (Kraus 1966, § 3.18). Antenna temperature T_A is defined as

$$T_A \equiv w/k,$$

so equation (2.1) can be rewritten as

$$T_A = \frac{T_\nu}{\exp(T_\nu/T) - 1} . \tag{2.3}$$

In the Rayleigh-Jeans limit, where $T >> T_\nu$, equation (2.3) reduces to

$$T_A \simeq T - \frac{1}{2}T_\nu .$$

Thus the antenna temperature of a sufficiently warm blackbody is approximately equal to the blackbody temperature minus a small constant.

When a radiometer views an object through its input port, it responds by producing an output voltage proportional to the object's antenna temperature, along with a target-independent offset voltage. The principle of a radiometric measurement is to determine the difference in the output voltage when the radiometer views the object of interest and when it views a blackbody at a known temperature. To convert the voltage difference to a temperature difference, the proportionality factor, or calibration coefficient, must be measured. One can perform the calibration by allowing the radiometer to view two blackbody targets at two known temperatures. The ratio of the (known) antenna-temperature difference between the two targets to the measured voltage difference of the radiometer response is the radiometer calibration coefficient G. If both targets satisfy the Rayleigh-Jeans criterion, the difference in their antenna temperatures is equal to their physical temperature difference, so G is then simply the ratio of the targets' temperature difference to the output voltage difference.

The output voltage of an ideal superheterodyne radiometer undergoes random fluctuations proportional to the sum of the radiometer noise temperature and the temperature of the target which set a limit on the accuracy that can be achieved by a measurement of a given duration. These fluctuations have a "white," or frequency-independent, spectrum. If the output voltage is averaged for a time τ, the rms variation between successive averages is given by the equation:

$$\delta T_{rms} = K\frac{T_{sys} + T_{target}}{\sqrt{B\tau}}\,, \tag{2.4}$$

where T_{sys} is the radiometer noise temperature, T_{target} is the antenna temperature of the target, B is the receiver IF bandwidth, and K is a term equal to 1 for a total-power radiometer and approximately 2 for a Dicke radiometer (Kraus 1966, § 7.1i). It is seen from the equation that time-averaging can improve the accuracy of the measurement.

2.2 Experimental Goals

Models of the origin and evolution of the CBR predict spectral features of up to several tenths of a Kelvin; measurements of T_{CBR} can provide useful constraints only if they are sensitive to spectral distortions at that level. Such sensitivity requires the data to have two characteristics: good spectral coverage and measurement accuracy.

To provide adequate spectral coverage, we initially chose to make measurements at five wavelengths over the range from 12 to 0.33 cm. The longest of these wavelengths was dictated by the fact that radio emission from the galaxy, a serious source of signal contamination, rises steeply with increasing wavelength. The shortest wavelength was set by the structure of the atmospheric emission spectrum, which increases dramatically at wavelengths shorter than about 1 cm but has a window centered near 3.3 mm.

In a practical sense, measurement accuracy is set by systematic uncertainty, the accuracy with which one knows the terms entering into the data analysis. The most important of these terms are the radiometric temperature of the cold load, the radiometric temperature of the atmosphere, and, at long wavelengths, the radio emission from the galaxy. Our goals with respect to measurement accuracy were twofold: first, to reduce the systematic uncertainties at each wavelength as much as possible by appropriate radiometer and cold load design, observing technique, and choice of observing site; second, to use the same cold load for measurements at each wavelength and to make all measurements at the same site under similar conditions, in order to avoid variations in the systematic errors which could introduce spurious spectral features. Our design goal at 3.3 mm was to measure T_{CBR} to an accuracy of 0.1 to 0.2 Kelvins.

2.3 Fundamentals of Radiometer Design

2.3.1 Bolometer vs. Superheterodyne Receiver

Two different radiometer technologies are available at 3.3 mm—bolometers and superheterodyne receivers. A bolometer is essentially a very small microwave absorber with a differential thermometer attached. Absorbed microwave power heats the bolometer, causing a temperature rise which the thermometer measures. The thermometer produces an output voltage proportional to the temperature rise and thus proportional to the the power flux intercepted by the bolometer. The bandwidth of a bolometric radiometer is determined by bandpass filters placed in front of the bolometer. A superheterodyne receiver, on the other hand, uses a mixer to shift the input signal to a low frequency before it is filtered and rectified.

Both approaches have their advantages, but superheterodyne receivers are better adapted to ground-based measurements of T_{CBR} for several reasons. First, superheterodyne receivers are better-suited than bolometers to narrow-bandwidth measurements. This advantage is important because the spectral response of the radiometer must be sharply defined in order take full advantage of the atmospheric window near 3.3 mm. Second, a superheterodyne receiver is more sensitive than an ambient-temperature, narrow-bandwidth bolometer at 3.3 mm. The sensitivity of a bolometer could be improved if the bolometer were cooled to a very low temperature, but to do so would make operation of the radiometer much more difficult.

2.3.2 Basic Anatomy of a Superheterodyne Dicke Radiometer

The type of superheterodyne radiometer most suitable for ground-based measurements of T_{CBR} is the superheterodyne Dicke radiometer, with two switched input ports. A superheterodyne Dicke radiometer makes a differential measurement of the spectral power entering its two input ports. The ports are typically a pair of antennas, or an antenna and a reference termination. Noise power entering the radiometer encounters the Dicke switch, a chopping microwave switch which alternately passes and blocks the radiation from the two input ports.

Radiation that is passed by the switch enters the RF (radio-frequency) port of a mixer, where it is mixed with the signal from a local oscillator to generate the beat frequency. In a double-sideband mixer, the beat or intermediate frequency, ν_{IF}, is given by the equation

$$\nu_{IF} = |\nu_{RF} - \nu_{LO}|,$$

where ν_{RF} is the frequency of the incoming radiation and ν_{LO} is the local-oscillator frequency. RF frequencies equidistant above and below ν_{LO} are down-shifted to the same IF frequency. Radiation entering the mixer spans a range of frequencies, so ν_{IF} can range from nearly DC for incoming radiation near the local-oscillator frequency to a maximum frequency determined by the filtering and matching characteristics of the mixer and the downstream components.

The down-shifted output from the mixer is filtered and amplified, then rectified by a detector diode which produces a DC output voltage proportional to the incoming RF power. The output voltage from the detector is square-wave modulated at the switching frequency of the Dicke switch with an amplitude proportional to the difference in the power entering the two switch ports. This modulated voltage is fed into a synchronous detector (lockin amplifier), a device sensitive to voltage variations whose frequency and phase match those of the switching signal. The lockin amplifies, rectifies, and time-averages the voltage variations that are in phase with the switch and rejects those that are not. The output voltage produced by the synchronous detector is thus proportional to the amplitude of the square-wave modulation, and hence to the power difference at the radiometer input ports.

This design, with its microwave switch and synchronous detector, is somewhat more roundabout than a simple total-power radiometer, which lacks these components and has only one input port. The Dicke design has the advantage however that it reduces the sensitivity of the radiometer to gain variations. A total-power radiometer, with only one input port feeding into the mixer, produces an output voltage proportional to the sum of the power entering the port and the noise power generated within the radiometer, equivalent to a temperature of several hundred to several thousand Kelvins. A gain variation of 0.1% in a total-power radiometer with a system noise temperature of 1000 K causes the output voltage to vary by the same amount as a 1 K change in the temperature of the load viewed by the input port.

Gain variations also affect the output from Dicke radiometers, but only by an amount proportional to the difference in the temperatures viewed in the two states of the Dicke switch. This temperature difference, ΔT, is the difference in antenna temperature of the loads at the two radiometer ports plus an offset temperature that results from differences in the reflection and insertion loss in the two arms of the radiometer. If ΔT is small, a Dicke radiometer is much less sensitive than a total-power radiometer to gain uncertainties. For instance, if $\Delta T = 5$ K, a 0.1% gain error in causes an error of only 5 mK in the measured value of ΔT.

If Dicke radiometers had no inherent offset, a temperature-difference measurement could be made simply by pointing the antennas at the two objects under examination, recording the output voltage from the radiometer, and multiplying by the calibration coefficient to obtain the temperature difference. Unfortunately, the offset makes this simple approach impractical for accurate measurements.

Two approaches can be used to remove the effect of the offset. The first approach is to arrange the radiometer so that one of its ports views a stable reference load while the other one is pointed alternately at the two targets of interest. The output voltages are measured and differenced, and the result is converted to a temperature difference. The reference load can be either a temperature-controlled termination or the sky. Although this approach was used in previous measurements of T_{CBR} and in the measurements made at 3.0, 6.3, and 12 cm for this project, it has one major drawback—the radiometer spends half of its time viewing the reference load instead of the targets of interest. In this way the observation time needed to reduce the radiometer noise to a given level is doubled.

A second approach, used for the 3.3-mm measurements, uses both input ports for observations. Two targets at temperatures T_A and T_B are observed by the antennas at the input ports. The output voltage, proportional to $(T_A - T_B) + T_{Offset}$, is measured. The radiometer is then reoriented so that the targets viewed by the two antennas are reversed. The new output voltage, proportional to $(T_B - T_A) + T_{Offset}$, is subtracted from the previous output voltage to give a value proportional to $T_A - T_B$, with T_{Offset} removed.

This offset-subtraction technique assumes that the offset is the same in both positions. In order for this assumption to be valid, the radiometer must not change its offset when its orientation is changed. If the components are not firmly and securely attached to a very stiff mounting structure, they can move relative to one another when the radiometer is rotated about a horizontal axis. This motion puts stresses on the waveguide and other components which lead to orientation-dependent changes in the instrument offset (known as flip offset in the local argot). Offset changes can also be induced by the Earth's magnetic field acting on magnetically sensitive components in the radiometer. Problems of this sort have plagued previous investigators to such an extent that some of them designed radiometers which did not need to be moved during the observations (Wilkinson 1967). Such designs call for tradeoffs which can compromise the performance of the instrument in other ways, however. After evaluating a number of designs, we concluded that the radiometer could be designed in such a way that changes in its orientation would not causing an unacceptably large flip offset.

2.4 Principles of CBR Measurement

The first step in a measurement of T_{CBR} is to determine the antenna temperature of the zenith, T_{Zenith}. One determines T_{Zenith} by measuring the output voltage produced by the radiometer when it views the zenith and the cold load. The voltage is multiplied by the calibration coefficient G and the resulting temperature difference is added to the antenna temperature of the absolute load as shown in equation (2.5):

$$T_{Zenith} = \frac{G}{2}(V_{Zenith/Load} - V_{Load/Zenith}) + T_{A,Load} \, . \tag{2.5}$$

($T_{A,Load}$ is the antenna temperature of the absolute load and $V_{Zenith/Load}$ and $V_{Load/Zenith}$ are the output voltages from the radiometer in the two positions.) The closer the temperature of the absolute load is to $T_{A,CBR}$, the less the ultimate result is affected by calibration error. The absolute load is therefore cooled with liquid helium (LHe) to a temperature near absolute zero.

Equation (2.5) does not include the small instrumental corrections for reflector emission, instrumental offset variations, and other effects that are inevitable in a measurement of the CBR temperature. These terms are discussed in detail in Chapters 7 and 8.

When an antenna points toward the zenith, radiation enters it from a variety of sources, local and distant. The ground, the atmosphere, the sun and moon, the galaxy, and the cosmos may all contribute to the observed signal. A measurement of T_{CBR} must discriminate among these various sources in order to exclude all the noncosmological components of the radiation.

To a radiometer, the ground resembles a blackbody emitter at a temperature of 270 to 300 Kelvins and subtends a solid angle of 2π steradians. The antennas must therefore exhibit low side- and back-lobe response in order to block out ground radiation. Metal shields also help to reduce the ground radiation seen by the radiometer to an acceptable level. These act as mirrors which reflect radiation from the cold sky toward the antennas while blocking the much more intense radiation from the ground.

If the antennas are properly shielded from ground emission, the largest component of T_{Zenith} at 3.3 mm is produced by the atmosphere. Atmospheric emission at 3.3 mm is produced almost entirely by water and oxygen molecules. The spectrum is pressure broadened, so the emission strength is substantial even well away from the line centers. Figure 2.4 plots the estimated atmospheric antenna temperature seen by a radiometer looking toward the zenith from an altitude of 3800 meters. The wavelength 3.3 mm lies in an atmospheric window, between a complex of oxygen lines near 5 mm and an oxygen line at 2.5 mm. Nevertheless, atmospheric emission is substantial and variable: Measurements made in Berkeley on clear nights have yielded values of $T_{A,atm}$, the antenna temperature of the zenith, in the range from 25 to 45 Kelvins, depending upon the atmospheric water-vapor content. Time variations in $T_{A,atm}$ are as serious a problem as emission itself, since the clumpy nature of the water-vapor distribution can cause the measured temperature to change by several tenths of a Kelvin in a matter of minutes.

Atmospheric emission cannot be eliminated from a ground-based measurement, but it can be reduced. $T_{A,atm}$ is substantially reduced if observations are made from a high-altitude, low-humidity site, not only because the column densities of oxygen and water vapor are lower, but also because of the lower atmospheric pressure reduces the emission from the wings of the pressure-broadened lines. Both of these trends lead to reduced atmospheric opacity. The low level of atmospheric water vapor also reduces the variation in $T_{A,atm}$.

Even so, $T_{A,atm}$ is still large compared to T_{CBR}. To remove $T_{A,atm}$ from T_{Zenith} requires independent knowledge of $T_{A,atm}$, obtained from radiometric observations of the sky at multiple zenith angles. These measurements determine the change in the atmosphere's antenna temperature as a function of its column density. They are fitted to a model of the variation in the

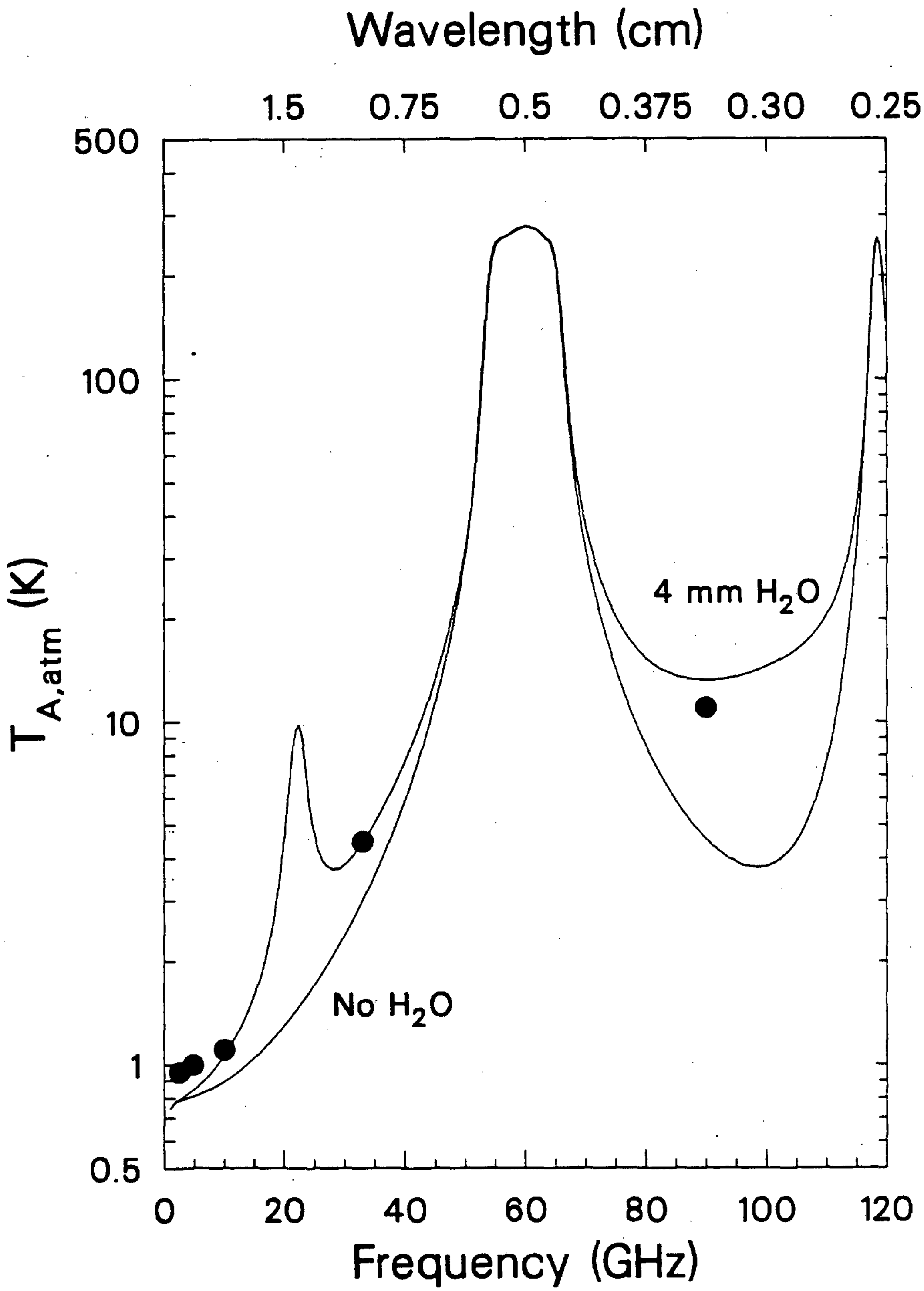

Figure 2.1: Measured and calculated atmospheric emission at 3800 m. Plotted points are our typical measurement values.

atmospheric emission with zenith angle Z to yield $T_{A,atm}$. Appendix A describes the atmospheric model. The fitting procedure is discussed in Chapter 7.

Variations in atmospheric conditions can cause errors in the measured values of $T_{A,atm}$, but careful planning can minimize these errors. $T_{A,atm}$ may change substantially within a matter of minutes, so the time interval between measurements of T_{Zenith} and $T_{A,atm}$ should be kept as short as possible. The clumpy nature of the water-vapor distribution can lead to errors in $T_{A,atm}$ because clouds may occur overhead which are not observed at other zenith angles, or vice versa. Errors of this sort are reduced if measurements are made at several zenith angles and the results are combined.

Measurements of $T_{A,atm}$ require accurate zenith-angle values. For example, if $T_{A,atm}$ is 10 K (a typical value for good weather conditions at high altitude) and if measurements of the sky temperature are made at zenith angles $Z_1 = 50^\circ$ and $Z_2 = 0^\circ$, then every arcminute of error in Z_1 causes an error of 10 mK in the measured value of $T_{A,atm}$. Our measurement strategy, which requires that the radiometers be mounted on carts and rolled into place for measurements, compounds the problem because radiometer cannot easily be accurately leveled under these conditions.

Fortunately, there is a solution: Zenith scans are made in opposite directions and the results are combined. This procedure removes the first-order error in $T_{A,atm}$ caused by the overall tilt of the radiometer. The residual error is roughly 10 mK for a 1° overall tilt and scales as the square of the tilt angle. Zenith scans in opposing directions have the added advantage that they remove some of the effects of the large-angular-scale sky-temperature variations caused by passing weather fronts.

Astronomical sources other than the CBR can contribute to T_{Zenith}. The sun and moon both have antenna temperatures much higher than that of the surrounding sky. Measurements of T_{CBR} must be made at times when the sun and moon are far enough from the part of the sky observed by the antenna so that they do not contribute significantly to the measured zenith or atmospheric temperature.

Radiation from the galaxy is a serious source of contamination at wavelengths longer than 3 cm. Figure 2.4 shows typical values of several sources of galactic radiation measured near the galactic plane, plotted as a function of wavelength. 3.3 mm lies in a spectral window: Thermal emission from ionized hydrogen and nonthermal synchrotron emission from cosmic-ray electrons, important emission mechanisms at longer wavelengths, both drop off rapidly with decreasing wavelength; thermal emission from dust grains rises with decreasing wavelength, but it is also insignificant at 3.3 mm. None of these sources of radiation is believed to be significant, or even detectable, in measurements of T_{CBR} at 3.3 mm.

An accurate determination of T_{CBR} requires precise knowledge of the radiometric temperature of the cold load $T_{A,Load}$; any error in its assumed value causes an equal error in $T_{A,CBR}$. $T_{A,Load}$ is determined not only by the temperature of the nominal target (generally the boiling temperature of the cryogen in which the target is immersed) but also by the radiation which comes to the antenna from sources other than the target. Included in the second category are radiation emitted by the (relatively) warm walls and windows of the cold load, and radiation from warm sources at the top of the cold load, such as the radiometer itself, which is reflected back into the antenna by the cold-load windows or target.

Finally, a measurement of T_{CBR} requires accurate knowledge of G, the radiometer calibration coefficient. The radiometer needs to be calibrated accurately enough so that uncertainty in G does not contribute substantially to the uncertainty in T_{CBR}, and frequently enough so that gain variation between successive calibrations does not degrade the measurement.

Once these various terms are known, they can be used to calculate T_{CBR}. In a simplified

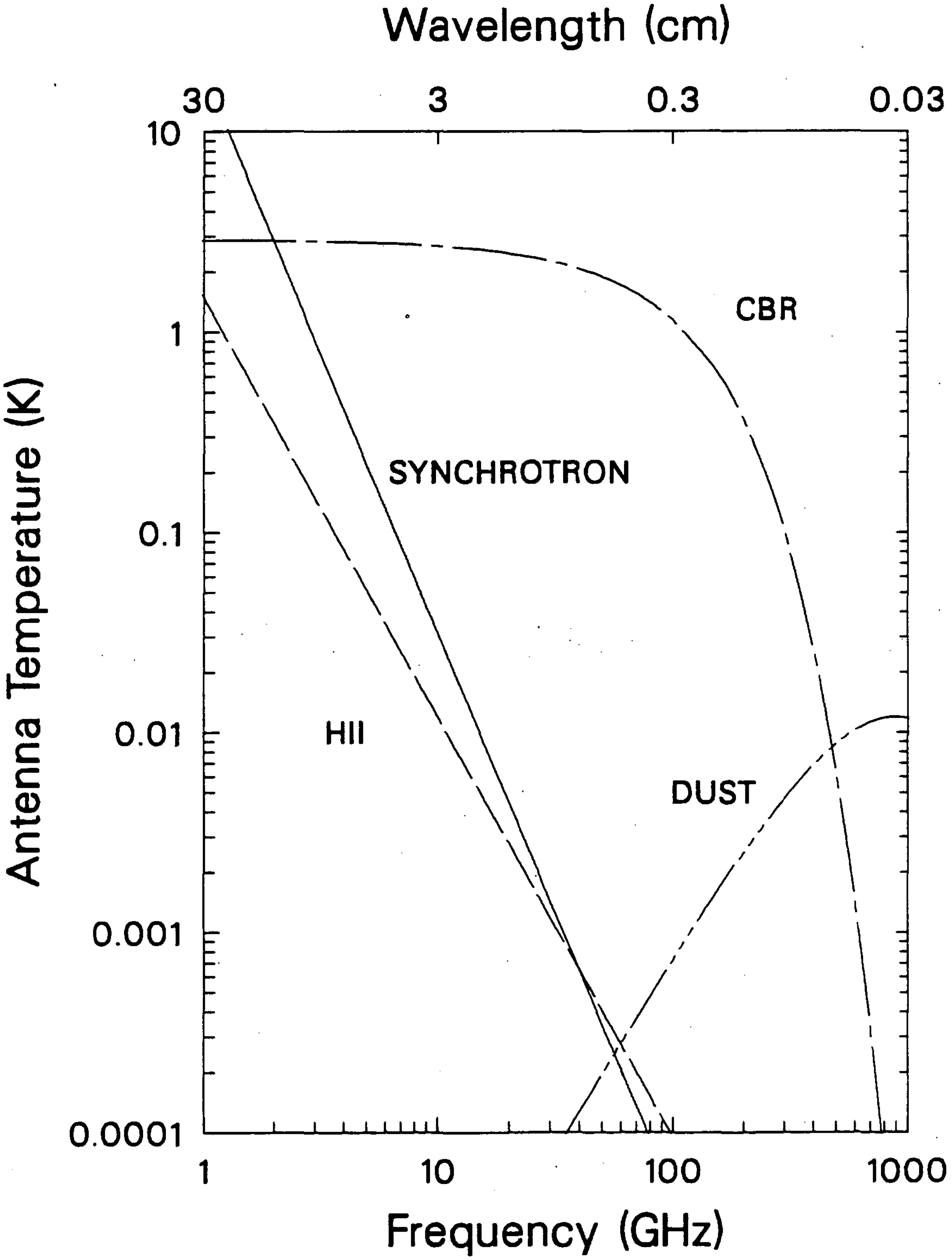

Figure 2.2: CBR signal and competing backgrounds. Galactic backgrounds are for a 7° beam viewing the galactic equator.

form and with instrumental corrections omitted, the equation used to derive $T_{A,CBR}$ is

$$\begin{aligned} T_{A,CBR} = \frac{G}{2}(V_{Zenith/Load} - V_{Load/Zenith}) + T_{A,Load} - T_{A,atm} \\ - T_{Ground} - T_{Sun} - T_{Moon} - T_{Galaxy} \, . \end{aligned} \tag{2.6}$$

Chapter 3

Description of Apparatus and Procedures

3.1 Choice of Observing Site

An observing site used for measurements of the CBR temperature must meet a number of requirements. A high-altitude, low-humidity environment is needed to minimize contamination of the signal by atmospheric emission. The horizon should be low enough so that radiation from the surroundings does not interfere with atmospheric zenith scans. The site must be accessible by truck since the radiometers, cold load, cryogen, and auxiliary equipment must all be brought in. In addition, electrical power, water, and accomodations are necessary for the health and well-being of the experiment and the experimenters.

We chose to make our observations from the Barcroft Laboratory of the White Mountain Research Station, near Bishop, California. This site has been used by a number of researchers over the years for measurements of T_{CBR} (Ewing *et al.* 1967; Stokes *et al.* 1967; Welch *et al.* 1967; Wilkinson 1967). It is situated on the central ridge of the White Mountains at an altitude of 3800 meters.

The White Mountains are in the rain shadow of the Sierra Nevada range some 35 km to the west. As a result, the humidity is typically much lower in the White Mountains than in the Sierras—the measured column density of precipitable water vapor can be less than 0.1 gm/cm^2 (1 mm precipitable H_2O) on a dry summer day. Furthermore, the relatively light snowpack and gentle terrain allow easier access to high-altitude sites in the White Mountains than to sites at comparable altitudes elsewhere in California.

Barcroft Laboratory is a well-developed facility, accessible by road from June through October. It is provided with laboratory space and simple shop equipment as well as living and sleeping quarters. Electrical power is supplied by a diesel generator. A helpful and able crew provide assistance when needed, and a cook is on hand to prepare meals. Besides these amenities, Barcroft Laboratory has the signal advantage that it is sheltered from most sources of manmade radio transmission. Aside from a radio telephone and a microwave oven, both of which are turned off during radiometric measurements, no strong sources of radio interference have been identified.

The site chosen for the observations is a relatively flat stretch of ground just below and to the southeast of the Barcroft Laboratory. Its horizon elevation is 18° or less in all directions—the highest point is in the direction of Mount Barcroft to the west. A portable storage shed, used to house power supplies, storage batteries, and data-recording equipment for the Berkeley radiometers, sits approximately five meters southeast of the cold load.

3.2 System Overview and Layout

The shared cold load is too heavy and awkward to be moved from one radiometer to another. Instead, the radiometers are mounted on carts which allow us to wheel them from place to place. We have mounted the cold load in a hole in the ground, suspended below the center section of a 20-meter-long set of tracks running east-west. The radiometer carts, which comprise the rolling stock of the White Mountain Shortline Railroad, are set on the tracks. This arrangement allows the radiometers to be moved quickly into position over the cold load. The 3.2-cm atmospheric monitor, which does not need access to the cold load, is fixed in place approximately ten meters southwest of the cold load.

A radiometer is rolled into place over the cold load in preparation for CBR measurements. Once there, it stays in position for a period of 40 to 60 minutes while measurements are made. It is aimed sequentially at the cold load below and the zenith above in order to measure T_{Zenith}, and sometimes at additional zenith angles for measurements of $T_{A,atm}$. Immediately after the observing run ends, the radiometer is rolled off the cold load to make room for the next instrument.

Efficient use of the limited observing time requires a carefully planned observing schedule and coordinated movement of the radiometers. The observing schedule has to allow for the transit of the galaxy and moon during the course of the night and also for the gradual drop in atmospheric water vapor which often occurs after sunset; all of these phenomena can affect the accuracy of CBR measurements at the various wavelengths. In addition, the order in which the radiometers are placed on the tracks must be considered; the carts cannot be quickly rearranged or removed from the tracks.

3.3 Liquid-Helium Cold Load

The liquid-helium cold load serves as a standard against which the radiation from the sky is compared, so its radiometric temperature must be known with great accuracy. Therefore, its design should reduce the inherently uncertain temperature contributions from the walls and windows to a low level. There are two basic, conflicting requirements for a good liquid-helium cold load. First, it should provide the radiometer with a clear, unobstructed view of the cold target. Second, the heat leak into the cold load should be as low as possible so that cryogen is conserved; liquid helium's low heat of vaporization (1.4 liter/hour/watt in practical units) and high cost (≈$4/liter) makes the insulation of the cold load an important consideration. The requirements come into conflict because on the one hand, the uninsulated aperture of a large cold load can act as a heat leak of 200 watts or more, while on the other hand, insulating material located between the mouth and the target of the cold load can significantly degrade the load's radiometric performance.

Our cold-load design is a compromise between the thermal and radiometric requirements. The radiometer views the target through two windows of thin polyethylene film; nothing else intervenes. Emission from the windows increases T_{Load} by no more than 18 mK at wavelengths of 3.3 mm or longer. The reflection coefficient of the cold load is less than 10^{-3} (VSWR less than 1.065) at all the measurement wavelengths. When the cold load is not actually in use, the heat leak to the cryogen is between 10 and 15 watts.

The design also seeks to maintain an airtight seal between the interior of the cold load and the surrounding air. The seal is necessary to prevent the formation of water and oxygen frost on the cold surfaces inside the load. Such frost could significantly increase the thermal emission from the walls of the load.

The target is contained in a cylindrical, open-mouth, liquid-helium cryostat with a 76-cm inner diameter and a 130-cm depth. The vacuum-insulated cryostat, shown in Figure 3.1, has

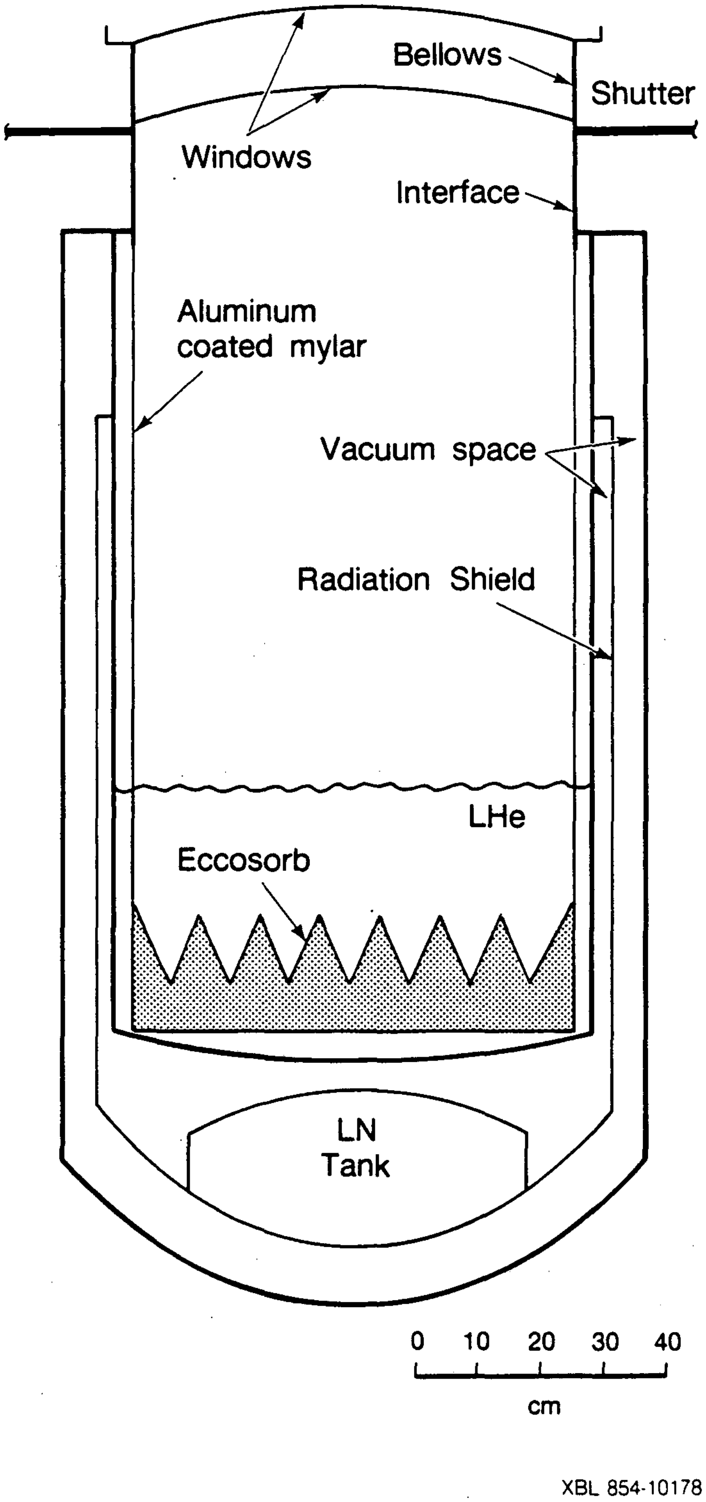

Figure 3.1: Liquid-helium cold load

an inner wall of stainless steel and an outer wall of aluminum which are joined at the top of the vessel by an aluminum flange. The space between the two walls is kept in vacuum to reduce heat transfer to the inside. An aluminum heat shield in the vacuum region intercepts the radiation emitted by the outer wall. The shield is attached to the inner wall, in good thermal contact with it. A liquid-nitrogen (LN) tank on the bottom provides the shield with active cooling when needed. Both the inner cryostat wall and the heat shield are wrapped with aluminized-mylar superinsulation—twenty layers on the inner wall and fifteen on the heat shield—to further reduce the radiative heat leak into the cryostat. When the cryostat is filled with liquid helium, cold boil-off helium gas cools the upper portion of the inner wall as it flows out of the cryostat, and the wall then cools the heat shield by means of the thermal short at the attachment point. This passive cooling mechanism maintains the heat shield at cryogenic temperatures during liquid-helium operations.

Attached to the floor of the cryostat is a target of Eccosorb VHP-8, a microwave absorber with emissivity greater than 0.999 at wavelengths from 0.33 to 12 cm. The target is a disk with a diameter of 70 cm and a 20-cm nominal thickness. The upper surface of the Eccosorb is formed into an array of tapered pyramids to reduce the reflection.

A cylinder of aluminum-coated mylar film 70 cm in diameter is mounted concentric with the cryostat inner wall. This cylinder, which encircles the target at the bottom and extends up through the top of the cryostat, serves as the radiometric wall of the load. It is held in tension between attachment points at the target and at the top of the cryostat. The thickness of the mylar film is 25 μm; the chemically deposited aluminum coating is 13 μm thick. The upper end of the coated-mylar cylinder is attached to an interface cylinder mounted on the top of the cryostat. The interface is 15 cm high with a 70-cm inner diameter.

Numerous components are mounted in the space between the cryostat wall and the radiometric wall: level sensors for both LN and LHe, heating resistors mounted on the bottom of the cryostat, temperature sensors attached to the target and to various points on the radiometric wall. The wires carrying power to the heaters, level sensors, and temperature sensors are all confined within that region and emerge through the lower flange of the interface cylinder; tubes used to transfer cryogen and boil-off gas in and out of the cold load follow the same route. Boil-off gas from the main volume of the cold load passes through small holes in the radiometric wall to reach the vent tubes.

Above the interface is a shutter designed to reduce the radiative heat flux entering the cryostat when the load is not in use. The shutter is a rectangular aluminum sheet 170 cm long by 85 cm wide, housed in an airtight aluminum case. The sheet is mounted on runners which allow it to move lengthwise inside the case. A push rod is used to move the sheet into its open and closed positions. When the shutter is open, a large circular hole in the sheet provides an unobstructed view of the Eccosorb target. An aluminum ring 70 cm in diameter by 2.5 cm high, mounted in the hole, spans the gap between the top and bottom of the shutter case to provide RF continuity. In the closed position, the solid portion of the sheet covers the top of the cryostat. Attached to its bottom surface is a square sheet of styrofoam, 1.3 cm thick, whose lower surface is covered by aluminized mylar. The mylar-covered styrofoam sheet prevents thermal radiation from entering the cryostat and presents an insulated, low-emissivity surface to the target and the cryogen.

Mounted on top of the shutter is another cylinder, 16 cm high by 69 cm in diameter, known colloquially as the "bellows". This cylinder allows the top surface of the cold load to be moved up and down when the radiometers and the load are coupled or uncoupled. When the antenna views the cold load, the load must be brought into contact with the antenna to assure that no RF power enters the antenna from outside sources. When the antenna is rotated to or from another position, the top of the load must be moved downward to provide clearance. The height of the bellows can be adjusted because the top cylinder is not directly attached to the shutter housing beneath it; instead, it is connected to a set of four vertical spring-loaded shafts located around its periphery. The shafts, which have three centimeters of travel, are mounted on a circular flange bolted to the top of the shutter. A metal band attached to the flange clamps around the circumference of the cylinder to bridge the gap that occurs when the bellows is raised.

A thin window between the shutter and the bellows seals the top of the cold load against air inflow. The window prevents frost from forming inside the cold load, but the window itself is susceptible to frost or dew formation if its cold surface is exposed to damp air. Therefore, a second window is installed at the top of the bellows to prevent frost formation on the lower window. Part of the vent gas from the cold load is heated and then passed through the region between the upper and lower windows, where the warm, dry gas heats the upper window enough to prevent condensation. Both windows are made of linear low-density polyethylene film 23 μm thick.

When one of the radiometers views the cold load, a set of circular plates couples the antenna to the top of the load and shields it from extraneous microwave radiation. Each plate has a central hole whose diameter matches that of the antenna with which it is used. The largest of the plates is used to couple the antenna of the 6.3-cm radiometer to the cold load; it sits in a circular depression in the top of the load. (The antenna used in the 12-cm radiometer has the same inner diameter as the cold load itself, so it needs no coupling plate.) The coupling plate for the 3-cm radiometer nests in the central hole of the larger plate. A lip around its circumference prevents it from falling into the hole. Even smaller coupling plates are used with the 0.91-cm and 0.33-cm radiometers. Each of them fits into the central hole of the 3-cm-radiometer coupling plate.

In order for a radiometer to couple to the cold load, contact must be maintained between the coupling plate and the lower sections of the cold load as the coupling plate is raised to the height of the antenna mouth. The 12-cm and 6.3-cm instruments both originally used the bellows to perform this function, but the time needed to raise and lower the bellows makes its use impractical for the smaller radiometers, so another mechanism has been devised. A thin, concentric cylinder is mounted on the bottom of the 3-cm-radiometer coupling plate. The ring sits in the central hole of the larger plate and acts as a guide, maintaining contact and preventing lateral motion when the coupling plate is raised and lowered. When the 0.33-cm or 0.91-cm radiometers use the cold load, their coupling plates sit in the plate for the 3-cm radiometer and they are raised and lowered together. The cylindrical guides proved so useful that in 1983 guides were installed on the coupling plates used with the 6.3-cm and 0.33-cm radiometers as well.

3.4 Radiometer Description

3.4.1 Overall Design

Figure 3.2 is a schematic diagram of the radiometer and its associated hardware. The radiometer is mounted between two aluminum reflectors on a cart. The reflectors and radiometer are mounted on bearings which permit them to rotate. Two oppositely directed antennas act as input ports for the radiometer; both antennas play equivalent roles during observations. The antennas can either point vertically to view the zenith and the cold load or horizontally to view the mirrors, depending on the orientation of the radiometer. The reflectors, which function as microwave mirrors, are used for measurements of atmospheric emission. Each can be set at a number of angles to allow each antenna to view the atmosphere at nominal zenith angles of 0°, 40°, or 50°.

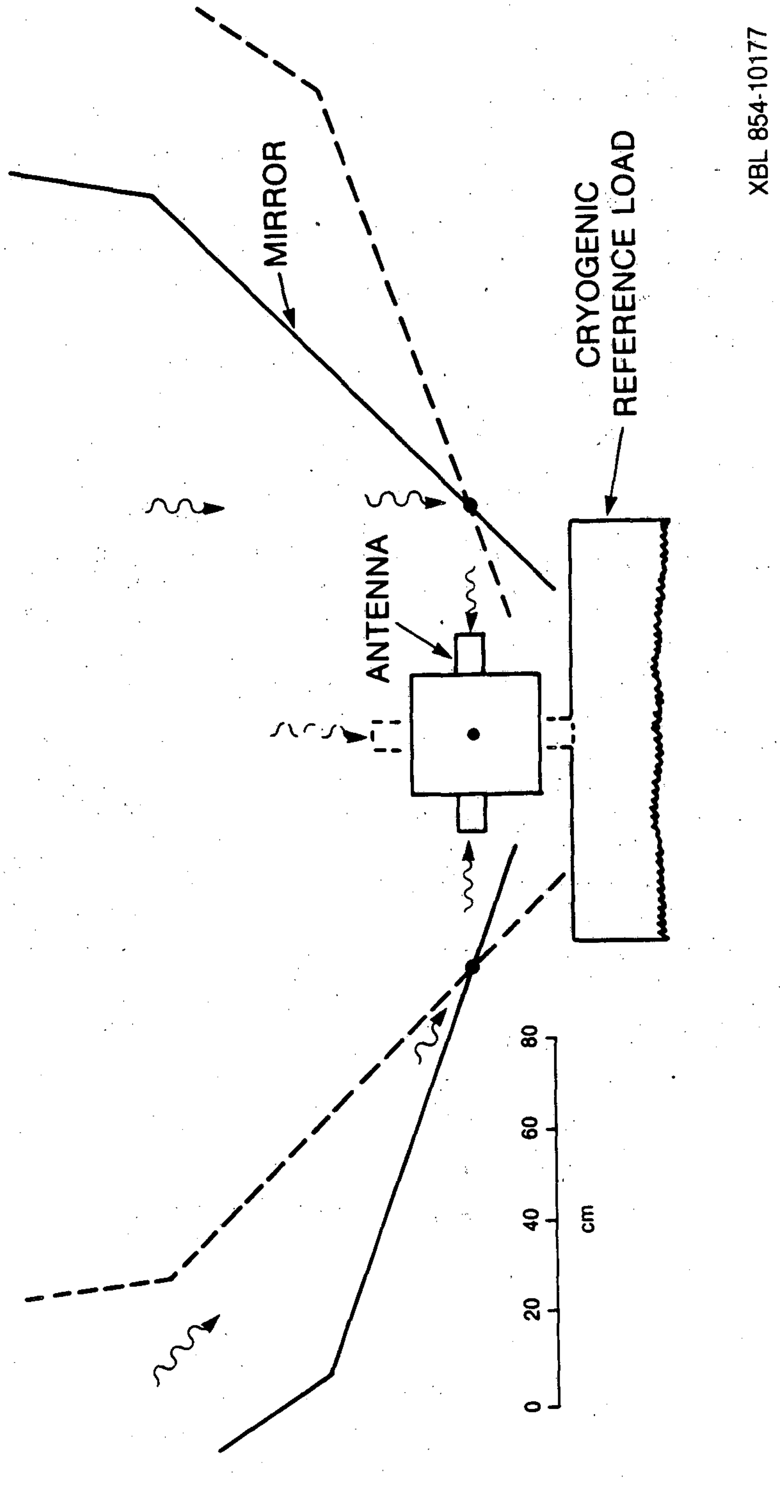

Figure 3.2: Schematic of the radiometer in its 1982 configuration.

3.4.2 Front End

A block diagram of the radiometer is given in Figure 3.3. Appendix B lists the manufacturers and model numbers of the front-end and IF components. The radiometer antennas are corrugated conical horns with half-power beamwidths of 7.5°. Antennas of this design have been used in a number of experiments, including measurements of the CBR anisotropy at 3.3 mm (Lubin, Epstein, and Smoot 1983) and 9.1 mm (Gorenstein and Smoot, 1981). The gain pattern for a scaled replica of the horn, measured at a wavelength of 9.6 mm, is shown in Figure 3.4.2(Jansen *et al.* 1979).

A tapered mode transition at the throat of each antenna converts the linearly polarized radiation from TE_{11} mode in the circular waveguide at the antenna throat to TE_{10} mode in the WR-10 rectangular waveguide used elsewhere in the receiver. The reflection coefficients of the antennas are $1.1 \pm 0.1 \times 10^{-2}$, measured at the output port of the waveguide transition.

The reflectivity and thus the emissivity of a conductor varies with the angle of incidence and with the polarization of the wave relative to the plane of incidence (Lorrain and Corson 1970). With the E-field perpendicular to the plane of incidence, the emissivity is proportional to $\cos(\theta_i)$, where θ_i is the angle of incidence measured relative to the surface normal. If the E-field is parallel to the plane of incidence on the other hand, the emissivity is proportional to $\sec(\theta_i)$. In the radiometer configuration used for the 1982 measurements, both the antennas are oriented with their E-plane polarization vectors 27° from horizontal when the antennas point horizontally (i.e. 27° from perpendicular to the plane of incidence). This orientation gives the minimum variation in reflector emissivity at the various incidence angles used for zenith scans. A 60° H-plane bend connects each of the mode transitions to the Dicke switch. (The bends are needed because the input ports on the switch are canted by 60° relative to each other, while the antennas are pointed 180° apart.)

The Dicke switch is a 3-port latching ferrite circulator. Two of the ports accept input power while the third acts as the output port. In each of the two switch states, only one of the input ports can pass power to the output port. A magnetized ferrite post in the center of the circulator causes power to flow through the circulator in only one direction, clockwise or counterclockwise, and to enter and leave through adjacent ports. The direction of the power flow is determined by the direction of the ferrite's magnetization, which is reversible; when the magnetization is reversed, the flow direction is reversed and the switch state changes. A shield of high-permeability iron around the switch reduces the influence of stray magnetic fields on the switch's ability to direct the flow of microwave power.

The switch is driven by a square-wave signal at 100 Hz. The rising and falling edges of the square wave activate electronic triggers which change the switch state. A single 100-Hz oscillator provides the switching signal for all the Berkeley radiometers and also provides timing pulses for the data-recording system.

The insertion loss of the Dicke switch over the wavelength range from 3.30 to 3.37 mm (89 to 91 GHz) is measured by the manufacturer to be less than 0.95 dB; the reverse isolation, measured over the same range, is greater than 20 dB; and the VSWR at all ports is 1.22:1 or less. The temperature offset of the switch is approximately 8 K when the radiometer views matched 77 K loads.

An isolator is mounted between the switch and the mixer to intercept any local-oscillator power that may leak through the mixer into the RF circuit. The isolator is actually a three-port circulator with an ambient-temperature termination on one of its ports. It is similar in design to the Dicke switch, but the magnetization of its ferrite is permanently fixed. Power entering its input port is passed to its output port, but power entering its output port is absorbed by the termination. Its insertion loss is approximately 0.8 dB, its reverse isolation is greater than 20 dB, and its VSWR is less than 1.3:1 at all three ports. Two layers of Mu-metal foil (a

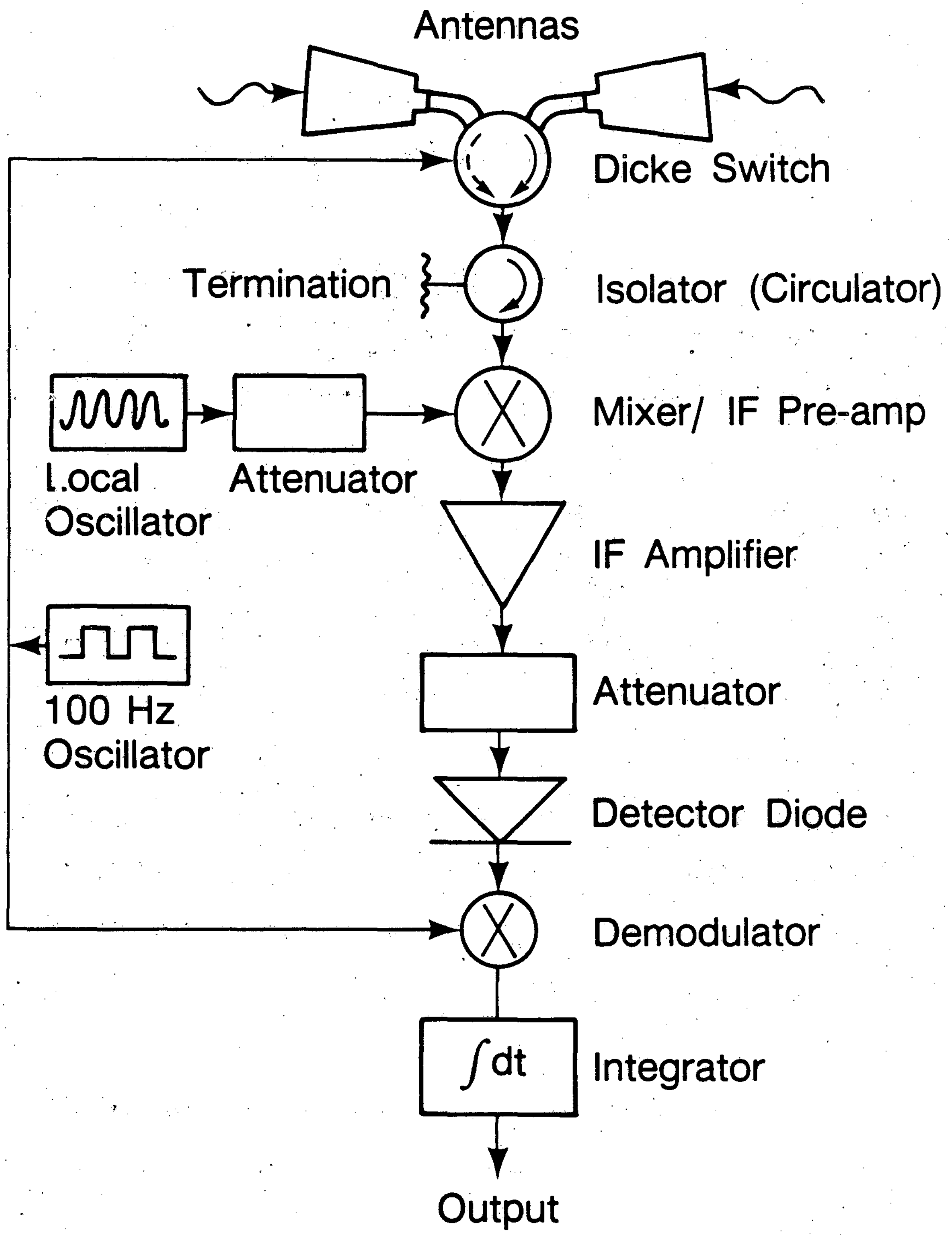

XBL 854-10179

Figure 3.3: Radiometer block diagram (1982 configuration).

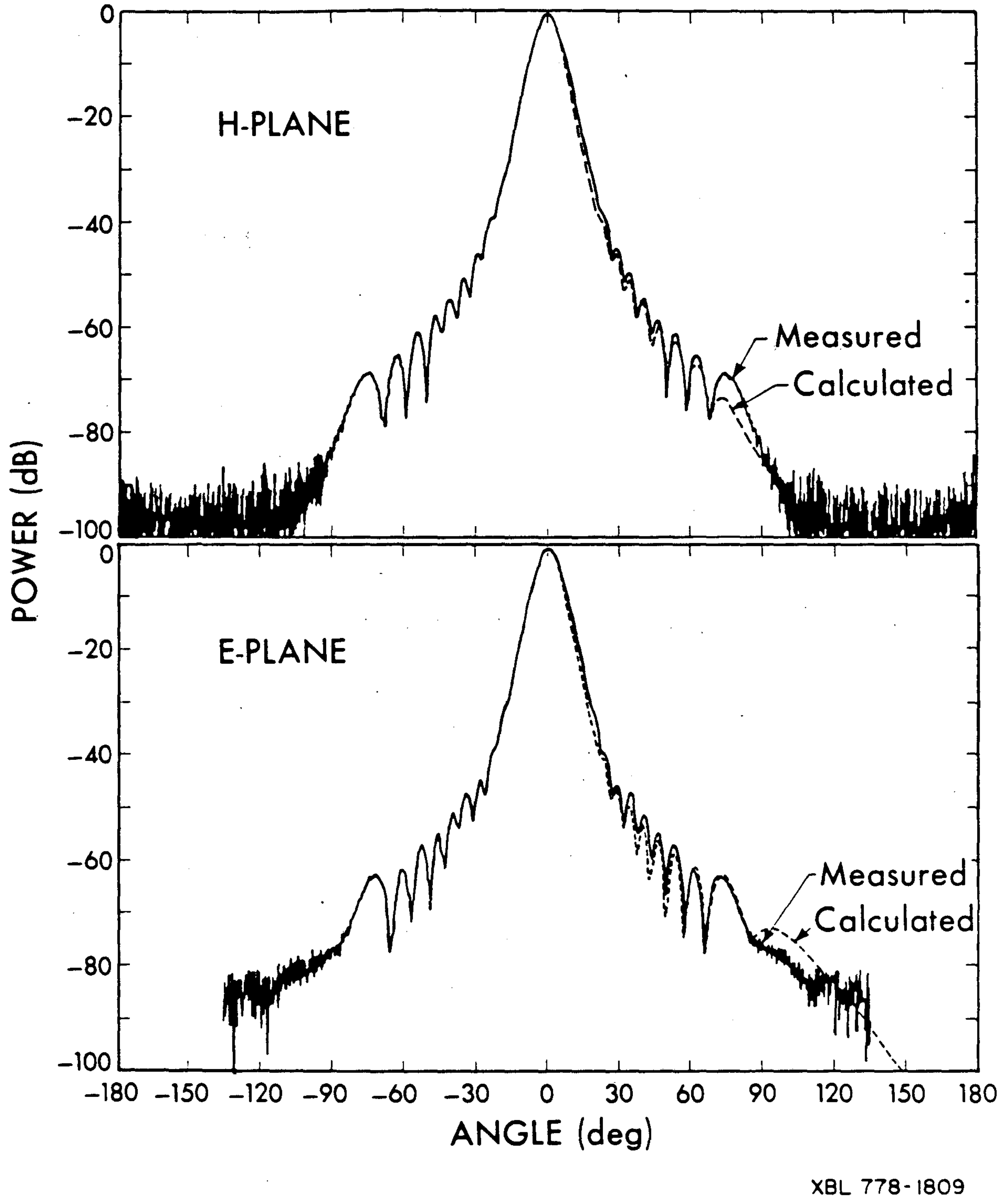

Figure 3.4: Antenna beam patterns. Data shown are for a proportionally scaled horn at 9.6 mm; the 3.3-mm beam patterns are essentially identical.

high-permeability iron alloy) shield the circulator from stray magnetic fields.

The balanced mixer uses a matched pair of beam-lead gallium-arsenide Schottky diodes as mixing elements. The diodes are biased by a DC current as well as by the microwave signal from the local oscillator (LO). RF power enters the mixer through one arm of a folded magic-tee junction and LO power enters through a second. The fields combine in the magic tee and exit through the two other ports of the junction, phased so that the LO fields in the two output ports are in phase but the RF fields are 180° out of phase. The fields cause the waveguide-mounted mixer diodes in each output port to produce currents at the difference frequency of the LO and RF fields (actually a superposition of difference frequencies, since what enters the RF port is a superposition of frequencies). Because of the relative phasing of the fields at the two diodes, the currents are out of phase with one another. Noise power in the sidebands of the local-oscillator signal is also downconverted by the mixer diodes, but the resulting currents from the two diodes are in phase. A built-in low-noise differential amplifier generates an output voltage proportional to the out-of-phase component of the two currents, thereby suppressing LO noise. The IF output port of the unit is a coaxial SMA connector.

The mixer has an RF bandwidth of approximately 2 GHz (DSB) centered at 90 GHz (3.33 mm); the IF band covers the frequency range from 0.1 to 1.0 GHz. The RF input VSWR is less than 2.0:1 over the passband; the RF/LO isolation is 25 dB. The gain of the built-in first-stage IF preamplifier is between 30 and 35 dB.

The DSB spot noise figure quoted by the manufacturer ranges from 4.8 to 5.7 dB over the IF range, with a typical value of about 5.1 dB. (These values include the contribution from IF amplifier.) The equivalent system noise temperatures are 600 to 815 Kelvins, with a typical value of 670 K. Our measurements of the mixer's broadband noise temperature, measured at the mixer RF port with 295 K and 77 K loads, yield values between 880 K and 930 K. The source of the discrepancy has not been resolved, but the values quoted by the manufacturer are definitely too low.

The local oscillator used with the mixer is a cavity-coupled, mechanically-tuned Gunn oscillator, set to a frequency of 90.0 GHz. A variable attenuator reduces its 17-mW output power to the 3 mW level required by the mixer.

3.4.3 IF and Back End

Output power from the IF preamplifier enters a second amplifier where it is boosted by another 37 dB. It passes through an 8-dB attenuator into a crystal detector diode where the waveforms are rectified. The detector produces a DC voltage between −9.8 mV and −11.7 mV when the radiometer views a load with a temperature between 0 K and 295 K. These voltages lie within the linear response range of the detector.

The lockin amplifier produces a DC voltage proportional to the amplitude of the square-wave-modulated voltage from the detector. Its broadband synchronous filter compares the time-varying component of the detector output voltage with the square-wave signal driving the Dicke switch. The component of the detector voltage that varies in phase with the square wave is amplified, demodulated, and integrated by a boxcar integrator with a two-second time constant. Multiple amplifier stages both before and after the synchronous filter boost the DC output voltage from the integrator by a factor of 4500 relative to the peak-to-peak amplitude of the input waveform. The output range of the lockin amplifier is ±10 V.

3.4.4 Temperature Regulation

A temperature-regulated 12-watt heater reduces the influence of ambient-temperature variations on radiometer performance. Over a ±4 K range in the ambient temperature, the temperature of the mixer, IF amplifiers, and lockin amplifier remains constant to within ±0.2 K. The heater is controlled by a thermostat whose sensor is a thermistor located near the mixer. The regulation point of the thermostat is adjustable from 0 °C to 30 °C to permit temperature regulation over a wide range of conditions. Four additional temperature-sensing circuits monitor the temperatures of both antennas, the Dicke switch, and the mixer. These temperatures are recorded along with the radiometer output.

3.4.5 Mechanical Structure

The mixer, IF amplifiers, detector diode, and lockin amplifier are all mounted on a 13-cm by 18-cm aluminum plate, the front-end components on the upper surface of the plate and the lockin amplifier below. The Dicke switch and local oscillator are held above the plate by mounting brackets and the isolator is fixed in position by its waveguide connections to the mixer and switch.

A rectangular metal case houses the radiometer. The case, made of aluminum plate, not only shields the instrument from radio interference in the IF band but also forms an integral part of the radiometer mounting structure. The front-end plate is bolted to it, and the antennas, which emerge from the case through cylindrical sleeves, are held fixed to it by three set screws around the circumference of each sleeve.

Shaft-and-bearing assemblies on two sides of the case allow the radiometer to rotate. During measurements, the instrument is held fixed by a pin which passes through a guide hole in one of the bearing mounts and through a matching hole in a rotating positioning plate mounted on the shaft. Holes drilled in the positioning plate allow the radiometer to be set in each of its measurement positions. The bearing mounts are separated from the cart by fiberglass-epoxy standoffs which provide thermal and electrical insulation between the radiometer and the cart.

Electrical cables enter the case through a hollow shaft that passes through one of the bearings. They carry power, the 100-Hz switching signal, the lockin output voltage, and housekeeping information from the heater and temperature sensors. A metal box on the stationary side of the bearing holds the power supplies for the local oscillator, the mixer, the IF amplifiers, and the temperature sensors.

The reflectors used for measurements of $T_{A,atm}$ should allow the zenith angles to be set with an accuracy of ±3 arcminutes. In order to provide the needed accuracy, the reflectors must be flat, stiff, and light enough not to bend under their own weight. Another reason for the reflectors to be lightweight that they need to be moved quickly and easily from one position to another during measurements. To satisfy these requirements, we have made the reflectors from 1-inch panels of foamed polyurethane faced on both sides with aluminum sheet. Lengths of 1-inch aluminum channel encircle the perimeters of the panels. The facing sheets, which overlay the foamed panels and the channel segments, are 122 cm long and 91 cm wide. They are glued to the panels and bolted to the channel pieces. 30-cm extensions on the far ends of the reflectors help to shield the antennas from radiation produced by sources near the horizon. The flat sheet-aluminum extensions have the same width as the reflectors and extend upward at a 30° angle to the reflector surface.

The cart holds the radiometer and reflectors in their proper positions while allowing the whole assembly to be moved rapidly on and off the cold load. It is a rectangular frame made of aluminum channel, mounted on a set of vee-groove wheels which ride on a ridge along the center of each track. The grooved wheels allow the cart to roll along the track but prevent it from moving in the transverse direction.

The two reflectors are mounted on the cart equidistant from the radiometer. When the antennas are pointed horizontally, the horizontal distance from the antenna mouth to the reflector is 28 cm. The upright supports that hold each reflector on the cart allow the reflector to pivot up and down for zenith scans. The pivot axis lies in the plane of the reflector, 27 cm from its lower edge. The rotation axes of the radiometer and both reflectors are at the same height, parallel to one another and parallel to the tracks. A pair of arms extending from the cart to the upper end of the reflector supports each reflector at the angles needed for zenith scans.

Figure 3.5 is a drawing of the radiometer and reflectors, mounted on the cart.

3.4.6 Ambient Calibrator

A small, insulated, ambient-temperature target is used to calibrate the radiometer. During calibrations, the target is placed in front of each antenna while the other antenna views the zenith. The output voltages produced by the radiometer are used to compute the calibration coefficient G. The 10-cm by 10-cm ambient target is cast from ferrite-loaded silicone rubber. An array of 2.5-cm cones cast into its front surface reduce its reflectivity below 3×10^{-3}. A layer of low-density styrofoam covers the front surface to insulate the target against changes in the ambient temperature. A styrofoam box covering the back and sides of the target provides added insulation. An electronic temperature-sensor on the back of the target allows its temperature to be monitored and recorded.

3.5 Data-Recording System

Data values from the radiometer are stored digitally on magnetic cassette tape. The tape records the radiometer output voltage, the temperatures measured at the the various sensors in the radiometer and the ambient calibrator, and the voltage applied to the heating resistors by the temperature regulator. Additional data concerning the orientation and status of the radiometer and reflectors are also recorded. The tape stores similar information from the 0.91-cm and 3.0-cm radiometers, as well as information about the cold load and the power supplies. Table 3.1 is a list of the devices whose output values are recorded on tape.

In order to record a large number of parallel analog data values on a sequential digital medium, the recording system must multiplex and digitize the voltage values before they are written onto cassette tape. The multiplexing circuit performs its task by sampling the voltage values sequentially during a sixteen-second period. Lockin output voltages are sampled every two seconds; other terms are sampled only once during the period. Voltages sampled by the multiplexer are digitized in a 16-bit analog-to-digital converter with a ±5 volt input range. Voltage-divider networks in the input circuits to the multiplexer reduce the voltages from the input devices to match the range of the A/D converter; for example, the lockin voltages are reduced by half so that the A/D converter can accomodate the full range of the lockin. The lockin-voltage values recorded on tape are quantized in data units of $10/2^{15}$ volts, or 0.31 mV.

Besides being stored on tape, the lockin output voltage is measured with a $4\frac{1}{2}$-digit digital volt meter and written down during measurements of T_{CBR}. One voltage value is recorded for each step in the measurement procedure; voltage fluctuations are averaged by eye. The temperature of the ambient calibrator is also written down once per measurement cycle. The hand-recorded table of measurement values provides a backup data source if the tape-recording system fails, and it is also useful for preliminary data analysis.

3.6 Electrical Power

The radiometers, heaters, data-recording system, and cold-load monitoring equipment are all powered by 12-volt deep-cycle lead-acid storage batteries. Pairs of batteries are connected in series to provide 24 volts. During use, they are connected to a battery charger to prevent them

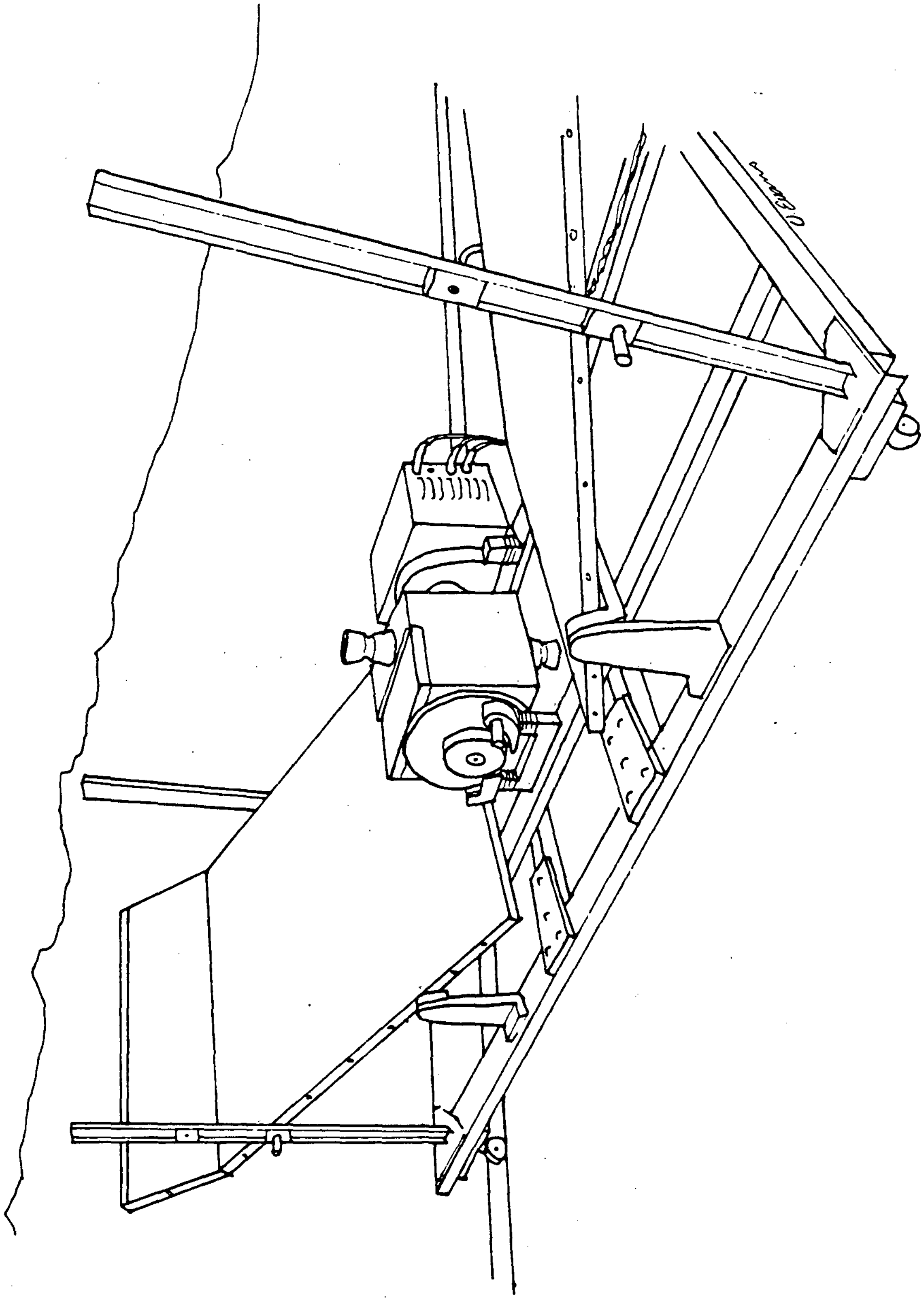

Figure 3.5: Drawing of the 3.3-mm radiometer and cart assembly.

Data Words	3.3 mm	9.1 mm	3.0 cm	Sampling Period (Seconds)
	Digital			
Universal Time: Day, Hour				16
Universal Time: Minutes, Seconds				16
Radiometer Position and Status Switches	x	x	x	16
Barometric Pressure				16
Atmospheric Monitor Scan Position				16
	Analog			
Lockin Amplifier Output	x	x	x	2
Temperature of Antenna 1	x	x	x	16
Temperature of Antenna 2	x	x	x	16
Temperature of Dicke Switch	x	x	x	16
Mixer/IF Amplifier Temperature	x	x	x	16
Support Electronics Temperature	x	x		16
Ambient Calibrator Temperature	x	x	x	16
Radiometer Heater Current	x	x	x	16
Support Electronics Heater Current	x	x	x	16
LHe Temperature Sensor 1				16
LHe Temperature Sensor 2				16
Cold Load Wall Temperature				16
LHe Level				16
Electronics Battery Voltage				16
Heater Battery Voltage				16
12-cm Radiometer Output				16
6.3-cm Radiometer Output				16
Atmospheric Monitor Output				16

Table 3.1: Data recorded on magnetic tape during 1982 measurements. The 1983 data format is similar.

from discharging. The batteries provide a steady voltage that drifts only slowly with time. The battery voltage shows no sign of ripple from the charger and is effectively decoupled from the AC line voltage, which is not only unsteady but undependable.

Care is taken to avoid supply-voltage fluctuations that could influence the behavior of the radiometer. The heaters and the electronics are powered by two separate sets of batteries so that radiometer operation is not affected by sudden changes in heater current. The effect of drifts in the battery voltage is minimized by voltage regulators which convert the battery voltage to the +15-volt, +10-volt, and −15-volt values required by the radiometer. Separate 15-volt regulators power the IF amplifiers and the Dicke switch in order to avoid the possibility of a low-level 100-Hz modulation on the voltage to the IF amplifiers which could give rise to a spurious 100-Hz variation in the output power from the amplifiers.

3.7 Measurement Procedure

The cycle used for CBR measurements in 1982 consisted of the following seven steps: 1. A measurement with one antenna pointed at the zenith and the other at the cold load; 2. The same measurement with the radiometer rotated by 180° so that the antennas were reversed; 3. A gain-calibration measurement with the antennas pointed horizontally, in which one antenna viewed the ambient calibrator and the other viewed the zenith through a reflector set at 45°; 4. The same measurement with the radiometer in the same position but the targets reversed; 5. A measurement of the sky in which one antenna viewed the zenith by means of a reflector and the other viewed a zenith angle of either 40° or 50° through the other reflector; 6. The same measurement but with the reflector settings reversed; 7. A measurement of the sky in which both antennas viewed the zenith by means of the reflectors.

Each cycle contained measurements at zenith angles of either 40° or 50° (steps 5 and 6). Most measurements were made at 50°, but occasional measurements at 40° served as consistency checks. Step 7 was not essential to the CBR measurement, but it provided a useful check on the stability of the radiometer offset.

The calibration coefficient was obtained from steps 1 through 4. The sum of the voltages from steps 1 and 3 yielded the voltage which would have resulted if the radiometer viewed the ambient and cold loads, and the sum from steps 2 and 4 yielded the voltage value with the targets reversed.

For measurements of $T_{A,atm}$ alone, a somewhat different cycle was used. The radiometer was pointed horizontally, and the sequence of reflector positions allowed each antenna to observe the sky at 40° and 50° nominal zenith angles while the other antenna viewed the zenith. For calibration, each antenna viewed the ambient calibrator while the other observed the zenith by means of the reflector; in this case, the sky was used as the calibration cold load. Even though its radiometric temperature was not precisely known, the sky could be used to calibrate the radiometer to better than 1%.

Chapter 4

System Operation, 1982

4.1 Radiometer Performance

The 3.3-mm radiometer underwent a series of tests to evaluate its performance and to search for potential systematic errors. Tests for systematic errors included measurements of the flip offset (caused either by magnetic fields or by mechanical stresses), the nonlinearity of the output voltage, and the radiometer's sensitivity to thermal emission received by the antenna sidelobes. Other tests measured the stability and temperature dependence of the calibration coefficient. Several of the tests used a DEC LSI-11/23 computer for data acquisition and analysis. A Fortran program, RADTST, instructed the computer to sample and record the radiometer output at 1-second intervals for a period of 1024 seconds (approximately 17 minutes). The stored data were then analysed to determine how the noise fluctuations varied with integration time and whether the data contained any periodic structure.

The radiometer noise temperature, measured with ambient and LN-temperature targets, was 1530 ± 20 Kelvins. The system noise fluctuations measured at White Mountain were 100 ± 2 mK for a 2-second integration period, significantly larger than the 71-mK value predicted by equation (2.4) for a Dicke radiometer with a nominal IF bandwidth of 950 MHz. The noise fluctuations decreased as the inverse square root of the integration time for periods of at least 8.5 minutes. The system offset was -7.1 ± 0.2 K.

The radiometer response at the detector diode output was 0.157 K/microvolt in the laboratory (operating temperature typically 27 ± 1 K). The response at the lockin output was 35.3 K/volt; the output from the A/D converter had a calibration coefficient G of 10.77 mK per digitized unit.

Over a period of 24 hours, the calibration coefficient was found to vary by 0.2% in a thermally controlled environment. The temperature dependence measured in Berkeley was +0.7%/K over the range from 21.6°C to 31.6°C. At White Mountain, the observed temperature dependence was $(+0.57 \pm 0.03)$%/K over the temperature range from 6.5°C to 19.6°C.

The influence of external magnetic fields on the radiometer's offset was of interest because the direction of the field seen by the radiometer changes when the radiometer is rotated. To test for magnetically induced offset changes, we placed the radiometer between two large Helmholtz coils whose fields were turned on and off every sixty seconds. The tests were performed outside on clear nights, with both antennas viewing the zenith by means of reflectors. The output values from the radiometer were stored in the computer and examined for modulations with the correct period and phase. A ten-Gauss field, either vertical or horizontal, changed the offset by less than 15 mK. Since the field seen by the radiometer changed by approximately one Gauss when the radiometer was rotated by 180 degrees, the largest magnetically induced flip offset that could occur during CBR measurements was less than 1.5 mK.

Mechanically induced flip offsets are generally caused by gravitational torques on the radiometer components and mounting. The only step in the measurement sequence vulnerable to flip offset was the measurement the measurement of T_{Zenith}, during which the antennas pointed vertically. Offset changes during this measurement are best evaluated with the radiometer in the correct orientation, but unfortunately, we had no matched cold loads suitable for that radiometer orientation.

Instead, we were forced to measure the flip offset with the antennas pointed horizontally. Reflectors in front of the two antennas caused them to view the zenith. The radiometer was periodically rotated on its bearings by 180 degrees, reversing the positions of the two antennas, and its output voltage was recorded and analyzed by the computer as described above. When the measurement was complete, the two reflectors were exchanged and the measurement was repeated in order to remove any offset due to the difference in the emissivities of the two reflectors. These measurements set an upper limit of 30 mK on the flip offset with the radiometer pointed horizontally. They served as an indication that the vertical flip offset was probably not a severe problem, but did not set a strong upper limit on it.

Measurements of the detector diode output response showed its nonlinearity to be less than 1% for output voltages up to 14 millivolts. Because of this good linearity characteristic, the radiometer was modified to raise the detector output voltage to 11.7 mV when the radiometer viewed an ambient load.

Thermal emission entering the antenna from the ground could not be easily estimated and subtracted from the results, so we conducted tests to make sure that the antennas were adequately shielded from ground radiation. We measured the ground pickup with the antennas pointed horizontally and the reflectors tilted back to simulate a 50-degree zenith scan (the position in which the radiometer is most sensitive to ground emission). An aluminum sheet held in the sidelobes of one antenna caused the antenna to see the reflected sky instead of the ground or nearby objects. The sheet was introduced and removed periodically, and the radiometer output was recorded. Measurements of sidelobe pickup from objects beside the antenna, below the antenna, and beyond the end of the scanning reflector were performed. These set an 8 mK upper limit on the contribution of ground radiation to the measured atmospheric emission. When the antennas were pointed vertically, ground pickup was completely negligible, since the horizon was at least 70° away from the axis of the upward-pointed antenna, and the downward-pointed antenna was shielded from the ground by the cold load.

4.2 Berkeley Dress Rehearsal

In June 1982 our collaborators from Milano, Bologna, and Haverford arrived in Berkeley with their equipment. The cold load and tracks were assembled at a test site at the Lawrence Berkeley Laboratory, complete with a hole in the ground to accommodate the cold load. After the cold load, rails, and radiometers had been fitted to one another, we tested the full system by measuring $T_{A,atm}$ and T_{CBR} from Berkeley, using first LN and then LHe as the cryogen in the cold load. This set of tests served several functions: First, it helped to identify and correct those things that were likely to cause problems at White Mountain. Second, it gave the participants some experience operating the radiometers and cold load as a system and some understanding of the procedures required (e.g. how to move the radiometers on and off the cold load quickly, how to couple a radiometer to the cold load without destroying either). In addition, it allowed us to measure the thermal performance of the cold load, which had improved significantly since we had last filled it with LHe.

Tests with LN on 12 and 13 June were largely successful. The heat leak into the cold load was approximately 14 watts, and the cold load and radiometers all functioned correctly and compatibly. The only major problem encountered was RF interference from transmitters in the area which prevented the 12-cm radiometer from obtaining useful data.

On 14 June we replaced the LN in the cold load with LHe and repeated the test. The performance of the LHe-filled cold load was a crucial unknown before the test, since the shutter and the vent system used to remove boil-off gas had only been tested with LN. Again the radiometers and the cold load behaved satisfactorily: The heat leak into the LHe was approximately 12 watts with the shutter closed, the shutter and the coupling system both worked smoothly, the vent gas was removed from the vicinity without excessively cooling the fittings around the top of the cold load or elsewhere, and there was not a serious frost-buildup problem on the windows or the inner wall of the cold load.

4.3 At White Mountain, 1982

Fresh from our triumph, we dismantled the tracks and packed up our equipment for the drive to White Mountain. After arriving on 25 June, we located a suitable site near Barcroft Laboratory, where we installed the tracks, cold load, and shutter, and mounted the radiometers on the tracks. Various system tests were repeated to verify that the equipment had not been damaged in transit. We used the radiometers to monitor the atmospheric emissivity at the various wavelengths from day to day, and we also measured the relative humidity and the water-vapor column density with other instruments.

On 29 June the cold load was filled with LN to check its thermal behavior and to prepare it for use. A snowstorm at the end of June delayed our progress by several days, but by 3 July the weather was good enough for us to conduct practice measurements of the CBR using LN.

During this period, the 3.3-mm radiometer developed a problem which ultimately compromised the quality of its measurement—the reflectors began to warp. The reflective aluminum sheets pulled away from the foamed plastic panels to which they had been attached, causing the reflective surfaces to bow outward. This warping, which was probably caused by diurnal thermal cycling, made it impossible for us to accurately determine the zenith angle viewed by the antenna.

The problem was compounded by the progressive nature of the deterioration. We could, in principle, have mapped out the surface variations over the reflectors and calculated the effective zenith angle viewed by each antenna. However, the zenith angle viewed by the antenna drifted from day to day as the warping progressed, and we had no way to make accurate angle measurements in the field. In any case, by the time we were ready to make CBR measurements, one of the reflectors varied in angle by 1.5 degrees over the surface viewed by the antenna main lobe. It would have been difficult if not impossible to make accurate corrections for a variation of this size.

We replaced the LN with LHe on 4 July and measured T_{CBR} that night and the next, as well as making additional measurements of atmospheric emission. Two series of CBR measurements were made the first night, the first starting at 08:43 UT and the second starting at 11:03 UT. Each one lasted about 50 minutes, and each one contained twelve to fourteen CBR measurements.

Small flakes of styrofoam from the ambient calibrator entered one antenna near the beginning of the second measurement series. These flakes lodged near the antenna throat, causing an irregular variation in the offset which rendered the data useless.

The styrofoam was removed from the antenna the next day, and CBR measurements were repeated that night. The first series started at 02:02 UT (near sunset) and ended at 02:58. The temperature controller on the radiometer was reset from 6.5°C (its normal value) to 19.6°C to allow it to maintain temperature regulation at the higher ambient temperatures of the early evening. Scattered clouds were observed during the run. An electronics failure in the data-recording system prevented the data from being recorded on cassette tape, but the hand-recorded values were accurate and complete enough to be used instead. The temperature regulator was reset to 6.5°C after the end of the first run. During the next few hours the electronics problem was corrected and the clouds dispersed, so that conditions during the second observing run (09:06 to 09:40 UT) were more nearly optimal.

The calibrator was filled with LN on 6 July and the CBR measurements were repeated that night and the next. The radiometer's horizontal flip offset was also remeasured to determine whether it had changed.

After the final tests and measurements, we packed the equipment and prepared to leave. The cold load and tracks, which were to be left there over the winter, were chained in place. The cold load was covered with sheets of plastic and plywood to keep out moisture, and the vacuum space in the cryostat was filled with dry nitrogen gas. The radiometers and other equipment were returned to Berkeley, and ultimately to their final destinations.

The data collected during our observations were reduced, analyzed and published after our return to civilization. Smoot *et al.* (1983) summarizes the project as a whole and lists the results at all five wavelengths. Other papers describe the individual radiometers and the data-analysis procedures used to derive T_{CBR} (De Amici *et al.* 1984; Friedman *et al.* 1984; Mandolesi *et al.* 1984; Partridge *et al.* 1984; Sironi *et al.* 1984).

As a postscript to the 1982 field operation, tests of the radiometer after our return revealed that both the isolator and the Dicke switch had been damaged, apparently during the trip back to Berkeley. These components were sent to their manufacturers for repair, and returned to us in working order with performance specifications similar to those of the previous summer. Several months later the mixer failed and was sent to Alpha Industries for repair. The mixer diodes were replaced and it was returned to us, still in a nonworking state. After several iterations of this process, Alpha succeeded in sending us a working mixer, with an 850 ± 10 Kelvin noise temperature (compared to the previous value of 910 ± 10 Kelvins) and an RF/IF gain which was 15-20% higher than its previous value.

Chapter 5

Radiometer Design Modifications, 1983

5.1 Shortcomings of the Old Design

Two major shortcomings in the initial radiometer design became evident at White Mountain and afterward. The reflectors, which were only marginally flat at the beginning, degraded with time. Furthermore, the reflector positions could not be reset quickly, so the rate at which we could make atmospheric scans was limited.

Analysis of the 1982 measurements indicated that most of the variation in the measured CBR temperature was caused by fluctuations in atmospheric emission. This finding led us to believe that the statistical uncertainty could be reduced if we measured the atmosphere more frequently and and made the measurements at two or more zenith angles to reduce the effect of the patchy water-vapor distribution. We therefore decided that a different approach to atmospheric measurements was necessary.

In addition, the system used to couple the antennas to the cold load did not function smoothly. The plate often jammed against the antenna as the coupling was made, causing much aggravation, lost time, and a certain amount of damage to the mouths of the antennas, whose delicate corrugations were periodically mashed against large pieces of aluminum.

5.2 Resulting Modifications

The problems we encountered with the original design prompted us to redesign the instrument; the modified radiometer is shown in Figures 5.1 and 5.2. The most important change in the radiometer was the altered topology of the antennas: The opening angle between the two antennas, which had previously been 180°, was reduced to 60°. This change allowed us to measure atmospheric emission by rotating the radiometer itself, thereby eliminating the need for tilting reflectors. The new design prevented the radiometer from directly measuring the temperature difference between the zenith and the sky at angles other than 60°, but this restriction was unimportant, since the temperature difference at any two zenith angles could in principle be used to determine the amount of atmospheric emission from directly overhead. The sensitivity of atmospheric measurements comparing zenith angles of 40° and 20° was a factor of 1.27 lower than the sensitivity of zenith scans comparing 40° to 0°; the sensitivity reduction for 50°/10° scans compared to 50°/0° scans was only 1.03. This loss of sensitivity was judged acceptable in light of the advantages of the new design.

The new antenna orientation also made the radiometer stiffer and more compact by eliminating the 60° waveguide bends between the Dicke switch and the antennas. The radiometer housing was shortened and reinforced to increase its stiffness, and the circulator was attached

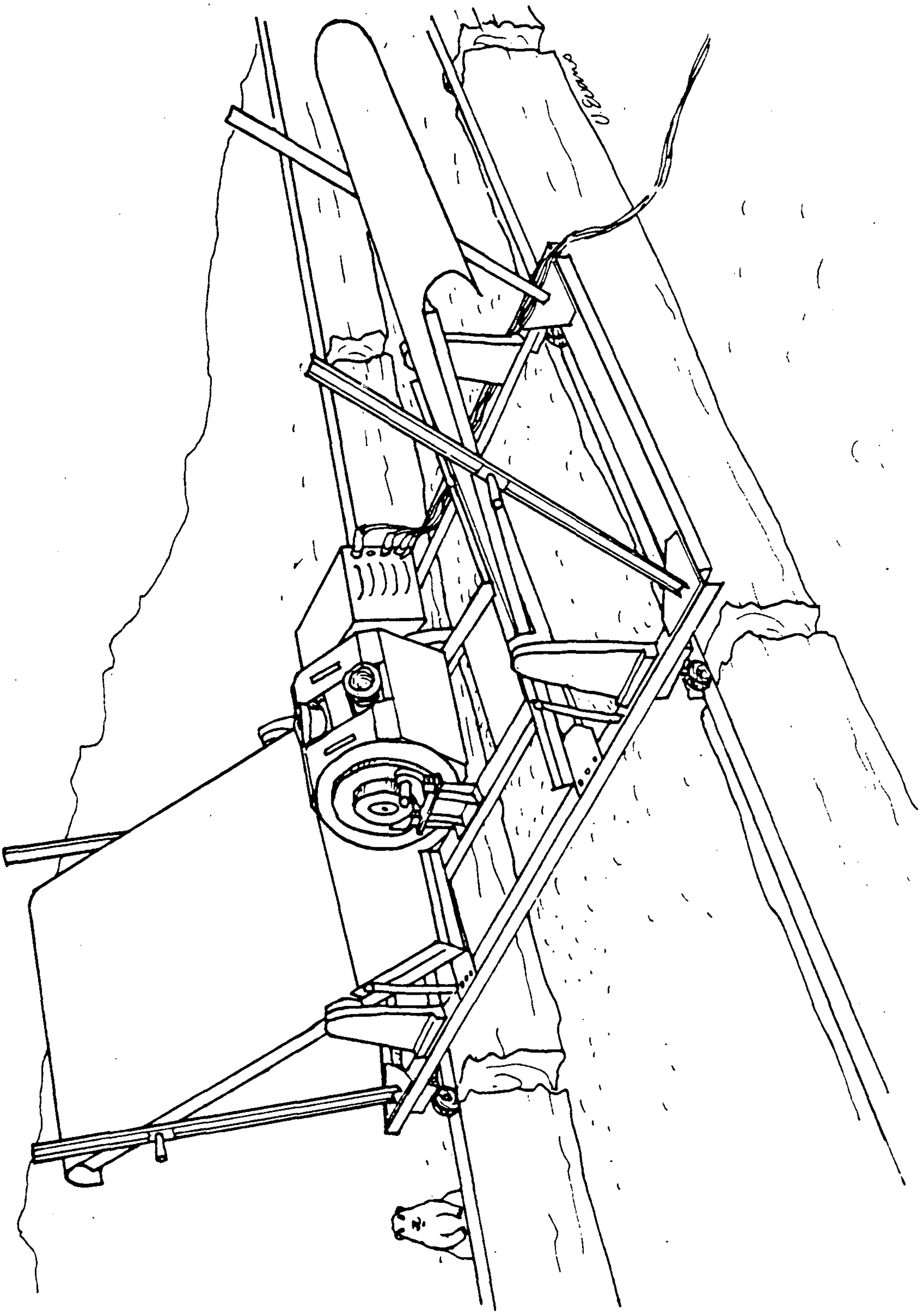

Figure 5.1: Drawing of the 1983-model 3.3-mm radiometer in place at White Mountain.

to a structural member instead of being held only by waveguide. A 30° bend was installed between the circulator and the switch to give the antennas the correct orientation relative to the radiometer's axis of rotation.

One result of these changes was that when one antenna pointed into the cold load, the other one no longer pointed upward. We therefore installed reflectors which allowed the antennas to view the sky during measurements of the zenith temperature. The reflectors were cut in the shape of the letter "T": The span across the arms was 91 cm, the width of the arms was 30 cm, and the height from base to top was 43 cm. The reflectors were made from sheets of alloy 1100 (commercially pure) aluminum for low emissivity and good resistance to oxidation. These were backed with sheets of a more rigid alloy for added strength. The pointing accuracy needed for vertical measurements accurate to 20 mK was only 3°, so no further stiffening was necessary.

The reflectors from the previous year were retained for use as ground shields during zenith measurements and atmospheric scans. Mounted parallel to and immediately behind the new reflectors, they extended 20° above the horizon as viewed from the throat of the antenna during an atmospheric scan. A curved extension was added to the ground shield to reduce the amount of ground emission diffracted over the far edge of the shield during atmospheric scans (Kellner 1957). Small shields were also installed below the reflectors, parallel to the ground. The radiometer, reflectors, and ground shields are shown in Figure 5.2.

The coupling plate which connected the antennas to the cold load was modified to permit faster and more reliable operation. A thin, concentric ring attached to the bottom of the plate acted as a guide like the one on the larger plate used to couple the 3-cm radiometer. This coupling arrangement proved to be much more satisfactory than the one used the previous year: The small coupling plate used with the 3.3-mm radiometer could be raised and lowered more quickly and with more accurate alignment than could the large, heavy plate designed for the 3-cm radiometer.

The gain of the lockin amplifier was reduced by 10% in order to compensate for the gain increase that occurred when the mixer was repaired. The amount of gain reduction was chosen so that the output voltage would be slightly less than 10 volts when the two antennas viewed ambient-temperature and LHe-temperature targets. This setting provided a nearly optimal match between the range of output voltages during a measurement cycle and the operating range of the ADC.

The zenith-angle measurement problems of the previous year prompted us to purchase a Tamaya precision clinometer with which we could measure the inclination of surfaces to an accuracy of one arcminute over a range of 90°. This proved to be extremely useful in helping us to determine the zenith angles viewed by the antennas in the various settings.

The changes in the radiometer and reflectors called for corresponding changes in the operation of the radiometer during measurements of both the zenith temperature and the atmospheric antenna temperature. To this end we adopted a nine-step cycle for measurements made over the cold load, including measurements of atmospheric emission at three pairs of nominal zenith angles. The first four steps measured T_{Zenith} and the radiometer calibration coefficient G. In the first step, one antenna looked into the cold load while the other viewed the zenith by means of a reflector. The second step was a calibration measurement in which the ambient calibrator was placed over the antenna that had previously viewed the zenith. For the third and fourth steps, the radiometer was rotated by 60° to reverse the roles of the two antennas, and the first and second steps were repeated.

The atmospheric antenna temperature, $T_{A,atm}$, was obtained from the five remaining steps. The radiometer was rotated to point the antennas upward and stepped through a series of angles, so that the north antenna viewed the sky at nominal zenith angles of 50°, 40°, 30°, 20°, and 10° to the north of the zenith while its southern partner observed the complementary zenith angles 10°, 20°, 30°, 40°, and 50°. (The 30°/30°, 40°/20°, and 50°/10° zenith-angle pairings were dictated by the 60° opening angle between the two antennas.) The observations at 40°/20°

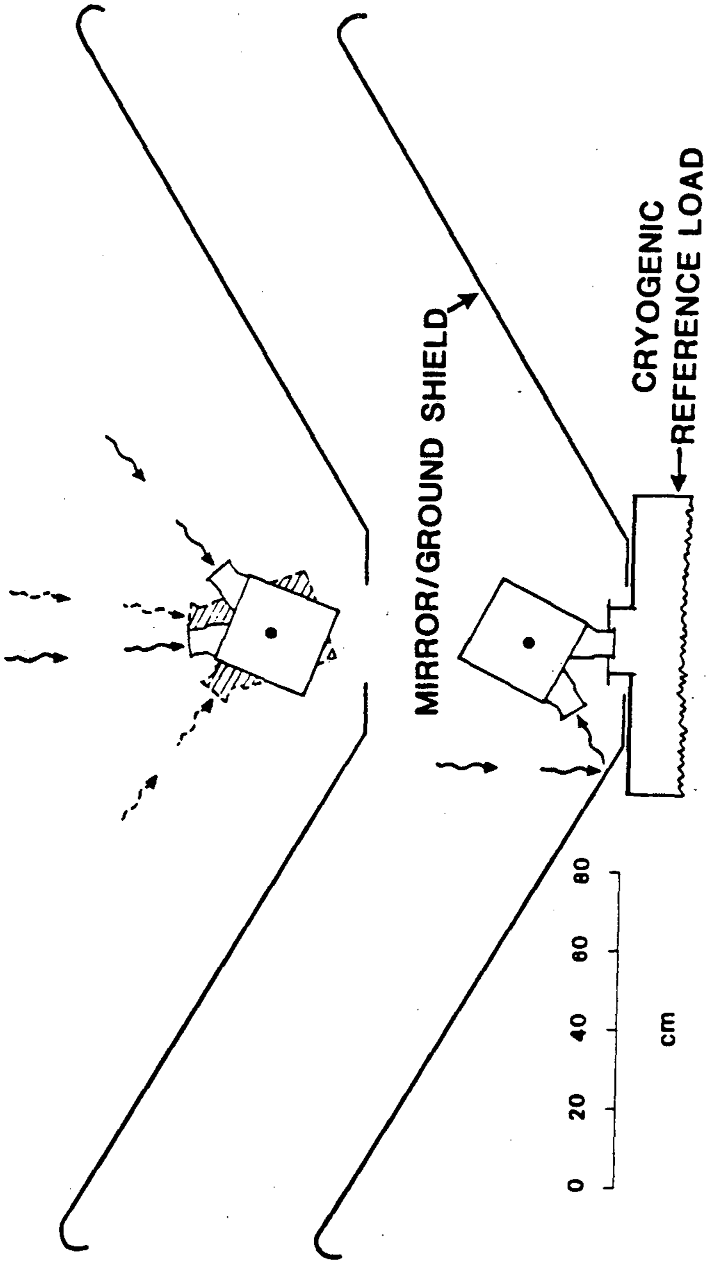

Figure 5.2: Schematic diagram of the radiometer and reflectors in their 1983 configuration.

and 50°/10° north and south were used to calculate $T_{A,atm}$; the 30°/30° measurements provided a means of monitoring the radiometer offset.

Because the radiometer could be moved quickly from one position to another, little time was wasted resetting the position during zenith scans. The time alloted to each step in the cycle was therefore reduced from 32 seconds to 16 seconds except for those steps in which extra time was needed to couple or decouple from the cold load. Shorter observation periods gave us time to make measurements at more zenith angles and reduced our sensitivity to fluctuations in the water-vapor column density. A measurement cycle, consisting of observations of the zenith and cold load, a gain calibration, and a set of atmospheric measurements, lasted 192 seconds.

A fourth radiometer, added to the Berkeley arsenal in 1983, functioned as a spectrometer which could be electronically tuned over the wavelength range from 1.7 to 15 cm. A DEC LSI-11/02 computer controlled its operation and recorded the observations for subsequent analysis. The computer was used to analyze and print out the results from the other Berkeley radiometers as well, and in this capacity it served as a backup for the cassette-tape recording system, thus eliminating the need to record radiometer output by hand.

Chapter 6

System Operation, 1983

6.1 Radiometer Characteristics

Tests to evaluate and characterise the radiometer were repeated on the modified system since many changes had been made and several components repaired. Several new tests were also performed in order to better measure any flip offsets that might be present and to measure the angular separation between the beam centers of the two antennas, a value needed for the analysis of atmospheric observations.

6.1.1 System Performance

The measured noise temperature of the system was 1520 ± 30 Kelvins (essentially unchanged from the previous year). The one-sigma noise fluctuations measured at White Mountain were 88 ± 2 mK for a 2-second integration period. The system offset looking into a zero-temperature load was -5.20 ± 0.11 Kelvins.

The calibration coefficient measured in the laboratory was 0.136 ± 0.003 K/microvolt at the detector diode output; the lockin output calibration was 32.3 ± 0.3 K/volt, or 9.86 ± 0.07 mK per digitized unit.

6.1.2 System Tests

We performed new tests to look for flip offsets in the radiometer. These were needed because the radiometer orientation now changed not only during measurements of the zenith temperature, but during atmospheric measurements as well, so an understanding of the offset variations was essential to the success of the measurement.

In order to measure the atmospheric flip offset directly, we constructed a pair of small LN-cooled loads which could be mounted over the two antennas. These were designed to be stable, low-temperature, low-reflectivity terminations whose radiometric properties would not change when they were tipped by up to 50° during measurements of the atmospheric flip offset.

Each load consisted of a styrofoam box filled with LN and lined on the bottom with two layers of Emmerson and Cummins AN-72 Eccosorb. It was held in an aluminum case which gave it added strength and allowed it to be bolted onto the antenna mount. The load was shielded from its surroundings by two layers of metal: the aluminum case on the outside, and an inner aluminum shield which surrounded the Eccosorb target on the sides and top. The antenna viewed the cold target through the bottom of the box, a 2.3-cm sheet of styrofoam with parallel v-grooves milled into its faces to reduce the reflection at the air/styrofoam and LN/styrofoam interfaces. The Eccosorb target was oversize—10.2 cm in diameter, compared to the 5.5-cm diameter of the antenna aperture—to reduce radiation leakage from beyond the target edge. The dimensions of the LN reservoir were chosen to ensure that the whole target was immersed in cryogen at all tip angles.

The radiometric temperature of the loads was approximately 80 K. Measurements made with the cold loads indicated an offset change of 9.8 ± 7.2 mK for scans at zenith angles of 40° north/south, and a change of 7.4 ± 9.2 mK for 50° zenith scans. In both cases, the offset was larger when the antennas pointed northward. When the measurements are extrapolated to 0 K loads, the resulting flip offsets are 13.4 ± 9.9 mK at 40° and 10.0 ± 12.6 mK at 50°.

We also measured the flip offset that occurred during measurements of the zenith temperature. This task was made easier by the new radiometer configuration, in which both antennas pointed downward during measurements of the zenith temperature. A pair of AN-72 Eccosorb targets was dipped in LN and held over the mouths of the antennas by spring clips. The radiometer was set in one of its two downward-looking positions and chopped to the other position every six seconds. The output voltage was recorded just before the radiometer position was reset, in order to give the lock-in, with its 2-second integration period, time to settle. A test lasted 60 to 120 seconds, until the differential warming of the two targets caused the offset to start drifting rapidly. A polynomial least-square fitting routine removed the drift from the data and computed the average values at the two positions. Initial measurements, made before the 1983 field operation, indicated an offset change of 50 ± 61 mK.

After our return from the field, we remeasured the zenith flip offset with improved Eccosorb targets which could be used for tests lasting up to 360 seconds. The combined result of six such tests yielded a flip offset of 15 ± 12 mK for 80 K loads; the extrapolated flip offset for 0 K was 20 ± 17 mK.

Emission from the aluminum reflectors was expected to contribute between 200 and 400 mK to the observed zenith temperature. To determine the value more accurately, we measured the difference between the zenith temperature observed when the antenna pointed directly upward and the temperature measured when the antenna viewed the zenith in the reflector. The measurements were performed in Berkeley, both before we went to White Mountain and after our return.

The most direct approach to the measurement was to cover one antenna with an ambient-temperature Eccosorb target and aim the other one alternately at the zenith and the reflector, then to calculate the reflector emission from the difference in the output values in the two states. Unfortunately, the gain of the radiometer varied by a factor of order 10^{-3} as the radiometer was rotated. This gain modulation caused the radiometer output to vary by approximately 200 mK, a term comparable to the expected emission from the reflector. We therefore made additional measurements in which we reduced the temperature variation by cooling the Eccosorb target with LN to reduce the sky/target temperature difference which the gain modulation acted upon.

Reflector measurements made with ambient and cold reference targets were extrapolated to the value that would have resulted if the reference target were at the same radiometric temperature as the sky, in order to remove the effect of gain modulation. This technique yielded temperatures of 263 ± 21 mK for the north reflector, and 341 ± 22 mK for the south reflector, viewing a 27 K sky at an ambient temperature of 278 K.

We also used a small reflector to make an independent measurement of the reflector emission. The reflector, made of alloy 1100 aluminum, was mounted next to one of the antennas with its normal vector 60° to the zenith. One of the radiometer antennas was pointed at the zenith, and the other was directed toward the reflector, through which it viewed the zenith as well. The output was recorded, then the reflector was placed next to the other antenna and the radiometer was rotated to interchange the roles of the two antennas. The difference in the output voltages in these two configurations was proportional to twice the reflector temperature. The temperature obtained was 168 ± 9 mK. When this was corrected for the variation of emissivity with the angle of reflection (a factor of cos 30°/cos 60°) and for the differences in the ambient and zenith temperatures between this measurement and those described above (a factor of 0.98) the result is 285 ± 16 mK.

The three measurements yield a mean value of 296 mK with an rms spread of 40 mK. This spread may represent a variation in the properties of the three aluminum sheets, so it is taken as the uncertainty in the emission from the reflectors.

The radiometer's magnetic sensitivity was evaluated as before. The radiometer was oriented with both antennas pointed 30° from the zenith, viewing LN-cooled loads. The offset change induced by a 5-Gauss vertical magnetic field was 17 ± 8 mK; a horizontal (north/south) 5-Gauss field caused a change of 7 ± 8 mK. The vertical and horizontal fields caused the gain to vary by factors smaller than 4×10^{-5} and 2×10^{-5} respectively.

Tests of the ground-shield performance showed that radiation from the ground contributed 12 ± 15 mK to the measured values of the T_{zenith}. They also set a 27-mK upper limit on amount of radiation from the ground and other objects on the horizon which could diffract past the edge of the ground shield into the antenna during measurements of the atmospheric temperature at a 50° zenith angle.

The angular separation between the beam centers of the two antennas was measured radiometrically. The results of this test, which is described in Appendix C, indicate that the radiometrically derived beam separation is in agreement with the value obtained if one measures the orientations of the antenna faces and simply assumes that the beam centers are perpendicular to them. The uncertainty in this measurement is ±4 arcminutes.

6.2 At White Mountain, 1983

Several considerations prompted us to plan our 1983 observations for late summer, rather than June or early July. The near-record snowfall that winter discouraged our hope that the road to Barcroft Station would be clear before the end of June. The unsettled weather we had experienced the year before, with intermittent rain and snow and relatively large amounts of water vapor in the air, also argued against observations in early summer, especially when there was so much water still on the ground. Microwave emission from the galactic plane interferred with observations at the longer wavelengths from early July until late August, so midsummer was ruled out as well. The position of the moon made some observing periods more desirable than others. New moon, the optimal date, occured on 7 September. Accordingly, we decided to meet at Barcroft in late August and to make our observations during the first week of September.

6.2.1 Reconnaissance

On 9 July 1983, Alan Benner and I made a preliminary trip to Barcroft Station, to see if the winter weather had affected the cold load and tracks and to start preparing the equipment and the site. Upon arrival, we learned that several weeks previously, the hole containing the cold load rested had filled with groundwater from the melting snow. Before the water was pumped out, the cold load, buoyed up by the water, had risen nearly a foot out of the hole, lifting not only its own weight but also 10 feet of steel tracks in either direction and the 12 × 12 wooden beams chained to the tracks. Needless to say, we were apprehensive about the equipment.

However, we need not have worried; the cold load had not suffered any serious damage. Aside from some water in the vacuum-valve bellows and mud in various unlikely spots, it seemed none the worse for its ordeal. The water was removed from the valve bellows, the cold load was re-aligned in its mounting (it had slipped out of position during its travels), and the nitrogen gas was pumped out of the cryostat vacuum region. Much to our relief, the cryostat held vacuum and showed no signs of either vacuum leaks or pooled water in the vacuum space.

Alan and I also checked the inside of the cold load to verify that the target and false wall were undamaged, and we repaired some damage which the shutter surface had suffered the previous year.

6.2.2 Return *En Masse*

In August the stream of researchers converged once more on Barcroft Station, the first trickle arriving on 20 August and the of the deluge flooding in over the course of the week. The radiometers and other equipment were unpacked, tested, and set in place. The cold-load shutter and windows were installed, and the load itself was warmed and dried with infrared lamps. When the cold load had been assembled, dried, and sealed to our satisfaction we filled it with LN on 27 August.

During the period from 27 August to 7 September (UT) we measured the radiometric temperature of the atmosphere on all nights when weather permitted in order to accumulate data on the range of values to be expected at that site. We performed many of the atmospheric measurements simultaneously at three or more wavelengths in order to study the wavelength dependence of $T_{A,atm}$ under a variety of atmospheric conditions. We also ran a number of integration tests with the two antennas pointed at different parts of the sky to evaluate the amplitude and time-structure of fluctuations in atmospheric emissivity.

Our first 3.3-mm measurements of T_{CBR} were made on 30 August (UT) during a 29-minute observing run, with LN in the cold load. Rainstorms delayed our progress, but by 2 September (UT) the sky was clear again. That night we measured T_{CBR} for 29 minutes with the LN-cooled load. High atmospheric humidity (measured relative humidity 85%) caused frost to form on the cold-load upper window, making the data from that night suspect.

On 3 September, the cold load was prepared for the LHe transfer. Our preparations went awry as we were pumping the LN out of the load. The load happened to be unattended when the last of the LN was removed; when the pump started pulling gas rather than cryogen out of the cryostat, the back-pressure in the transfer line dropped and the fluid throughput increased. Gas was removed from the cryostat faster than it was replaced, so the pressure in the cryostat fell below the outside pressure and air was sucked in through the vent lines. Moisture in the air condensed on the cold interior surfaces, forming a layer of frost on the false wall. The frost layer, unacceptable as it was, was not our only problem. The pressure difference created by the pump ruptured the lower cold load window, further adding to our troubles.

We warmed up the cold load that night and the next morning to drive off the moisture, and replaced the windows. By the afternoon of 4 September (UT), the inside of the cold load was dry and the windows were once again intact. The weather was still good and the humidity was very low, so we refilled the load with LN to cool it, then removed the LN (*very* carefully) and replaced it that evening with LHe.

We measured T_{CBR} at 3.3 mm on the nights of 4, 5, and 6 September (UT) with LHe in the cold load. Two observing runs, lasting 43 and 40 minutes, took place on the first night.

On the second night (5 September) chaos erupted. In the midst of the observing runs, a voltage-regulator failure on the electrical generator at Barcroft Station caused the line voltage to rise from 120 volts to approximately 180 volts. Much of the equipment was temporarily disrupted, but the main casualty was the computer that ran the tunable radiometer and provided on-line data printout and analysis for the other Berkeley radiometers. With the demise of the computer, we once again relied on hand-written voltage values to back up the data recorded on cassette tape. (Fortunately the tape writer and the radiometers were powered by batteries which isolated them from the worst effects of the power surge.) The equipment was connected to backup generators and the measurements were continued. One set of measurements, lasting 40 minutes, was performed with the 3.3-mm radiometer.

By the third night (6 September) the generator was functioning once again, although the computer was still dead. One 38-minute observing run was made with the 3.3-mm radiometer. The night's observations came to a premature end when we used up the last of the LHe.

The next day (7 September) the computer was finally resurrected. LN was transferred into the cold load and measurements of T_{CBR} were repeated that night. One observing run lasting 43 minutes was made with the 3.3-mm radiometer. Some frost was observed on the cold-load window at the end of the run.

On 8 September the cold load was drained of LN and warmed up. During the next two days the radiometers and other equipment were packed away. The cold load was covered and sealed against the elements, and its vacuum region was backfilled with nitrogen. On 10 September we left for Berkeley.

Chapter 7

Data Reduction and Processing

7.1 Selection and Editing of Data

A small amount of initial, quick-look analysis was performed in the field, but the bulk of the data reduction, processing, and analysis occurs in Berkeley. The first step in data reduction is to transfer the data from the cassette tapes to a disk for reduction and processing on the LSI-11/23 computer.

Following the data transfer, we inspect the data records in order to screen out erroneous values. Each record written during a CBR measurement is displayed on a terminal so that we may identify and delete those data values that are clearly in error. Blatently erroneous data occur in a few records as a result of the cold-load shutter being closed during a measurement of the zenith temperature or the antennas viewing the wrong angles during a zenith scan; such values are easily identified and removed.

In general, no attempt is made to analyse a measurement cycle in which the data from one or more of the steps is missing. Erroneous records resulted in the loss of 5 out of 37 CBR measurements in 1982 and 2 out of 51 measurements in 1983.

Data values recorded while the radiometer was in transit from one setting to another are somewhat more difficult to identify. The technique used in this case is to examine the first few values at each position for rapid drifts or sudden changes. The first value recorded at each position, and sometimes the second, are generally discrepant; if so they are discarded. The remaining values are then averaged.

The procedure is repeated for all the steps in the cycle. The mean and variance of the output values at each of the nine positions are recorded, together with the temperature of the ambient calibrator during the calibration steps. The editing process is repeated for each of the cycles in the measurement run, and the 70 to 120 reduced values are stored in a disk file. A similar procedure is used to reduce the data from atmospheric measurements. These data files serve as input for a computer program which computes $T_{A,atm}$ and $T_{A,CBR}$ as described below.

7.2 Determining the Calibration Coefficient

Once the raw data have been reduced, the first step in computing the CBR temperature is to determine the calibration coefficient G. All measurement cycles are individually calibrated in order to reduce the effect of gain drifts. The changes in the radiometer and calibration procedures from 1982 to 1983 have caused minor differences in the equations used to compute G.

1982: The equation used to determine the calibrations of the 1982 measurements is

$$G = 2\,\frac{(T_{A,Amb} - T_{A,Load} - T_{Refl})}{(V_{Amb/Zenith} + V_{Zenith/Load}) - (V_{Zenith/Amb} + V_{Load/Zenith})} \tag{7.1a}$$

where $T_{A,Amb}$ and $T_{A,Load}$ are the antenna temperatures of the ambient calibrator and cold load, T_{Refl} is the antenna temperature of the reflector (due to its nonzero emissivity), and $V_{Amb/Zenith}$, $V_{Zenith/Load}$, $V_{Zenith/Amb}$, and $V_{Load/Zenith}$ are the radiometer output voltages when the two antennas view the ambient calibrator and the zenith, the zenith and the cold load, etc.

T_{Refl} enters into equation (7.1a) because in the 1982 configuration the radiometer views the reflector during measurements of $T_{A,Amb} - T_{Zenith}$ but not during measurements of $T_{A,Load} - T_{Zenith}$. The assumed value of T_{Refl} is 400 mK, corresponding to an emissivity of 1.45×10^{-3}; the precise value is not crucial to the calculation.

1983: The altered calibration procedure used in 1983 leads to a simpler equation for G:

$$G = 2\,\frac{T_{A,Amb} - T_{A,Load}}{V_{Amb/Load} - V_{Load/Amb}}. \tag{7.1b}$$

Values of G from both years lie in the range from 8.8 to 10.5 mK /data unit.

$T_{A,Amb}$ and $T_{A,Load}$ are calculated with the aid of equation (2.3). $T_{A,Amb}$ is simply the temperature measured by the sensor on the ambient calibrator, converted to antenna temperature. $T_{A,Load}$ is the sum of the antenna temperature of the target, whose thermodynamic temperature is that of the boiling cryogen in which it is immersed, plus small temperature contributions from the windows and walls, plus the power broadcast by the antenna into the cold load and reflected back into the antenna by the cold-load windows. The smaller components of $T_{A,Load}$ are unimportant for calculations of G, but their contributions need to be known for accurate determinations of T_{Zenith} and $T_{A,CBR}$. Detailed discussion of the various uncertainties that enter into the calculation of T_{CBR} is deferred to Chapter 8, which deals with error analysis. Tables 8.2 and 8.3 in Chapter 8 list our best estimates of their values and uncertainties.

7.3 Determining the Zenith Temperature

Once the radiometer has been calibrated, the zenith temperature can be computed. We do so by adding the temperature of the cold load to the cold-load/zenith temperature difference measured by the radiometer. The cold-load temperature, as mentioned in the previous section, is the sum of several components:

$$T_{A,Load} = T_{A,LHe} + T_{Windows} + T_{Wall} \tag{7.2}$$

where $T_{A,LHe}$ is the boiling temperature of LHe, converted to antenna temperature, $T_{Windows}$ is the temperature component due to emission from the windows and radiation reflected by the windows into the radiometer, and T_{Wall} is the microwave power received by the radiometer from the cold-load walls.

1982: The radiometer configuration used in 1982 allows one antenna to point directly at the zenith while the other looks down into the cold load. The equation used to calculate T_{Zenith} is

$$T_{Zenith} = \frac{G}{2}(V_{Zenith/Load} - V_{Load/Zenith}) - \frac{\Delta T_{Z,Flip}}{2} + T_{A,Load} - T_{Z,gnd}\,, \tag{7.3a}$$

where $\Delta T_{Z,Flip}$ is the zenith flip offset, estimated to be 0 K but with an uncertainty discussed in Chapter 8. $T_{Z,gnd}$ is the ground radiation entering the upward-pointing antenna.

1983: In the new configuration, the antennas must view the zenith through reflectors during measurements of T_{Zenith}. Therefore, the radiation emitted by the reflectors must be considered when T_{Zenith} is evaluated. Because reflector emission adds to the zenith temperature, its estimated value must be subtracted from the temperature difference measured by the radiometer. Thus, the revised equation for T_{Zenith} is

$$T_{Zenith} = \frac{G}{2}(V_{Zenith/Load} - V_{Load/Zenith}) - \frac{\Delta T_{Z,Flip}}{2} + T_{A,Load} - T_{Refl} - T_{Z,gnd}\,, \qquad (7.3b)$$

where T_{Refl} is now the antenna temperature of the reflector which the antenna uses to view the zenith and $\Delta T_{Z,Flip}$ is the 20 ± 17 mK zenith flip offset discussed in § 6.1.2.

7.4 Determining the Atmospheric Contribution $T_{A,atm}$

$T_{A,atm}$ is the net contribution by the atmosphere to the zenith temperature. The atmosphere acts primarily as an emitter with a characteristic physical temperature of roughly 240 to 270 K and an opacity τ_0 in the zenith direction. At 3.3 mm, τ_0 is large enough so that atmospheric self-absorption cannot be neglected, even at a dry, high-altitude site. Besides emitting radiation, the atmosphere also attenuates incoming radiation, including the CBR, by a factor of $\exp(-\tau_0)$ in the zenith direction. The ratio of these two effects is approximately equal to the ratio of the atmosphere's characteristic temperature to the CBR antenna temperature, or about 250:1 at 3.3 mm.

The radiometric sky temperature $T_{Sky}(Z)$ is determined by the temperature and emissivity profiles of the atmosphere and the gain pattern of the antenna. Its zenith-angle dependence departs from a simple secant law not only because of the finite beamwidth of the antenna but also because of the earth's curvature and because of variation of atmospheric temperature with altitude. These latter two effects are small but are included for completeness.

$T_{A,atm}$ is obtained from measurements of the change in $T_{Sky}(Z)$ with zenith angle. This procedure assumes that the atmosphere is horizontally uniform—i.e. it neglects the effects of clouds and similar meteorological phenomena. Let $\Delta T_{Sky}(Z_1, Z_2)$ be the difference in $T_{Sky}(Z)$ measured at zenith angles Z_1 and Z_2, Define $\epsilon(Z_1, Z_2)$ as

$$\epsilon(Z_1, Z_2) \equiv \frac{\Delta T_{Sky}(Z_1, Z_2)}{\Delta \mathcal{T}_1(Z_1, Z_2)}\,,$$

where $\Delta \mathcal{T}_1(Z_1, Z_2)$, derived in Appendix A, characterizes the physical temperature of the atmosphere and the variation of air mass with zenith angle. The function $\epsilon(Z_1, Z_2)$ is equal to τ_0 to first order, and only weakly dependent on Z. Appendix A derives the relationship between $T_{A,atm}$ and $\epsilon(Z_1, Z_2)$:

$$T_{A,atm} \simeq \epsilon\, \hat{\mathcal{T}}_{atmos,1}(Z_1, Z_2) + \epsilon^2\, \hat{\mathcal{T}}_{atmos,2}(Z_1, Z_2) + \epsilon^3\, \hat{\mathcal{T}}_{atmos,3}(Z_1, Z_2)\,, \qquad (7.4)$$

where the functions $\hat{\mathcal{T}}_{atmos,n}(Z_1, Z_2)$ are derived in the appendix and where the Z-dependence of ϵ has been suppressed for typographical clarity.

To derive $T_{A,atm}$, we still need to know the values of $\hat{\mathcal{T}}_{atmos,n}(Z_1, Z_2)$ and $\Delta \mathcal{T}_1(Z_1, Z_2)$, which depend upon the temperature and emissivity profiles of the atmosphere and the gain pattern of the antenna. Fortunately, the value of $T_{A,atm}$ obtained from atmospheric scans is not strongly dependent on our knowledge of atmospheric conditions. Information about the temperature and emissivity profiles only enters into the corrections for atmospheric self-absorption, a 4% to 5% effect at the high-altitude site, so precise temperature and emissivity profiles are not necessary. We therefore take the temperature and emissivity profiles from standard atmospheric models (Ulaby, Moore, and Fung 1981). The error that results from this simplification is discussed in Chapter 8.

The actual derivation of $T_{A,atm}$ is slightly more complicated than the situation just described because each value of $T_{A,atm}$ is derived from two measurements of ΔT_{Sky} at four zenith angles. For the first measurement, one antenna points southward at a zenith angle Z_1 of either approximately 40° or approximately 50°, while the other antenna observes at a zenith angle Z_2, a point closer to the zenith than Z_1. (The value of Z_2 used for the 1982 measurements is approximately 0°, while the value used in 1983 is either approximately 20° north or 10° north, depending on the value of Z_1.) The output voltage from the radiometer is proportional to the difference in the sky temperatures seen by the first and second antennas (a positive quantity) plus the radiometer's offset temperature.

The second measurement is similar to the first, but the first antenna points toward a zenith angle Z_3 near or slightly *south* of the zenith whose value is approximately equal to Z_2, at approximately the same zenith angle viewed by the second antenna in the previous measurement, while the second antenna observes at a zenith angle Z_4 approximately equal to Z_1 but *north* of the zenith. The sky-temperature difference seen by the radiometer during this measurement is negative because Z_3 is less than Z_4; the offset temperature has the same sign and the same or nearly the same value that it had in the first measurement.

The radiometer output voltages from the two measurements are then differenced, a procedure which removes the radiometer offset and also cancels the first-order effects of a tilted cart. The 1983 data are also corrected at this point for the flip offsets that occurred during the atmospheric measurements. The voltage value is converted to a temperature difference according to the formula:

$$\Delta T_{Sky}(\theta_1,\theta_2) = \frac{1}{2}\left[G\left(V_{\theta_1/\theta_2} - V_{\theta_2/\theta_1}\right) - \Delta T_{Flip}(\theta_1,\theta_2)\right] - T_{atm,gnd}(\theta_1,\theta_2), \tag{7.5}$$

where θ_1 and θ_2 are the nominal zenith angles viewed by the antennas during the atmospheric measurement (e.g. $\theta_1 = 50°$, $\theta_2 = 10°$; $\theta_1 \simeq Z_1 \simeq Z_4$, $\theta_2 \simeq Z_2 \simeq Z_3$). $T_{atm,gnd}(\theta_1,\theta_2)$ is the contribution from ground radiation, and $\Delta T_{Flip}(\theta_1,\theta_2)$ is the flip-offset correction for the atmospheric scan. There is no flip-offset correction for the 1982 atmospheric measurements since the radiometer did not change positions; the values of $\Delta T_{Flip}(\theta_1,\theta_2)$ in 1983 are -13.4 ± 9.9 mK for 40°/20° scans and -10.0 ± 12.6 mK for 50°/10° scans.

The equation used to calculate $T_{A,atm}$ from $\Delta T_{Sky}(\theta_1,\theta_2)$ is exactly analogous to equation (7.4), except that values of $\Delta\mathcal{T}_1$ and $\hat{T}_{atmos,n}$ used in the equation are now computed from four zenith angles. Thus,

$$\epsilon(\theta_1,\theta_2) \equiv \frac{\Delta T_{Sky}(\theta_1,\theta_2)}{\Delta\mathcal{T}_1(\theta_1,\theta_2)} \tag{7.6}$$

and

$$T_{A,atm} \simeq \epsilon\hat{T}_{atmos,1}(\theta_1,\theta_2) + \epsilon^2\hat{T}_{atmos,2}(\theta_1,\theta_2) + \epsilon^3\hat{T}_{atmos,3}(\theta_1,\theta_2)\ , \tag{7.7}$$

where the nominal zenith angles are used here for compactness and where $\hat{T}_{atmos,n}(\theta_1,\theta_2)$ and $\Delta\mathcal{T}_1(\theta_1,\theta_2)$ represent the averages of the values at zenith angles Z_1 and Z_2 and at zenith angles Z_4 and Z_3. Table 7.1 lists the zenith angles at which observations were made in 1982, together with our best estimates of $\hat{T}_{atmos,n}(\theta_1,\theta_2)$, and $\Delta\mathcal{T}_1(\theta_1,\theta_2)$. Because of the uncertainty and variation in the 1982 zenith angles, Table 7.1 contains both the zenith-angle measurements of 3 July 1982 and those of 9 July 1982. Table 7.2 contains the zenith-angle values measured on 8 September 1983 and the terms derived from them.

Atmospheric measurements from the two years are processed similarly; aside from the changes in the zenith angles, the only significant change from the first year to the second is the number of angles at which T_{Sky} was observed during each measurement cycle. The 1982 cycle includes one measurement of $T_{A,atm}$ at either 40°/0° or 50°/0°. The 1983 cycle has been augmented to include two separate measurements of $T_{A,atm}$, one at 40°/20° and another at 50°/10°; the mean of the two values is used to calculate $T_{A,CBR}$.

Nominal Angle	Actual Angle N Antenna	Actual Angle S Antenna	ΔT_1 (K)	$\hat{T}_{atmos,1}$ (K)	$\hat{T}_{atmos,2}$ (K)	$\hat{T}_{atmos,3}$ (K)
3 July 1982						
40° 0°	38°.7 1°.0	39°.2 1°.5	75.3	260.7	166	246
50° 0°	49°.0 1°.0	48°.7 1°.5	137.6	260.7	197	324
9 July 1982						
40° 0°	38°.5 0°	40°.3 0°	77.9	260.7	167	249
50° 0°	49°.4 0°	51°.0 0°	149.3	260.7	204	340

Table 7.1: Temperatures and angles used to compute $T_{A,atm}$ in 1982. The temperatures are intermediate between the values computed for pure oxygen emission (emissivity scale height $\simeq$ 4.2 km) and pure water-vapor emission (e.s.h. $\simeq$ 1.7 km). Values derived from the zenith-angle measurements of 3 July 1982 and those of 9 July 1982 are both listed.

Nominal Angle	Actual Angle N Antenna	Actual Angle S Antenna	ΔT_1 (K)	$\hat{T}_{atmos,1}$ (K)	$\hat{T}_{atmos,2}$ (K)	$\hat{T}_{atmos,3}$ (K)
40° 20°	40°.42 20°.33	39°.23 19°.15	63.4	260.7	176	274
50° 10°	50°.40 10°.33	49°.23 9°.17	142.0	260.7	205	344

Table 7.2: Temperatures and angles used to compute $T_{A,atm}$ in 1983. The temperatures are intermediate between the values computed for pure oxygen emission (emissivity scale height $\simeq$ 4.2 km) and pure water-vapor emission (e.s.h. $\simeq$ 1.7 km).

7.5 Determining $T_{A,CBR}$

Once T_{Zenith} and $T_{A,atm}$ have been determined, we calculate $T_{A,CBR}$ simply by taking the difference of the two terms. (The contribution to T_{Zenith} from galactic sources is less than 1 mK (Epstein 1983) and can therefore be neglected.) At this point, all the values of $T_{A,CBR}$ which result from a measurement run are tabulated, as are the values of G, T_{Zenith}, and $T_{A,atm}$. The mean value and the rms variation are calculated for each of the tabulated terms. The tabulated values are inspected, and those observations which produced suspect data are noted. Tables 7.3 and 7.4 contain the tabulated results of the 1982 and 1983 measurements made with LHe in the cold load.

The mean values of $T_{A,CBR}$ from all the observing runs of the year are combined to form an overall mean, $\overline{T}_{A,CBR}$. The value of $\overline{T}_{A,CBR}$ derived from the 1983 data is the weighted average of the mean values from the individual observing runs, with each mean weighted by its variance.

The zenith-angle uncertainty and day-to-day drift in the 1982 results, all too evident in Table 7.3, prevent them from being treated so simply. The question of how to treat the 1982 results is discussed in the following chapter, which deals with error analysis.

Once the value of $\overline{T}_{A,CBR}$ is obtained, it is converted to a thermodynamic temperature. This step is described in Chapter 9.

RESULTS FROM 5 JULY 1982 (Run 1)

	TIME	θ	GAIN (mK/du)	T_{Zenith} (K)	$T_{A,atm,1}$ (K)	$T_{A,atm,2}$ (K)	$T_{A,CBR,1}$ (K)	$T_{A,CBR,2}$ (K)
1	8:58	40°	9.702	13.210	12.885	12.456	0.326	0.754
2	9:01	40°	9.696	13.205	12.563	12.145	0.642	1.059
3	9:16	40°	9.712	13.178	12.498	12.082	0.680	1.095
MEAN					12.648	12.228	0.549	0.970
RMS					0.207	0.200	0.195	0.188
1	8:46	50°	9.729	13.191	12.403	11.410	0.788	1.782
2	8:50	50°	9.716	13.224	12.056	11.091	1.168	2.133
3	8:54	50°	9.728	13.261	12.063	11.097	1.199	2.164
4	9:05	50°	9.714	13.200	12.295	11.310	0.904	1.889
5	9:09	50°	9.725	13.178	12.436	11.439	0.742	1.739
6	9:13	50°	9.720	13.207	12.163	11.189	1.044	2.018
MEAN					12.236	11.256	0.974	1.954
RMS					0.167	0.153	0.193	0.179
MEAN			9.716	13.206				
RMS			0.010	0.026				

RESULTS FROM 6 JULY 1982 (Run 2)

	TIME	θ	GAIN (mK/du)	T_{Zenith} (K)	$T_{A,atm,1}$ (K)	$T_{A,atm,2}$ (K)	$T_{A,CBR,1}$ (K)	$T_{A,CBR,2}$ (K)
1	2:11	40°	10.463	15.165	14.733	14.241	0.432	0.924
2	2:22	40°	10.415	14.763	14.153	13.681	0.610	1.082
3	2:40	40°	10.431	14.356	13.794	13.334	0.562	1.022
MEAN					14.227	13.752	0.535	1.009
RMS					0.474	0.458	0.092	0.080
1	2:02	50°	10.521	14.599	15.084	13.870	−.485	0.730
2	2:06	50°	10.541	14.658	14.040	12.911	0.618	1.746
3	2:14	50°	10.500	15.108	14.054	12.924	1.054	2.183
4	2:18	50°	10.476	14.786	13.560	12.471	1.227	2.315
5	2:25	50°	10.490	14.425	14.788	13.597	−.363	0.827
6	2:29	50°	10.473	14.250	13.626	12.532	0.624	1.719
7	2:32	50°	10.452	14.551	14.128	12.992	0.423	1.559
8	2:36	50°	10.477	14.393	13.809	12.700	0.584	1.693
9	2:44	50°	10.444	14.303	13.376	12.302	0.927	2.001
10	2:51	50°	10.463	14.085	14.037	12.909	0.047	1.175
11	2:55	50°	10.439	14.347	13.439	12.360	0.909	1.988
MEAN					13.995	12.870	0.506	1.631
RMS					0.538	0.493	0.561	0.523
MEAN			10.469	14.532				
RMS			0. 034	0.317				

Table 7.3: Results of the 1982 CBR Measurements

RESULTS FROM 6 JULY 1982 (Run 3)

	TIME	θ	GAIN (mK/du)	T_{Zenith} (K)	$T_{A,atm,1}$ (K)	$T_{A,atm,2}$ (K)	$T_{A,CBR,1}$ (K)	$T_{A,CBR,2}$ (K)
1	9:14	40°	9.773	13.668	13.600	13.147	0.068	0.521
2	9:25	40°	9.758	13.529	13.232	12.792	0.296	0.737
3	9:36	40°	9.777	13.403	12.858	12.430	0.545	0.973
MEAN					13.230	12.790	0.303	0.744
RMS					0.371	0.358	0.239	0.226
1	9:06	50°	9.759	13.765	13.286	12.220	0.478	1.545
2	9:10	50°	9.783	13.629	13.067	12.019	0.562	1.610
3	9:18	50°	9.760	13.970	13.431	12.353	0.538	1.617
4	9:21	50°	9.761	13.731	13.009	11.966	0.722	1.765
5	9:29	50°	9.770	13.395	12.825	11.797	0.570	1.598
6	9:33	50°	9.775	13.576	12.444	11.447	1.132	2.129
MEAN					13.010	11.967	0.667	1.711
RMS					0.350	0.321	0.242	0.218
MEAN			9.768	13.630				
RMS			0.007	0.182				

Table 7.3: Results of the 1982 CBR Measurements (cont.)

RESULTS FROM 4 SEPT 1983

	TIME	GAIN (mK/du)	T_{Zenith} (K)	$T_{A,atm,40/20}$ (K)	$T_{A,atm,50/10}$ (K)	$T_{A,CBR}$ (K)
1	6:33	8.763	10.724	9.912	9.597	0.969
2	6:36	8.760	10.636	9.657	9.600	1.008
3	6:39	8.775	10.500	9.559	9.442	0.999
4	6:42	8.761	10.505	9.681	9.614	0.857
5	6:46	8.768	10.597	9.638	9.702	0.928
6	6:49	8.782	10.599	9.634	9.457	1.054
7	6:58	8.767	10.537	9.675	9.701	0.849
8	7:02	8.771	10.513	9.457	9.423	1.073
9	7:05	8.778	10.523	9.644	9.631	0.886
10	7:08	8.778	10.595	9.544	9.491	1.077
11	7:11	8.775	10.442	9.325	9.390	1.084
MEAN		8.771	10.561	9.611	9.550	0.980
RMS		0.007	0.078	0.147	0.113	0.089

RESULTS FROM 4 SEPT 1983

	TIME	GAIN (mK/du)	T_{Zenith} (K)	$T_{A,atm,40/20}$ (K)	$T_{A,atm,50/10}$ (K)	$T_{A,CBR}$ (K)
1	11:58	8.745	10.203	9.166	9.182	1.029
2	12:01	8.749	10.203	8.954	9.036	1.208
3	12:04	8.751	10.084	9.128	9.204	0.918
4	12:08	8.757	10.178	9.249	9.287	0.910
5	12:11	8.755	10.129	8.997	9.101	1.080
6	12:14	8.759	10.121	9.123	9.154	0.982
7	12:17	8.753	10.090	9.153	9.126	0.950
8	12:20	8.755	10.027	9.174	9.192	0.844
9	12:24	8.754	10.084	9.137	9.054	0.989
10	12:27	8.754	10.187	9.030	9.168	1.088
11	12:30	8.745	10.273	9.447	9.221	0.939
12	12:33	8.750	10.345	9.446	9.331	0.957
MEAN		8.752	10.160	9.167	9.171	0.991
RMS		0.004	0.090	0.154	0.087	0.098

Table 7.4: Results of the 1983 CBR Measurements

RESULTS FROM 5 SEPT 1983

	TIME	GAIN (mK/du)	T_{Zenith} (K)	$T_{A,atm,40/20}$ (K)	$T_{A,atm,50/10}$ (K)	$T_{A,CBR}$ (K)
1	5:23	9.090	12.135	10.921	11.043	1.153
2	5:27	9.089	12.092	10.991	10.953	1.120
3	5:30	9.081	11.980	11.083	10.876	1.001
4	5:33	9.073	11.939	10.921	11.252	0.853
5	5:36	9.060	11.996	10.852	11.106	1.017
6	5:39	9.051	11.946	11.128	11.101	0.832
7	5:43	9.037	12.050	11.253	11.141	0.853
8	5:46	9.030	12.072	11.001	11.127	1.008
9	5:49	9.029	12.085	10.844	11.128	1.099
10	5:52	9.012	12.069	11.012	11.019	1.053
11	5:55	9.002	12.034	10.630	11.097	1.171
12	5:59	9.002	11.923	10.780	10.966	1.050
13	6:02	8.988	11.899	10.691	10.937	1.084
14	6:05	8.981	11.828	10.962	10.968	0.863
MEAN		9.037	12.004	10.934	11.051	1.011
RMS		0.037	0.088	0.168	0.102	0.117

RESULTS FROM 6 SEPT 1983

	TIME	GAIN (mK/du)	T_{Zenith} (K)	$T_{A,atm,40/20}$ (K)	$T_{A,atm,50/10}$ (K)	$T_{A,CBR}$ (K)
1	5:38	9.189	13.169	13.062	12.930	0.173
2	5:42	9.198	13.156	12.335	12.224	0.877
3	5:45	9.193	13.031	12.741	12.347	0.488
4	5:48	9.177	13.030	12.241	12.163	0.828
5	5:51	9.178	13.411	12.197	11.972	1.326
6	5:54	9.169	13.200	11.899	11.861	1.320
7	5:58	9.161	13.143	12.744	12.762	0.390
8	6:01	9.159	13.185	11.610	11.355	1.703
9	6:04	9.156	12.927	12.248	11.990	0.808
10	6:07	9.153	12.652	12.192	12.563	0.275
11	6:10	9.155	12.856	11.120	11.699	1.446
12	6:14	9.163	12.818	12.137	11.805	0.848
MEAN		9.171	13.048	12.210	12.139	0.873
RMS		0.016	0.207	0.519	0.456	0.492

Table 7.4: Results of the 1983 CBR Measurements (cont.)

Chapter 8

Data Analysis—Uncertainties and Systematic Errors

8.1 Introduction

Any measurement of the CBR temperature without a *realistic* estimate of its uncertainty is suspect at best and useless at worst. The uncertainty in the CBR measurement is largely determined by systematic errors, so these need to be recognized and carefully evaluated in the data analysis. Statistical uncertainties in the measurements also contribute to the overall uncertainty of the result; these errors must be accounted for as well.

8.2 Statistical Fluctuations

Fluctuations in the radiometer output are caused by noise-power variations from two sources: internally-generated radiometer noise, which fluctuates because of statistical variations in its strength, and atmospheric emission, which varies with the column density of water vapor observed by the antennas. Both types of fluctuations add random variations to the CBR measurements, but their properties differ markedly.

Figure 8.1 plots the spectrum of the radiometer-noise fluctuations and the atmospheric fluctuations measured at White Mountain on 6 September 1983. Both antennas viewed the zenith (a convenient cold target) during the radiometer-noise measurement; changes in atmospheric emission had little effect on the measurement since the fluctuations seen by both antennas were equal. Atmospheric fluctuations were measured with the antennas pointed 60° apart, so the relative changes in atmospheric emission at zenith angles of 40° south and 20° north combined with the radiometer-noise to produce the observed fluctuations. Each measurement lasted for 34.1 minutes (2048 seconds).

The spectrum of radiometer-noise fluctuations shown in Figure 8.1 is characteristic of white (frequency-independent) noise. The rms variation of the 2-second signal averages is 9.84 ± 0.22 d.u., or 87.7 ± 2.0 mK. When the output is averaged over intervals of n seconds, the rms fluctuations in the average values scale as $n^{-\frac{1}{2}}$ as predicted by equation (2.4).

Large-amplitude, low-frequency atmospheric fluctuation dominate the second spectrum in the figure. The amplitude of these atmospheric components drops below the level of the radiometer-noise fluctuations at periods shorter than about 120 seconds.

One can compare the uncertainties which the two noise mechanisms add to measurements of T_{CBR} by calculating the rms variation in a set of 12 consecutive 16-second averages of the measurement values. The variation in the averages calculated from the measurements of atmospheric fluctuations is 9.4 d.u. (84 mK), compared to the 2.7 d.u. (24 mK) variation in the averages of the radiometer noise measurements. Such calculations do not predict the amount of

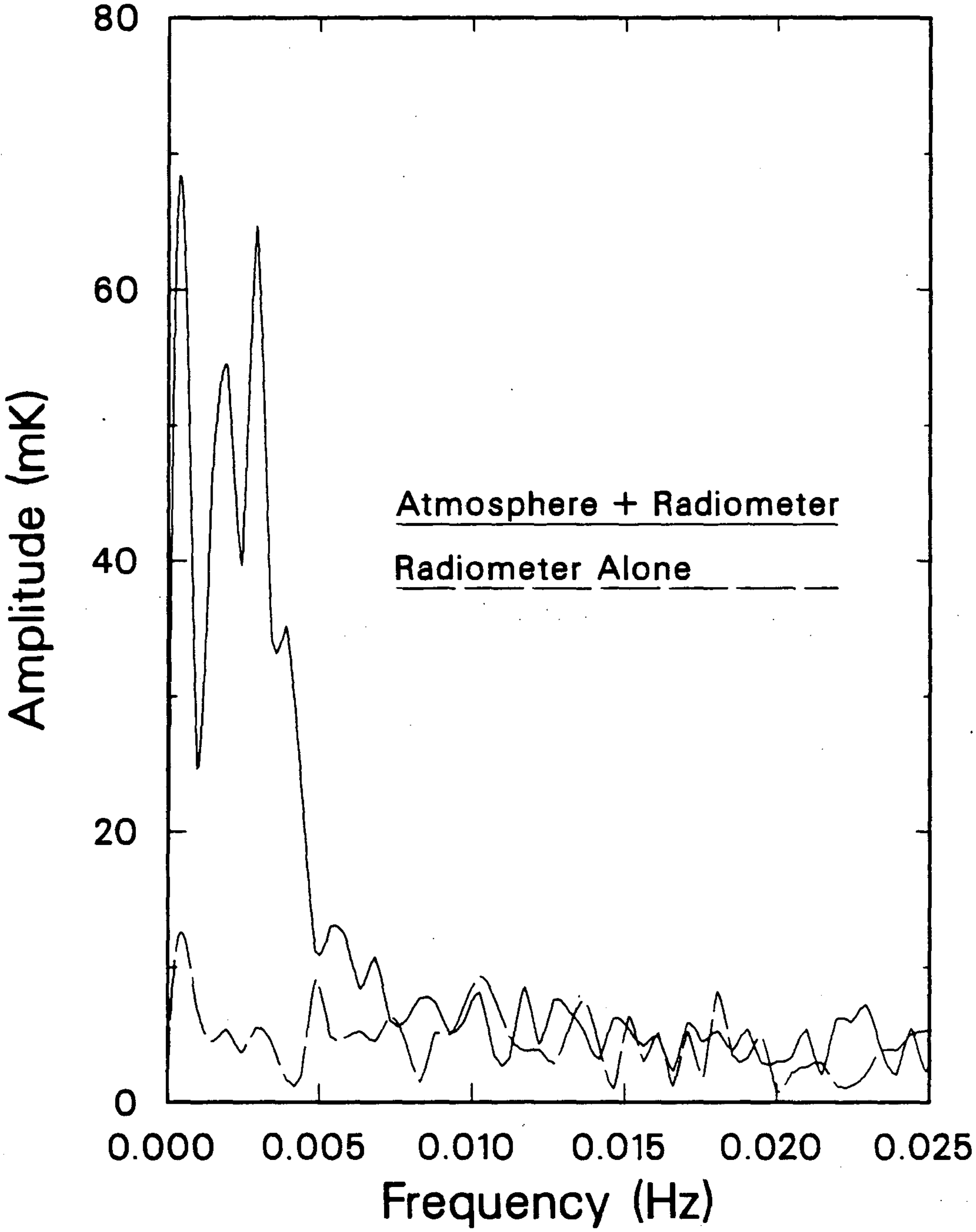

Figure 8.1: Noise from atmosphere and radiometer—frequency domain.

variation to be expected in CBR measurements, but they do provide a way to compare the relative effects of atmospheric fluctuations and radiometer noise over the course of one CBR measurement cycle. Clearly, atmospheric fluctuations are the dominant source of statistical uncertainty in the measurement.

The net effect of atmospheric fluctuations can be seen in the results in Tables 7.3 and 7.4. Figure 8.2, a histogram of the CBR antenna temperatures measured on 4 and 5 September 1983, shows the distribution of the values during a period when observing conditions were especially good. The scatter in the measured values of $T_{A,CBR}$ during the four observing runs ranges from 90 mK on 4 September to 500 mK on 6 September and correlates closely with the scatter in $T_{A,atm}$.

The scatter in $T_{A,atm}$ is larger than that in T_{Zenith} for two reasons: First, each measurement of $T_{A,atm}$ requires observations in two parts of the sky whose fluctuations are only loosely correlated, so the fluctuations add; second, the fluctuations are amplified in the calculation of $T_{A,atm}$ because the measured temperature differences (and their fluctuations) are multiplied by factors ranging from 1.8 to 4.1, depending on the zenith angles used. This second reason also explains why the scatter in the 1983 measurements of $T_{A,atm}$ is greater for measurements made at 40°/20° zenith angles than for those at 50°/10°.

The variance in the mean value of $T_{A,CBR}$ from each run is computed from the spread in the individual values of $T_{A,CBR}$. The variances in the 1983 results are used as weighting terms to calculate the overall average, $\overline{T}_{A,CBR}$, according to the formula

$$\overline{T}_{A,CBR} = \frac{\sum_{i=1}^{4} T_i/\sigma_i^2}{\sum_{i=1}^{4} 1/\sigma_i^2} \tag{8.1}$$

where T_i is the mean value of $T_{A,CBR}$ from the i'th measurement run, and σ_i^2 is the variance of the individual values which make up the mean. The statistical uncertainty in the overall mean is

$$\sigma_{\overline{T}_{A,CBR}} = \left(\sum_{i=1}^{4} 1/\sigma_i^2\right)^{-\frac{1}{2}} . \tag{8.2}$$

The CBR antenna temperature so derived from the 1983 measurements is

$$\overline{T}_{A,CBR} = 0.99 \pm 0.016 \text{ K} \qquad (1983) .$$

Note that only the *statistical* uncertainty is quoted here.

The statistical uncertainty in the 1982 measurements is

$$\sigma_{\overline{T}_{A,CBR}} = \pm 0.034 \text{ K} \qquad (1982) .$$

This value is computed as in equation (8.2), except that those $T_{A,CBR}$ measurements in each measurement run which included atmospheric measurements at 40° are treated separately from those with atmospheric measurements at 50°. A total of six variances is summed; each one is the average of the variance in $T_{A,CBR,1}$ and $T_{A,CBR,2}$. Because of the pointing uncertainties mentioned in the previous chapter, the computation of $\overline{T}_{A,CBR}$ from the 1982 measurements is deferred to § 8.3.3.

8.3 Systematic Uncertainties

The systematic uncertainties fall into three general categories: those which result from the design and operation of the radiometer, those due to the behavior of the LHe cold load, and

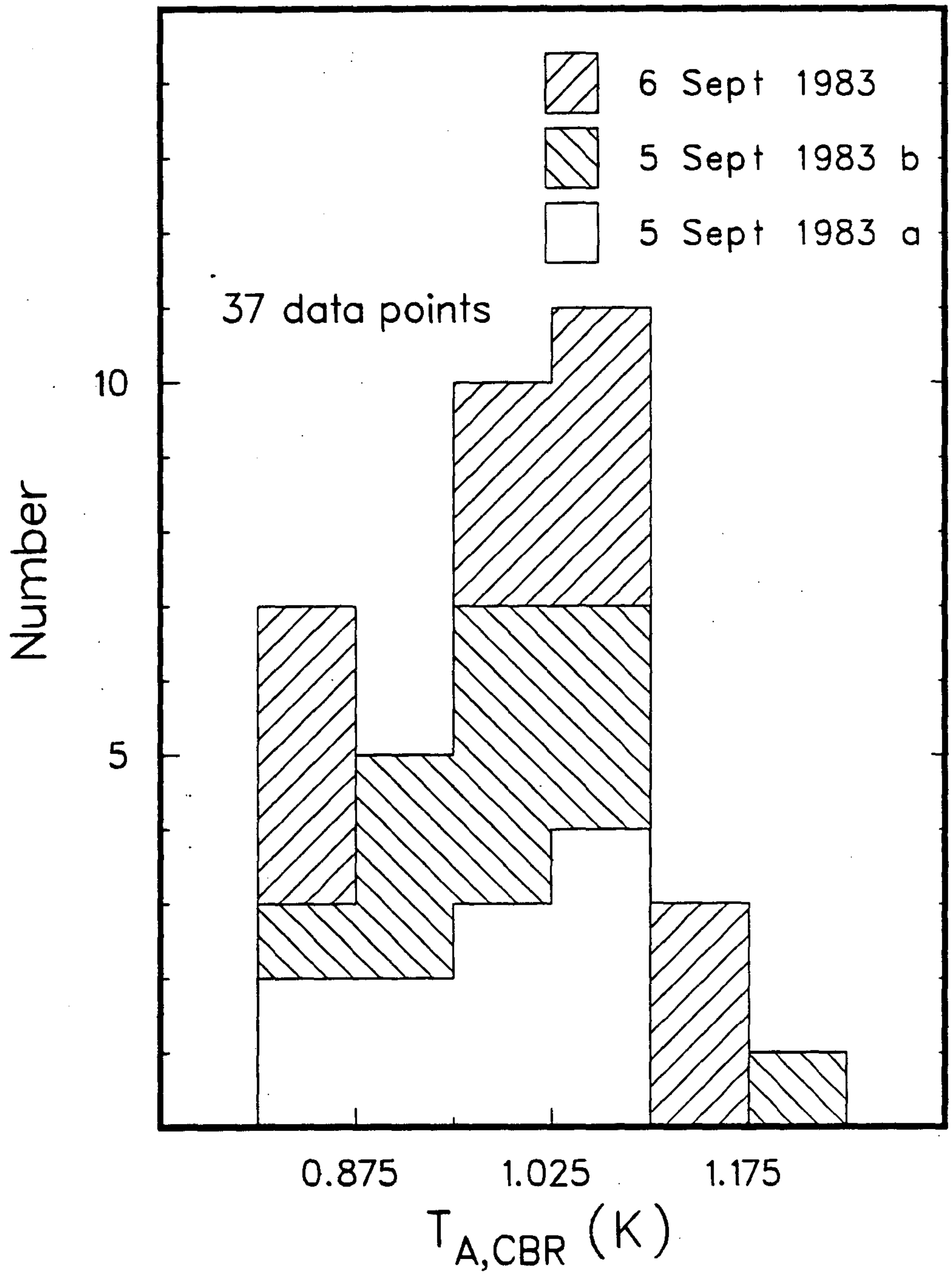

Figure 8.2: Histogram of CBR measurements at 3.3 mm on 4 and 5 September 1983.

those caused by uncertainty in the parameters used to calculate $T_{A,atm}$. The overall systematic uncertainty in the 1983 measurements is composed of roughly comparable contributions from each of the three categories. The first two categories of systematic errors in the 1982 measurements are generally comparable to their 1983 equivalents, but the uncertainty in the zenith angles used in the 1982 measurements causes an uncertainty in $T_{A,atm}$ that overwhelms all the other errors in the measurement.

8.3.1 Radiometer-Related Uncertainties

Uncertainties in the behavior of the radiometer can cause a number of significant systematic errors. The two largest sources of error are uncertainty in the magnitude of flip offsets and in the amount of emission from the reflectors. Two other error sources, uncertainty in the amount of ground radiation that enters the radiometer and uncertainty in the radiometer calibration, are smaller but must still be evaluated. All of these are discussed below.

8.3.1.1 Flip Offsets

1982: The possibility of flip offsets (discussed in Chapter 3) is a major consideration not only in the design of the instrument but also in the analysis of the results. The flip-offset tests performed in 1982 set a 30-mK upper limit on the offset change when the radiometer is pointed horizontally, but they do not indicate whether a flip offset is present in the measurements of T_{Zenith}.

To supplement the results of the tests, we have examined the 1982 CBR measurements for evidence of flip offsets by comparing the average offset in the two vertical positions used to measure T_{Zenith} with the offset present when the horizontally-pointing antennas view the zenith by means of the reflectors. The offset change revealed by this comparison is still not a direct measurement of the relevant flip offset, but it does provide another indication of the probable magnitude of the flip offset.

The equation used to compute the offset change is

$$\Delta T_{Offset} = G\ \left(V_{Zenith/Load} + V_{Load/Zenith}\right) \frac{(T_0 - T_{Zenith})}{(2\,T_0 - T_{Zenith} - T_{A,Load})} + G\,V_{0/0} \qquad (8.3)$$

where $V_{0/0}$ is the radiometer output voltage when both antennas view the zenith by means of the reflectors. The first term is the average offset in the two vertical positions, with a small correction added for the effect of the temperature difference between the load and the zenith; the second term is the offset in the horizontal position with the antennas viewing the zenith. Analysis of the 1982 data reveals that ΔT_{Offset} is 16 ± 16 mK. The 300 mK value of ΔT_{Offset} reported by DeAmici *et al.*(1984) is incorrect because the analysis does not correct for the zenith/cold-load temperature difference.

The tests and analysis do not rule out a large change in the instrumental offset during zenith measurements, but they do suggest that the offset change is probably on the order of 100 mK or less. If this value is adopted as a conservative estimate of the uncertainty in $\Delta T_{Z,Flip}$, then from equation (7.3a), the resulting uncertainty in T_{Zenith} is half of that, or 50 mK.

1983: Flip offsets cause uncertainty in both the zenith and atmospheric measurements from 1983. The 20 ± 17 mK zenith-temperature flip offset ($\Delta T_{Z,Flip}$ in equation (7.3b)) gives rise to a ±9 mK uncertainty in T_{Zenith}.

One can easily show from equations (7.5) and (7.7) that an uncertainty $\sigma_{\Delta T,Flip(\theta_1,\theta_2)}$

causes an uncertainty in $T_{A,atm}$ whose approximate value is given by the equation:

$$\sigma_{T_{A,atm}} \simeq \frac{\sigma_{\Delta T,Flip(\theta_1,\theta_2)} \hat{\mathcal{T}}_{atmos,1}(\theta_1,\theta_2)}{2\Delta \mathcal{T}_1(\theta_1,\theta_2)} \simeq \frac{\sigma_{\Delta T,Flip(\theta_1,\theta_2)}}{\sec(\theta_1)-\sec(\theta_2)} \tag{8.4}$$

where $\hat{\mathcal{T}}_{atmos,1}(\theta_1,\theta_2)$ and $\Delta\mathcal{T}_1(\theta_1,\theta_2)$ are atmospheric-model terms introduced in § 7.4 and derived in Appendix A. Using the values of the atmospheric terms in Table 7.2 one can show that the -13 ± 10 mK value of $\Delta T_{Flip}(40,20)$ causes an uncertainty of approximately ±21 mK in $T_{VA,40/20}$. The -10 ± 13 mK flip offset during 50°/10° atmospheric measurements leads to a ±12 mK uncertainty in $T_{VA,50/10}$. The error in equation (8.4) which results from neglecting the higher-order terms in equation (7.7) is less than 3 mK at a 40° zenith angle and less than 1 mK at a 50° zenith angle.

8.3.1.2 Reflector Emission

Uncertainty in the microwave emissivity of the reflectors contributes to the overall uncertainty in both the 1982 and 1983 CBR measurements, but in different ways and for different reasons.

1982: In the 1982 configuration, the radiometer views the reflectors during all atmospheric measurements and at no other time, so the reflectors radiate approximately the same amount of microwave power into both antennas and the contributions from the two reflectors differ by less than 10 mK. If the reflectors were known to have uniform emissivities over their entire surfaces, the ±40 mK uncertainty in T_{Refl} would cause an error of less than 4.5 mK in $T_{A,atm}$. The reflector surfaces are not necessarily uniform, however: The variation in emission over the reflector surface is unknown, but if one uses ±40 mK as a representative estimate, the change in the surface area viewed by the antenna when the reflector is set for sky measurements at the various zenith angles results in an uncertainty of up to ±50 mK in values of $T_{A,atm}$ measured at 40° and 0° zenith angles, and an uncertainty of up to ±40 mK in values of $T_{A,atm}$ measured at 50° and 0°.

1983: The 296 ± 40 mK value of T_{Refl} creates a ±40 mK uncertainty in T_{Zenith}, and hence in $T_{A,CBR}$.

8.3.1.3 Ground Radiation

1982: Very little radiation from the ground entered the radiometer during measurements of T_{Zenith} from either year. The upward-looking antenna was pointed directly at the zenith in 1982, so the horizon was typically 80° or more from the beam axis. The integral of the antenna pattern at angles greater than 80° indicates that $T_{Z,gnd}$ was less than 1 mK in 1982.

Ground radiation can also affect measurements of $T_{A,atm}$ when the antennas observe the sky at large zenith angles. Ground shields extend above the horizon to block out the radiation, emitted by objects near the horizon, but some radiation is still diffracted over the edge of the ground shields into the antennas. The amount of power diffracted into the antennas is of course strongly dependent on the zenith angle being viewed.

Tests of the radiometer have set 8-mK upper limits on values of $T_{atm,gnd}$ at 40° and 50°. From equations (7.6) and (8.4), these limits place uncertainties of 28 mK and 15 mK on values of $T_{A,atm}$ obtained from observations at 40° and 50°, respectively.

1983: Changes in the orientation of the antennas have made the radiometer slightly more sensitive to ground radiation. With the antenna looking downward at a reflector to view the zenith, care has been taken to test the effectiveness of the ground shielding. Our tests yield a value of 12 ± 15 mK for $T_{Z,gnd}$.

Tests show that the value of $T_{atm,gnd}(50,10)$ is less than 27 mK. Similar measurements have not been performed at 40°, but one can derive an upper limit from the measurements at 50° by considering the diffracted radiation as a line source eminating from the upper edge of the ground shield, at a zenith angle of 70°. When the antenna points 50° from the zenith, the edge of the shield is 20° to 25° away from the antenna axis; when the antenna points 40° from the zenith, the shield edge is 30° to 35° from the axis. Therefore, the diffracted power seen by the antenna is reduced by the ratio of the antenna responses at the two angles, at least a factor of 10, so the contribution of diffracted ground radiation to the sky temperature observed at 40° must be less than 2.7 mK. The corresponding uncertainties in $T_{A,atm}$ are $^{+11}_{-0}$ mK in measurements made at 40° and $^{+49}_{-0}$ mK in the 50° measurements.

8.3.1.4 Gain Calibration and Linearity

How do errors in the gain calibration affect the results? Suppose the calibration coefficient obtained in the course of a single measurement sequence is G_0, whereas the actual calibration coefficients are G_1 during the T_{Zenith} measurement and G_2 during the measurement of $T_{A,atm}$; G_1 and G_2 need not be equal to each other or to G_0. Let the terms calculated using the measured calibration coefficient G_0 be indicated by primes. It follows from equations (7.3) that the error T_{Zenith} resulting from the calibration error is

$$\begin{aligned} T_{Zenith} - T'_{Zenith} &= \frac{(G_1 - G_0)}{2}(V_{Zenith/Load} - V_{Load/Zenith}) \\ &= \left(\frac{G_1}{G_0} - 1\right)\frac{G_0}{2}(V_{Zenith/Load} - V_{Load/Zenith}) \qquad (8.5) \\ &\simeq \delta G_1(T_{Zenith} - T_{Load}) \end{aligned}$$

where $\delta G_1 \equiv (G_1 - G_0)/G_0$.

The error in $T_{A,atm}$ can be calculated similarly. If the error in G_0 is small, then from equation (7.7),

$$\begin{aligned} T_{A,atm} - T'_{A,atm} &= \hat{T}_{Atmos,1}\left(\epsilon - \epsilon'\right) + \hat{T}_{Atmos,2}\left(\epsilon^2 - \epsilon'^2\right) + \hat{T}_{Atmos,3}\left(\epsilon^3 - \epsilon'^3\right) \\ &\simeq \left(\frac{\epsilon - \epsilon'}{\epsilon'}\right)\left(\hat{T}_{Atmos,1}\epsilon' + 2\hat{T}_{Atmos,2}\epsilon'^2 + 3\hat{T}_{Atmos,3}\epsilon'^3\right) , \end{aligned} \qquad (8.6)$$

where primed and unprimed variables represent respectively the values one obtains using the measured and true calibration coefficients, and where the θ's have been suppressed for compactness. From equations (7.5) and (7.6),

$$\frac{\epsilon - \epsilon'}{\epsilon'} \simeq \left(\frac{G_2 - G_0}{G_0}\right) \equiv \delta G_2.$$

The approximation, which results from neglect of the term $(1 - \Delta T_{Flip}/G_0\Delta V)^{-1}$ on the right-hand side of the equation, introduces an error of less than 1% in $(\epsilon - \epsilon')/\epsilon'$. Thus equation (8.6) can be written:

$$\begin{aligned} T_{A,atm} - T'_{A,atm} &\simeq T'_{A,atm}\delta G_2\left[1 + \left(\frac{\hat{T}_{Atmos,2}\,\epsilon' + 2\hat{T}_{Atmos,3}\,\epsilon'^2}{\hat{T}_{Atmos,1} + \hat{T}_{Atmos,2}\epsilon' + \hat{T}_{Atmos,3}\epsilon'^2}\right)\right] \\ &= T'_{A,atm}\delta G_2\left[1 + R_2\epsilon' + \left(2R_3 - R_2^2\right)\epsilon'^2 + O\left(\epsilon'^3\right)\right] \end{aligned} \qquad (8.7)$$

where $R_n \equiv \hat{T}_{Atmos,n}/\hat{T}_{Atmos,1}$.

The error in $T_{A,CBR}$ due to gain-calibration errors is approximately equal to the difference between equations (8.5) and (8.7):

$$\begin{aligned}\Delta T_{A,CBR} &= \left(T_{Zenith} - T'_{Zenith}\right) - \left(T_{A,atm} - T'_{A,atm}\right) \\ &\simeq \delta G_1 \Delta T'_{Zenith/Load} - \delta G_2 T'_{A,atm} - \delta G_2 T'_{A,atm}\left[R_2\epsilon' + \left(2R_3 - R_2^2\right)\epsilon'^2\right].\end{aligned}$$

$\Delta T'_{Zenith/Load}$ is approximately equal to $T'_{A,atm} + T_{A,CBR} - T_{Load}$. With this substitution and some regrouping, the equation becomes

$$\begin{aligned}\Delta T_{A,CBR} = {} & \left(\delta G_1 - \delta G_2\right) T'_{A,atm} + \delta G_1\left(T_{A,CBR} - T_{Load}\right) \\ & - \delta G_2 T'_{A,atm}\left[R_2\epsilon' + \left(2R_3 - R_2^2\right)\epsilon'^2\right].\end{aligned} \tag{8.8}$$

Equation (8.8) contains three terms: The first is proportional to the difference $\delta G_1 - \delta G_2$, and the other two are proportional to δG_1 and δG_2 respectively. The size of the first term depends not on any error in the measurement of the calibration coefficient, but rather on the amount by which the calibration drifts during the measurement cycle. The calibration drift can be estimated from the data in Tables 7.3 and 7.4. The largest drifts occurs on the nights of 5 and 6 September 1983 (U.T.), during periods when the heater was not operating. The average fractional drift between successive measurement cycles on those nights is $9.3 \pm 1.7 \times 10^{-4}$ on 5 September and $6.4 \pm 1.5 \times 10^{-4}$ on 6 September; the drift is much smaller during the other measurement runs. Taking $\delta G_1 - \delta G_2$ to be less than or equal to 9.3×10^{-4} and $T_{A,atm}$ to be less than or equal to 12 K, one can set a conservative upper limit on their product: $\left(\delta G_1 - \delta G_2\right) T_{A,atm} \leq 11$ mK.

Errors in the gain-calibration measurement could cause the second and third terms in equation (8.8) to be significant even though the calibration drift is negligible. The second term is equal to the product of δG_1 and the antenna-temperature difference between the CBR and the cold load ($\simeq -1$ K), so a 1% calibration error during T_{Zenith} measurements causes an error of 10 mK in $T_{A,CBR}$. The third term in equation (8.8) owes its existence to atmospheric self-absorption. Over the range of atmospheric conditions that occured during the CBR measurements, the value of the term lies in the range from $0.4\delta G_2$ to $0.5\delta G_2$ Kelvins, so the error in $T_{A,CBR}$ which results from a 1% calibration error during measurements of $T_{A,atm}$ is approximately 5 mK.

How large are δG_1 and δG_2? The calibrations are stable to at least the 10^{-3} level, so significant miscalibrations could only be caused by some systematic error in the calibration procedure, such as incorrect calibration-load temperatures or nonlinear radiometer response.

A sensor on the ambient load monitors its physical temperature with an accuracy better than ±1 K; the uncertainty in the effective temperature of the cold load is less than ±0.1 K. The fractional error in G due to inaccurate temperature measurement is therefore less than $\pm 1.1/(270)$ or ±0.41% . The transparency of the ambient load causes an error of less than ±0.04% in G; reflection from its surface results in an error of approximately ±0.2%. The sum of these terms, ±0.65%, is a conservative limit on the fractional error δG due to inaccurate estimates of the radiometric temperatures of the calibration loads. The resulting limit on the uncertainty in $T_{A,CBR}$ is 10 mK.

The position-dependent gain modulation mentioned in § 6.1.2 also contributes some uncertainty to $T_{A,CBR}$. Let δG be the fractional variation in G due to rotation of the radiometer. If gain modulation occurs during measurements of T_{Zenith} and G, the resulting error in T_{Zenith} is

$$\Delta T_{Zenith} = \frac{\delta G}{2} T_{Offset}$$

where T_{Offset} is the offset temperature of the radiometer. For a value of δG equal to 10^{-3} and a 5.2 K offset temperature, $\Delta T_{Zenith} \simeq 3$ mK.

The gain modulation also affects measurements of $T_{A,atm}$. In this case, two effects must be considered. First, there is the systematic variation in G between observations to the north and to the south. Tests have shown that the fractional change in G during atmospheric scans is approximately 10^{-4}, so this error can be neglected. Second, systematic differences in the value of G during zenith measurements and during atmospheric measurements give rise to an error:

$$\Delta T_{A,atm} = \delta G T'_{A,atm} \, .$$

If $T'_{A,atm} \simeq 12$ K and $\delta G \simeq 10^{-3}$, $\Delta T_{A,atm}$ is ±12 mK.

The uncertainty in $T_{A,CBR}$ due to gain modulations is the quadrature sum of the modulation-induced errors in T_{Zenith} and $T_{A,atm}$, ±12 mK.

The linearity of the radiometer's response can be verified from the measurements made at White Mountain. If the radiometer's output voltage were not proportional to the temperature difference between the target loads, the value of the calibration coefficient would vary depending on the temperatures of the target loads. In particular, one would expect that at higher input temperatures, the radiometer response would increasingly depart from linearity, so that the calibration coefficient measured with one of the loads at ambient temperature would not be an accurate measurement of the radiometer response to low-temperature targets like the sky and the cold load.

The observations of 30 August 1983 include radiometer calibrations made with ambient and LN-cooled targets; the data from 4 September 1983 include calibrations made under similar conditions but with LHe in the cold load. Data from the two nights can be combined to yield the calibration coefficient which would result if the calibrations were made using targets at the temperatures of LN and LHe, instead of an ambient temperature target and a cold one. The resulting coefficient differs by only 1.1% from the calibration coefficient measured with ambient and LN-cooled targets; the discrepancy between the two values is compatible with the uncertainties in the calibrations themselves. Therefore, any nonlinearity in the radiometer response affects G by less than 1.1% over the range of temperatures viewed by the radiometer during CBR measurements, and causes an error of less than ±17 mK in $T_{A,CBR}$.

The net effect of the various calibration uncertainties is that the measured calibration coefficient G is in error by no more than ±1.3% at the time of measurement, and it drifts by no more than ±0.1% before it is remeasured. These uncertainties give rise to estimated errors of ±23 mK in $T_{A,CBR}$ and ±160 mK in $T_{A,atm}$.

8.3.2 Cold-Load Uncertainties

The antenna temperature that the radiometer sees when it views the cold load is the sum of the power emitted by the cold target, by the aluminum-coated surface of the false wall, and by the windows, plus the noise power broadcast by the radiometer itself and reflected back into the antenna by the load (mostly by the windows). Uncertainties in all of these contributions give rise to an overall uncertainty in $T_{A,Load}$.

The temperature of the cold Eccosorb target is determined by its surroundings. When immersed in LHe, its temperature is that of the boiling LHe, dictated by the ambient pressure within the cold load. Both the target temperature and the cold-load pressure are monitored. The cold-load pressure during the CBR measurements, 488 ± 2 mm Hg, implies a target temperature of 3.776 ± 0.004 K (Brickwedde *et al.* 1960) or 2.020 ± 0.004 K in units of antenna temperature. This value is verified by two temperature sensors mounted within the target, which showed temperatures of 3.773 ± 0.020 K and 3.795 ± 0.020 K during the 1983 CBR measurements. From equation (2.3), the antenna temperature of the target, $T_{A,LHe}$, is 2.020 ± 0.004 K.

The LHe level was monitored during the CBR measurement runs, and cryogen was added as needed to keep the target immersed. The observations at 3.3 mm show no sign of the systematic time-variation in T_{Load} that one would expect if the target had emerged from the LHe.

T_{Wall}, the contribution from the false wall, is determined by the wall's emissivity and temperature profile and by the antenna response over the solid angle that it subtends. The wall's inner surface is clean aluminum, with an estimated emissivity smaller than 5×10^{-3} over the range of incidence angles at which the antenna views the wall. However, a thin layer of nitrogen frost with an unknown thickness and emissivity was observed on the lower part of the wall after LHe had been added to the cold load.

Despite these uncertainties in the properties of the lower wall, one may still set an upper limit on T_{Wall}. Measurements show that the integral of the antenna gain over the solid angle subtended by the false wall is approximately 0.7% of the beam solid angle. The average temperature of that part of the wall seen by the antenna is 30 K or less. Finally, the emissivity of a thin (probably less than 1-mm) layer of nitrogen frost is almost certainly less than 0.1. Therefore, T_{Wall} is less than $.007 \times 30 \times 0.1$ Kelvins, or 20 mK. This value is an upper limit; the true value of T_{Wall} lies somewhere between 0 and 20 mK, depending upon the temperature and emissivity of the frost layer. The data analysis uses the value 10 ± 10 mK for T_{Wall}.

The two windows on the top of the cold load increase the radiometric temperature of the load through two mechanisms: emission and reflection. $T_{Windows}$ is the sum of the contributions from both mechanisms. To first order, the antenna temperature of each of the windows is equal to the product of its temperature (roughly ambient), its emissivity, and its thickness (23 micrometers). This temperature increment has been measured to be 9.2 ± 2.3 mK per window.

A more important contribution comes from the a small fraction of the radiation striking the windows from above is reflected into the antenna. One can easily show that the power reflectivity r of a dielectric window with thickness t and dielectric constant ϵ is given by:

$$r = \left[\pi(\epsilon - 1)\frac{t}{\lambda}\right]^2 . \tag{8.9}$$

This formula is valid as long as t is small compared to the wavelength λ. A 23-micrometer-thick polyethylene film, with an ϵ of 2.26, has a theoretical reflectivity of 7.5×10^{-4} at 3.3 mm wavelength.

The radiation reflected into the antenna comes partly from the cold load and partly from the antenna itself; the proportions vary depending on the distance from antenna to window. If the window is immediately in front of the antenna mouth, a fraction r of the microwave power emerging from the antenna is reflected back into the antenna. As the window is moved away from the antenna, the fraction of the broadcast power reflected by the window is still r, but not all the reflected power re-enters the antenna. Some of it misses the antenna and strikes the coupling plate, which reflects most of it downward into the absorber at the bottom of the cold load.

The two windows are of course at different distances from the antenna, and both of them are moved up and down by the changing pressure of the cold load. Tests indicate that depending upon its position, the upper window reflects between 0 and 1.0×10^{-3} of the power broadcast by the antenna back into the antenna. The maximum measured reflection coefficient is about 30% larger than the theoretical value derived from equation (8.9). The lower window is far enough from the antenna so that it reflects a negligible amount of broadcast power back into the antenna.

The amount of power broadcast by one antenna depends upon the target being viewed by the other antenna, since the Dicke switch causes the microwave radiation entering the unused radiometer port to exit through the port connected to the receiver. Thus, when the radiometer views the cold load, the power broadcast into the load by the antenna is the sum of the power entering the upward-looking antenna and the thermal noise generated by the switch itself, a total of about 70 K. Power broadcast from the antenna thus adds from 0 to 70 mK, or 35 ± 35 mK to the antenna temperature of the upper window.

Reflected power which does not come from the antenna must originate inside the cold load, radiated either by the coupling plates and bellows at the top of the load ($\epsilon T \sim 350$ mK), by the false wall ($\epsilon T \sim 350$ mK near the top; $\epsilon T \leq 3$ K near the bottom where nitrogen frost occurs), or by the target. If all the power reflected into the antenna by both windows is emitted by the nitrogen frost, the resulting increase in $T_{Windows}$ is less than $2 \times 10^{-3} \times 3$ K, or 6.0 mK. In other cases the increase is smaller. This contribution can therefore be neglected.

$T_{Windows}$, the sum of the emitted and reflected contributions from both windows, is 53 ± 35 mK.

The sum of $T_{Windows}$, T_{Wall}, and $T_{A,LHe}$ is $T_{A,Load}$. Its value is 2.083 ± 0.037 K.

8.3.3 Atmosphere-Related Uncertainties

Uncertainties in $T_{A,atm}$ fall into two categories: uncertainty in the zenith angles observed during atmospheric zenith scans and uncertainties in the parameters of the atmospheric model used to calculate $T_{A,atm}$ from the zenith scans.

8.3.3.1 Pointing Errors

Pointing errors can result from a number of causes. If the cart is improperly leveled for instance, the zenith angles viewed by the antennas will differ from their expected values. Pointing errors can also occur if the beam separation of the two antennas is not known accurately, or if the orientations of the reflectors (in the 1982 design) and the radiometer (in both designs) are not measured correctly relative to the cart.

Pointing errors can be classified according to the way that the errors at the four zenith angles are correlated. This division is useful for the purpose of error analysis because the effect of pointing errors on $T_{A,atm}$ depends not only on the magnitude of the errors but also on their correlation. For example, one might expect that tilting of the cart toward the north or south, a major source of pointing error, would also be a dominant source of error in $T_{A,atm}$, but such is not the case. The north-south symmetry of the radiometer and the atmospheric measurements causes the pointing errors to correlate in such a way that they compensate for one another—increased values of T_{Sky} at Z_2 and Z_4 are largely offset by the reductions at Z_1 and Z_3, and vice versa.

The categories of pointing error are:

1. Pointing errors which have equal and opposite values for northward and southward-looking observations (cart tipping in the north-south plane, for example).
2. Pointing errors which have the same value and sign on both sides (such as cart tipping in the east-west plane, or inaccurate measurement of the beam separation between the two antennas).
3. Equal and opposite errors in two zenith angles—Z_1 and Z_3, or Z_2 and Z_4—with no associated error in the other two zenith angles (for instance the error that could occur in the 1983 configuration if the orientation of the radiometer in one of its scan positions is incorrectly measured).
4. Errors at one zenith angle not correlated with errors elsewhere (such as poorly measured reflector settings in the 1982 configuration).

Since the four types of pointing error affects $T_{A,atm}$ differently, it is useful to have a mathematical expression for the error in $T_{A,atm}$ for each of the four varieties of pointing error. One can derive tractable and surprisingly accurate expressions for the effects of pointing errors on $T_{A,atm}$ from the simple model

$$T_{Sky}(Z) \simeq T_{A,atm} \sec(Z). \qquad (8.10)$$

Although the expressions derived from this model are only approximate, They provide useful insight into the way that the error in $T_{A,atm}$ varies with the zenith angles Z_1–Z_4 and with the various types of pointing error.

Pointing Errors of the First Type: To derive an expression for the error in $T_{A,atm}$ due to pointing errors of the first type, let Z_1–Z_4 be the assumed zenith angles (neglecting pointing error) and let Z_1'–Z_4' be the true zenith angles. Define the sign of the error such that a positive error increases the zenith angles of the southward-looking observations. If the error in the pointing angles is δ, then the primed and unprimed zenith angles are related as:

$$\begin{aligned} Z_1' &= Z_1 + \delta \\ Z_2' &= Z_2 - \delta \\ Z_3' &= Z_3 + \delta \\ Z_4' &= Z_4 - \delta. \end{aligned}$$

The ratio of the observed value of $T_{A,atm}$ to the true one is therefore

$$\begin{aligned} \frac{T'_{A,atm}}{T_{A,atm}} &= \frac{\sec(Z_1') + \sec(Z_4') - \sec(Z_2') - \sec(Z_3')}{\sec(Z_1) + \sec(Z_4) - \sec(Z_2) - \sec(Z_3)} \\ &= \frac{\sec(Z_1+\delta) + \sec(Z_4-\delta) - \sec(Z_2-\delta) - \sec(Z_3+\delta)}{\sec(Z_1) + \sec(Z_4) - \sec(Z_2) - \sec(Z_3)}. \end{aligned} \tag{8.11}$$

Define two difference angles β_1 and β_2 as:

$$\begin{aligned} \beta_1 &\equiv Z_4 - Z_1 \\ \beta_2 &\equiv Z_2 - Z_3. \end{aligned}$$

Both these angles are of order 1°, since $Z_1 \simeq Z_4$ and $Z_3 \simeq Z_2$. If $\beta_1 \simeq \beta_2$, as was the case in 1983 when they differed by only 1 arcminute, both can be represented as β and the zenith angles Z_2 and Z_4 can be expressed as

$$\begin{aligned} Z_2 &= Z_3 + \beta \\ Z_4 &= Z_1 + \beta. \end{aligned}$$

If β and δ are both much less than one radian, then when the expressions for Z_4 and Z_2 are substituted into the numerator of equation (8.11) the secant terms can be expanded around Z_1 and Z_3 using the Taylor-series expansion

$$\sec(Z+\delta) = \sec(Z)\left[1 + \delta\tan(Z) + \frac{\delta^2}{2}[1 + 2\tan^2(Z)] + \mathcal{O}(\delta^3)\right].$$

With some rearrangement, the expanded equation can be written as

$$\frac{T'_{A,atm}}{T_{A,atm}} = 1 + \left[1/2 + \left(\frac{\sec(Z_1)\tan^2(Z_1) - \sec(Z_3)\tan^2(Z_3)}{\sec(Z_1) - \sec(Z_3)}\right)\right] \times (\delta^2 - \beta\delta), \tag{8.12}$$

accurate to second order in δ, β, and cross terms.

Equation (8.12) shows that the error in $T_{A,atm}$ goes as $(\delta^2 - \beta\delta)$; if β were zero, the error would depend only on δ^2 and higher-order terms. Since β is not zero, the fractional error in $T_{A,atm}$ has a small linear dependence on δ.

The expressions derived numerically from the full atmospheric model, weighted by the antenna gain pattern, are

$$\frac{\Delta T_{A,atm}}{T_{A,atm}} = (1.16\ \delta^2 - 1.38\ \delta) \times 10^{-3} \qquad \theta = 40^\circ$$

$$\frac{\Delta T_{A,atm}}{T_{A,atm}} = (1.42\ \delta^2 - 1.66\ \delta) \times 10^{-3} \qquad \theta = 50^\circ$$

for δ in degrees. The coefficients in these expressions are approximately 5% higher than those derived from the simple model of equation (8.10). Note that as before, θ represents the *nominal* zenith angle, while Z symbolizes the *actual* zenith angle.

It is no accident that pointing errors of the first type have little influence on the results. Our need to minimize measurement errors due to cart misalignment was largely responsible for the north-south symmetry of the radiometer and the atmospheric measurements.

Pointing Errors of the Second Type: Pointing errors of the second type are potentially much more serious than those of the first type because they cause an error in $T_{A,atm}$ that varies linearly with δ. One derives an expression for $\Delta T_{A,atm}$ from equation (8.10) by the same steps used to derive expressions for Type 1 pointing errors except that the relations between the primed and unprimed zenith angles are now

$$\begin{aligned} Z_1' &= Z_1 + \delta \\ Z_2' &= Z_2 + \delta \\ Z_3' &= Z_3 + \delta \\ Z_4' &= Z_4 + \delta. \end{aligned}$$

The resulting expression for the fractional error in $T_{A,atm}$ is

$$\frac{\Delta T_{A,atm}}{T_{A,atm}} \simeq \left[\frac{\varsigma(Z_1) + \varsigma(Z_4) - \varsigma(Z_2) - \varsigma(Z_3)}{\sec(Z_1) + \sec(Z_4) - \sec(Z_2) - \sec(Z_3)}\right] \times \delta$$

where the function $\varsigma(Z)$ is defined as

$$\varsigma(Z) = \sec(Z)\tan(Z)$$

and small terms of order $\beta\delta$ and δ^2 have been neglected.

The expression for $\Delta T_{A,atm}/T_{A,atm}$ derived from the full atmospheric model yields values

$$\frac{\Delta T_{A,atm}}{T_{A,atm}} = 6.6 \times 10^{-2} \times \delta \qquad \theta = 40^\circ$$

$$\frac{\Delta T_{A,atm}}{T_{A,atm}} = 6.0 \times 10^{-2} \times \delta \qquad \theta = 50^\circ$$

for the zenith angles used in 1982 and

$$\frac{\Delta T_{A,atm}}{T_{A,atm}} = 5.3 \times 10^{-2} \times \delta \qquad \theta = 40^\circ$$

$$\frac{\Delta T_{A,atm}}{T_{A,atm}} = 5.6 \times 10^{-2} \times \delta \qquad \theta = 50^\circ$$

for the 1983 zenith angles. These values are approximately 4% larger than those derived from the simple secant model.

Pointing Errors of the Third Type: Pointing error of this sort are not likely to have occurred in 1982 because the reflectors were independently set in each position. In 1983 on the other hand, the design of the radiometer was such that an incorrect or incorrectly measured angle setting at one position gave rise to correlated errors in the zenith angles observed by the two horns—positive on one side and negative by the same amount on the other. Errors of this type occured at roughly the one-arcminute level in 1983—too small to be a major component in the error budget but large enough to be included for the sake of completeness.

The secant model leads to the following expression for the fractional error in $T_{A,atm}$ due to correlated errors of δ in Z_1 and Z_2:

$$\frac{\Delta T_{A,atm}}{T_{A,atm}} \simeq \left[\frac{\varsigma(Z_1)+\varsigma(Z_2)}{\sec(Z_1)+\sec(Z_4)-\sec(Z_2)-\sec(Z_3)}\right] \times \delta,$$

accurate to first order in δ. When the 1983 zenith angles are substituted into this expression, the result is

$$\frac{\Delta T_{A,atm}}{T_{A,atm}} = 5.3 \times 10^{-2} \times \delta \qquad \theta = 40^\circ$$

$$\frac{\Delta T_{A,atm}}{T_{A,atm}} = 3.2 \times 10^{-2} \times \delta \qquad \theta = 50^\circ$$

for the 1983 zenith angles.

Pointing Errors of the Fourth Type: Uncorrelated pointing errors at the four zenith angles caused large errors in $T_{A,atm}$ in 1982. If the zenith angle Z_n is in error by an amount δ, the effect of the pointing error on $T_{A,atm}$ can be calculated from the by-now-familiar secant model; the resulting expression is

$$\frac{\Delta T_{A,atm}}{T_{A,atm}} \simeq \pm \left[\frac{\sec(Z_n)\tan(Z_n)}{\sec(Z_1)+\sec(Z_4)-\sec(Z_2)-\sec(Z_3)}\right] \times \delta$$

to first order in δ. The sign of the error in $T_{A,atm}$ is positive for pointing errors in Z_1 and Z_4, and negative for errors in Z_2 and Z_3.

It is clear from the equation that the effect of this type of pointing error on $T_{A,atm}$ depends greatly on the zenith angle at which the error occurs. Because of its dependence on $\sec(Z)\tan(Z)$, the error in $T_{A,atm}$ which results from a pointing error in Z_2 or Z_3 is at least a factor three smaller than one caused by a pointing error of the same size in Z_1 or Z_4. In fact, when Z_2 or Z_3 is zero, pointing errors at these angles cause no error in $T_{A,atm}$ to first order. The fractional error in $T_{A,atm}$ due to pointing errors in Z_1 and Z_4 varies from $2.9 \times 10^{-2}\delta$ in the 50°/0° configuration to $4.0 \times 10^{-2}\delta$ in the 40°/20° configuration. The first-order error in $T_{A,atm}$ due to pointing errors in Z_2 and Z_3 ranges from 0 in the 50°/0° and 40°/0° to $1.4 \times 10^{-2}\delta$ in the 40°/20° configuration.

Having determined the quantitative effect of each type of error on $T_{A,atm}$, one can now use these expressions to estimate the total error in $T_{A,atm}$ due to errors in zenith angle. Before doing so however, one must show that the four pointing errors can be treated independently. Suppose the error angles associated with the four pointing errors in a given atmospheric measurement are δ_1, δ_2, δ_3, and δ_4. Because Types 2, 3, and 4 pointing errors cause temperature errors that are predominantly linear in the error angle, a combination of these types of pointing errors causes a temperature error proportional to a linear combination of δ_2, δ_3, and δ_4.

Type 1 pointing errors produce temperature errors that vary as δ^2, so in principle they cannot be treated independently of the other types of pointing error. However, any non-Type 1 pointing errors large enough to produce significant cross terms (proportional to $\delta_1\delta_2$, etc.) also cause such large linear errors in $T_{A,atm}$ that the quadratic errors are insignificant by comparison.

1982: The main source of Type 1 pointing errors in 1982 is north-south cart tilt. Cart tilt of 1° or less and a difference of approximately 1° in the northward and southward zenith angles result in a maximum error of approximately 30 mK in $T_{A,atm}$.

Type 2 pointing errors result from east-west cart tilt and from antenna misalignment. If the cart tilts to the east or west by an angle ϕ, the new zenith angles are given by the equation

$$\sec(Z'_n) = \sec(Z_n)\sec(\phi).$$

In the secant model the ratio of the measured atmospheric emission to its true value is

$$\frac{T'_{A,atm}}{T_{A,atm}} = \sec(\phi) \simeq 1 + \frac{\phi^2}{2},$$

so if the tilt angle is 1° and $T_{A,atm}$ is 11 Kelvins, the error in $T_{A,atm}$ is only 1.7 mK—clearly not significant.

On 3 July 1982, the axes of the two antennas were measured to be parallel to ±10 arcminutes in the vertical plane. This uncertainty in the antenna alignment is the main Type 2 pointing error in the 1982 measurements. It can lead to an error in $T_{A,atm}$ of up to 115 mK.

Type 3 pointing errors were of little consequence, due to the radiometer design used in 1982.

On the other hand, uncertainty in the reflector positions from that year resulted in such large Type 4 errors that they became the leading source of error in $T_{A,atm}$ and T_{CBR}. The reflector settings were measured on 3 July and again on 9 July 1982. Warping reflectors and inadequate measuring tools caused the zenith angles measured on the two days to differ by as much as 2.3°. Because neither set of zenith-angle values is trustworthy, the observations have been analyzed using both sets of angles. Each measurement cycle yields two values of $T_{A,atm}$—one for each set of angle factors used in the calculation—and two values of $T_{A,CBR}$. The values derived using the zenith-angle measurements of 3 July and 9 July are subscripted 1 and 2 respectively. Table 7.3 shows that neither set of angles yields values of $T_{A,atm}$ which are consistent at 40° and 50° and that the values of $T_{A,CBR}$ are systematically different on 5 July and 6 July, probably because the reflectors underwent further warping on 6 July, resulting in a systematic change in the error in $T_{A,atm}$.

Because there is no *a priori* reason to give preference to either set of angle measurements, to believe that one night's measurements of $T_{A,atm}$ were more accurate than the other's, or to favor the results of the 50° zenith scans rather than those at 40° (or vice versa), we take an average of the values of $T_{A,CBR}$ from both nights, computed with both sets of angle factors. The spread in the values of $T_{A,CBR}$ derived in the various ways is used to estimate the Type 4 pointing error in $T_{A,atm}$ due to errors in the zenith angles.

Analysis of the first measurement run yields four mean values of $T_{A,CBR}$: two values (one for each set of angle factors) from the measurement cycles that include atmospheric measurements at 40° and two more values from the cycles with 50° scans. These four averages are listed in Table 7.3 as the mean values of $T_{A,CBR1}$ and $T_{A,CBR2}$ for θ of 40° and 50°for 5 July.

The two measurement runs from 6 July, runs number 2 and 3, are analyzed the same way. Because of the systematic shift in the values of $T_{A,CBR}$ from 5 July to 6 July, the results of each of the runs on 6 July are given half the weight of the results of the single run on 5 July, in order to give equal weighting to the results of both days. This is done by averaging each of the four $T_{A,CBR}$ values—$T_{A,CBR1,40}$, $T_{A,CBR2,40}$, $T_{A,CBR1,50}$, and $T_{A,CBR2,50}$—from run 2 with the corresponding value from run 3. Table 8.1 lists the four entries from the first measurement run (5 July) and the four averaged entries from runs 2 and 3 (6 July).

The mean of the eight values in Table 8.1 is 1.00 Kelvin with a standard deviation of 0.55 K. One could wish for more precise and more rigorously derived estimates of $T_{A,CBR}$ and of the uncertainty that Type 4 pointing errors caused, but one would be destined to wish in vain. The total uncertainty in $T_{A,atm}$ and $T_{A,CBR}$ from pointing errors is ±0.56 K, the quadrature sum of the uncertainties due to Type 1, Type 2, and Type 4 pointing errors.

<u>1983:</u> Moveable reflectors were not used in 1983, and the systematic errors in $T_{A,atm}$ were greatly reduced.

Type 1 pointing errors contributed little to the uncertainty in the 1983 measurements. Comparisons of the atmospheric observations made to the north and south during the CBR

Run Number	40° Zenith Scans		50° Zenith Scans	
	$T_{A,CBR,1}$ (mK)	$T_{A,CBR,2}$ (mK)	$T_{A,CBR,1}$ (mK)	$T_{A,CBR,2}$ (mK)
1	549 ± 113	970 ± 109	974 ± 80	1954 ± 73
2 and 3	419 ± 50	877 ± 69	586 ± 98	1671 ± 78

Table 8.1: Averages of 1982 $T_{A,CBR}$ measurements.

measurements indicate that the cart could not have been tilted by more than half a degree while over the cold load. If $T_{A,atm}$ is taken as 11 K, these values limit the component of $\Delta T_{A,atm}$ due to north-south tilt to 11 mK or less for atmospheric measurements at 40° and 13 mK or less for those at 50°.

Among the Type 2 pointing errors, east-west cart tilt contributed only 2 mK to the overall error budget. More important was the pointing error caused by the $\pm 0\overset{\circ}{.}007$ uncertainty in the beam separation of the two antennas (discussed in Appendix C), which gave rise to a ±40 mK uncertainty in $T_{A,atm}$.

Type 3 pointing errors might have occurred at one or more positions if the restraining mechanism that held the radiometer in place were loose or if the radiometer positions had been measured inaccurately. In addition to the position measurements of 8 September, the positions were also measured on 29 August. Comparison of the two set of measurements shows that the angles were systematically different by 3 arcminutes (Type 1 error) with a scatter of ±2 arcminutes (Type 3 error). A two-arcminute Type 3 pointing error causes measurements of $T_{A,atm}$ made at 40° and 20° to be in error by 19 mK and 12 mK when the observations are made at $\theta = 40°$and $\theta = 50°$, respectively.

The design of the radiometer prevented the antennas from being pointed independently, and thus effectively eliminated Type 4 pointing errors. For that reason, the error in $T_{A,atm}$ caused by Type 4 pointing errors can be neglected.

The total estimated error in the 1983 measurements of $T_{A,atm}$ (and $T_{A,CBR}$) due to pointing errors is the quadrature sum of the error estimates for Types 1, 2, and 3 pointing errors, ±45 mK.

8.3.3.2 Atmospheric-Model Uncertainties

In order to calculate $T_{A,atm}$ from measurements of the atmosphere, the measurements are fitted to an atmospheric model. The three sets of data that go into the atmospheric calculations are the antenna gain pattern, which is used to determine the effects of beam spread, and the temperature and emissivity profiles assumed for the atmosphere. In addition, the calculations assume that the atmosphere overhead has the same physical characteristics (e.g. temperature profile, water-vapor distribution) as the atmosphere actually observed during zenith scans. To the extent that the model departs from the actual characteristics of the atmosphere, the departures cause errors in $T_{A,atm}$.

Two independent measurements and one theoretical calculation of the antenna gain pattern were used to calculate $T_{A,atm}$; the resulting values varied by ±6 mK depending upon which gain pattern was used. This value is taken to be the uncertainty in $T_{A,atm}$ resulting from uncertainty in the gain pattern.

The temperature profile used for the calculations, discussed in Appendix A, is adapted from the 1962 U. S. Standard Atmosphere (Cole *et al.* 1965). It assumes that the air temperature decreases uniformly with altitude from ground level to the tropopause, then increases at a slower rate up to the stratopause.

$T_{A,atm}$ is remarkably unaffected by the details of the temperature profile used in the computations, due to the fact that the temperature of the atmosphere only enters into the term for atmospheric self-absorption. If the temperature at every altitude is uniformly increased by an amount T', the rate of change in $T_{A,atm}$, $dT_{A,atm}/dT'$, is only -1.6 mK/K. An overall error of ±10 K in the temperature profile leads to a ±16 mK error in $T_{A,atm}$.

One can also estimate the effect that the structural details of the the temperature profile have on $T_{A,atm}$. Let $\overline{T}_{Atm}$ be the average temperature of the atmosphere, weighted at each altitude by the specific emissivity and the atmospheric absorption between that altitude and ground level. If $T_{A,atm}$ is calculated under the assumption that the atmospheric temperature is $\overline{T}_{Atm}$ irrespective of altitude, the resulting value differs by less than 7 mK from the value derived from the full atmospheric model.

The densities of both oxygen and water vapor decrease approximately exponentially with altitude, but the scale heights differ for the two gases (typically the scale height is 9.5 km for oxygen and 2.2 km for water vapor). Atmospheric radiation is produced by both molecular species, in varying proportions depending upon the water-vapor content of the atmosphere during the observations, so the atmospheric model assumes an exponential density distribution but leaves the scale height as a free parameter. Model calculations show that oxygen contributes roughly 5 K to the zenith temperature at 3800 meters altitude, so oxygen and water vapor make roughly equal contributions to the zenith temperatures observed in 1983 (Costales *et al.* 1985). Therefore, the true value of $T_{A,atm}$should lie approximately midway between the value calculated using a 9.5-km density scale height and the one derived from a 2.2-km scale height. If the scale heights of oxygen and water vapor are each used to compute $T_{A,atm}$, the resulting temperatures differ by 38 mK or less; the assumed value of $T_{A,atm}$ is the average of the two values and the uncertainty is half the difference: ±19 mK.

The overall uncertainty in $T_{A,atm}$ due to model-related errors is the quadrature sum of the individual error estimates, ±26 mK. This same error also contributes to the overall uncertainty in $T_{A,CBR}$.

8.4 Summary

Tables 8.2 and 8.3 list the terms that enter into the computation of $T_{A,CBR}$ and the estimated errors associated with each term in 1982 and 1983. The total estimated uncertainties, ±570 mK in 1982 and ±89 mK in 1983, are quadrature sums of the entries in the two tables.

Term	Value	Source of Error	Section	Error Value	Error in $T_{A,CBR}$
		Gain			
G	9.70 to 10.54 mK/du				
		Gain Drift	8.3.1.4	±0.07%	±8 mK
		Calibration-Load Uncertainties	8.3.1.4	±0.65%	±10 mK
		Angular dependence	8.3.1.4	±0.1%	±12 mK
		Nonlinearity	8.3.1.4	±1.1%	±17 mK
		Total:		±1.3%	±24 mK
		T_{Zenith}			
$\Delta T_{Z,Flip}$	0 mK	Offset Changes	8.3.1.1	±100 mK	±50 mK
$T_{Z,gnd}$	0 mK	Ground Radiation	8.3.1.3	$^{+1}_{-0}$ mK	$^{+0}_{-1}$ mK
$T_{A,Load}$:			8.3.2		
$T_{A,LHe}$	2020 mK	Temperature Uncertainty		±4 mK	
$T_{Windows}$	53 mK	Window Emission and Reflection		±35 mK	
T_{Wall}	10 mK	Wall Temperature and Emissivity		±10 mK	
Total:	2083 mK			±37 mK	±37 mK
		$T_{A,atm}$			
$T_{atm,gnd}$	0 mK	Ground Radiation	8.3.1.3	$^{+8}_{-0}$ mK	$^{+22}_{-0}$ mK
T_{Refl}	290 mK	Reflector Emission	8.3.1.2	±40 mK	±45 mK
Pointing Errors:					
Type 1		Cart Tilt	8.3.3.1	±1°	±30 mK
Type 2		Antenna Misalignment	8.3.3.1	±10′	±115 mK
Type 4		Reflector Misalignment	8.3.3.1	±1°	±550 mK
Modeling Errors:		Atmospheric Temperature and Emissivity Profiles	8.3.3.2		±26 mK
Statistical Uncertainty		Atmospheric Fluctuations and Radiometer Noise	8.2		±34 mK
				Total:	±570 mK

Table 8.2: Terms and estimated errors in the derivation of $T_{A,CBR}$ from the 1982 measurements.

Term	Value	Source of Error	Section	Error Value	Error in $T_{A,CBR}$
		Gain			
G	8.75 to 9.20 mK/du				
		Gain Drift	8.3.1.4	±0.09%	±11 mK
		Calibration-Load Uncertainties	8.3.1.4	±0.65%	±10 mK
		Angular dependence	8.3.1.4	±0.1%	±12 mK
		Nonlinearity	8.3.1.4	±1.1%	±17 mK
		Total:		±1.3%	±26 mK
		T_{Zenith}			
$\Delta T_{Z,Flip}$	20 mK	Offset Changes	8.3.1.1	±17 mK	±9 mK
$T_{Z,gnd}$	12 mK	Ground Radiation	8.3.1.3	±12 mK	±15 mK
T_{Refl}	296 mK	Reflector Emission	8.3.1.2	±40 mK	±40 mK
$T_{A,Load}$:			8.3.2		
$T_{A,LHe}$	2020 mK	Temperature Uncertainty		±4 mK	
$T_{Windows}$	53 mK	Window Emission and Reflection		±35 mK	
T_{Wall}	10 mK	Wall Temperature and Emissivity		±10 mK	
Total:	2083 mK			±37 mK	±37 mK
		$T_{A,atm}$			
$T_{atm,gnd}$	0 mK	Ground Radiation	8.3.1.3	$^{+15}_{-0}$ mK	$^{+30}_{-0}$ mK
$\Delta T_{Flip}(40,20)$	−13 mK	Offset Changes	8.3.1.1	±10 mK	±21 mK
$\Delta T_{Flip}(50,10)$	−10 mK	Offset Changes	8.3.1.1	±13 mK	±12 mK
Pointing Errors:					
Type 1		Cart Tilt	8.3.3.1	±30′	±12 mK
Type 2		Antenna Misalignment	8.3.3.1	±0.4′	±40 mK
Type 3		Inaccurate Positions	8.3.3.1	±2′	±16 mK
Modeling Errors:		Atmospheric Temperature and Emissivity Profiles	8.3.3.2	–	±26 mK
Statistical Uncertainty		Atmospheric Fluctuations and Radiometer Noise	8.2		±16 mK
				Total:	±90 mK

Table 8.3: Terms and estimated errors in the derivation of $T_{A,CBR}$ from 1983.

Chapter 9

Results and Interpretation

9.1 Results of These Measurements

The values of the CBR antenna temperature derived in Chapters 7 and 8,

$$T_{A,CBR} = 1.00 \pm 0.57 \text{ K} \qquad \text{in 1982}$$
$$T_{A,CBR} = 0.99 \pm 0.09 \text{ K} \qquad \text{in 1983,}$$

are converted to thermodynamic temperatures by means of the equation:

$$T_{CBR} = \frac{T_\nu}{\ln(1 + T_\nu / T_{A,CBR})}$$

to yield:

$$T_{CBR} = 2.58^{+0.68}_{-0.79} \text{ K} \qquad \text{in 1982}$$
$$T_{CBR} = 2.57 \pm 0.12 \text{ K} \qquad \text{in 1983.}$$

The weighted mean of the measurements from both years is $T_{CBR} = 2.57 \pm 0.12$ K, virtually equal to the 1983 value. That the results from 1982 and 1983 agree to 10 mK is certainly accidental, given the magnitude of the pointing errors in 1982.

The values quoted here for the 1982 results are somewhat different from those previously derived from the same measurements (Smoot *et al.* 1983, 1985), $T_{A,CBR} = 0.86 \pm 0.70$ and $T_{CBR} = 2.42 \pm 1.00$. The new values are the result of a careful reanalysis of the 1982 measurements, which has revealed two significant errors in the initial data analysis. The first error was the assumption that the antenna gain pattern could be modeled by a Gaussian profile. This assumption resulted in an error of approximately 140 mK in the values of $T_{A,atm}$ derived from zenith scans, which led in turn to a 160 mK error in T_{CBR}. The second error was an initially incorrect analysis of the CBR-measurement data for signs of a flip offset. Initially, the data-analysis algorithm used to calculate ΔT_{Offset} (eqn. 8.3) did not include the correction in the first term for the temperature difference of the loads. This omission resulted in an apparent change of 300 mK when the radiometer was rotated from horizontal to vertical. When the analysis was performed correctly, the estimate of the offset change was greatly reduced, substantially reducing the estimated uncertainty in the CBR measurements as a whole.

Our measurements of $T_{A,atm}$ have proven useful not only in the derivation of T_{CBR} but also in the study of atmospheric emission. The values of $T_{A,atm}$ observed during the CBR measurements at 3.3 mm range from approximately 9.0 K on 4 September 1983 to approximately 15 K on 6 July 1982. The atmospheric measurements from both years have been analyzed and compared with the results of simultaneous atmospheric measurements made with the other radiometers. These concurrent measurements provide a means of separating the temperature

Wavelength (cm)	Number of Observations	$T_{A,CBR}$	T_{CBR} Thermodynamic	Combined Results
12.0	6	2.49 ± 0.24	2.55 ± 0.24	2.78 ± 0.13
	18	2.82 ± 0.15	2.88 ± 0.16	
6.3	5	2.64 ± 0.21	2.74 ± 0.22	2.71 ± 0.08
	38	2.60 ± 0.08	2.71 ± 0.08	
3.0	82	2.68 ± 0.17	2.91 ± 0.17	2.75 ± 0.08
	59	2.41 ± 0.14	2.64 ± 0.14	
0.91	21	2.10 ± 0.20	2.82 ± 0.21	2.81 ± 0.12
	32	2.09 ± 0.13	2.81 ± 0.14	
0.33	29	1.00 ± 0.57	$2.58^{+0.68}_{-0.79}$	2.57 ± 0.12
	49	0.99 ± 0.09	2.57 ± 0.12	

Table 9.1: Results of our measurements of the CBR expressed in Kelvins. The first row at each wavelength is for the 1982 measurements; the second for 1983. The quoted errors are 68% confidence level.

contributions of oxygen from those of water vapor, since the day-to-day variations in the atmospheric water-vapor content alter the emission from water vapor at the various wavelengths without changing the contribution from oxygen. Although they cannot provide unambiguous values of the oxygen and water-vapor emission coefficients at the various wavelengths, they do establish relationships between the coefficients and set strong constraints on atmospheric-emission models (Waters 1976; Liebe 1981).

If values of $T_{A,atm}$ at 9.1 mm are plotted against concurrent values at 3.3 mm, the results fall approximately along a straight line whose slope is the ratio of water-vapor emission at 9.1 mm to that at 3.3 mm and whose intercept is determined by the amount of emission from oxygen at the two wavelengths. The atmospheric measurements of 1982 are consistent with Waters' atmospheric model (Partridge *et al.* 1984) but the uncertainties in the measurement limit the accuracy of the results. Our more recent measurements have yielded a slope of 0.24 ± 0.01 and an intercept of 1.87 ± 0.13 K (Figure 9.1). These values disagree not only with Partridge's computations from Water's model (slope = 0.16, intercept = 2.41 K) but also with the predictions of Liebe's model (Liebe 1985) (slope = 0.21, intercept = 2.24 K) and with computations by Costales *et al.* (1985) based on a modified form of Waters' (1976) model (slope = 0.17, intercept = 2.21 K). One can conclude from these comparisons that neither model correctly predicts the relationship between emission at 9.1 mm and 3.3 mm either for water vapor or for oxygen.

9.2 Comparison with Previous and Related Measurements

The results of our CBR measurements at all five wavelengths are shown in Table 9.1. The thermodynamic temperatures derived from the combined 1982 and 1983 measurements are con-

Reference	Wavelength (mm)	Frequency (GHz)	T_{CBR} (K)
Boynton *et al.* (1968)	3.33	90.0	$2.46^{+0.40}_{-0.46}$
Kislyakov *et al.* (1971)	3.58	83.8	2.4 ± 0.7
Millea *et al.* (1971)	3.32	90.4	2.61 ± 0.25
Boynton & Stokes (1974)	3.33	90.0	$2.48^{+0.50}_{-0.54}$
Weighted mean:			2.55 ± 0.19
This work	3.33	90.0	2.57 ± 0.12
Weighted mean of all values:			2.56 ± 0.10

Table 9.2: Past and present heterodyne measurements of the CBR temperature near 3.3 mm. The quoted errors are 68% confidence levels.

sistent with one another at all the wavelengths and have a weighted mean equal to 2.72 ± 0.04 K. They are plotted in Figure 9.1 together with previous heterodyne measurements and the results of recent bolometric and spectroscopic CBR measurements.

The CBR temperature at 3.3 mm is in good agreement with previous heterodyne measurements at the same wavelength, listed in Table 9.2, but has a greatly reduced uncertainty. The weighted average of the previous heterodyne measurements near 3.3 mm is $T_{CBR} = 2.55 \pm 0.19$ K; the most precise of the individual measurements, performed by Millea *et al.* (1971), yields a value of 2.61 ± 0.25 K for T_{CBR}. The 3.3-mm result is also consistent with the weighted mean of previous heterodyne measurements at all wavelengths, $T_{CBR} = 2.74 \pm 0.09$ (Smoot *et al.* 1985).

Woody and Richards (1979, 1981), measured CBR temperatures of $3.28^{+0.29}_{-0.23}$ K at 4.20 mm and $3.09^{+0.20}_{-0.14}$ K at 2.94 mm with a balloon-borne cryogenic Fourier spectrometer. Their values disagree with the 2.57 ± 0.12 K result reported here by over 2.7σ.

On the other hand, more recent measurements by Peterson, Richards, and Timusk (1985) provide better agreement with groundbased values. This experiment used a balloon-borne cryogenic multichannel bolometer to measure the CBR temperature. A value of 2.80 ± 0.16 K was obtained in the wavelength range from 2.95 to 4.35 mm.

Spectroscopic measurements of CN molecules in the directions of ζ Ophiuchi, ζ Persei, and o Persei by Meyer and Jura (1985) have yielded excitation temperatures of 2.72 to 2.79 K at 2.64 mm and 2.72 to 2.80 K at 1.32 mm. These values represent upper limits on the CBR temperature, since local mechanisms such as collisional excitation and photoexcitation by nearby sources can induce transitions in the CN molecule. Thaddeus (1972), in a discussion of possible local excitation mechanisms, concludes that only collisional excitation by electrons is likely to play a significant role. When Meyer and Jura correct for collisional excitation, they derive CBR temperatures of 2.70 ± 0.04 K at 2.64 mm and 2.76 ± 0.20 K at 1.32 mm, in good agreement with the 3.3-mm result.

Measurements of the CBR anisotropy at two or more wavelengths can also be used to derive the temperature of the (assumed) blackbody distribution. Epstein (1983) has used anisotropy measurements at 3.3 mm and at 1.22 cm (Fixen *et al.* 1983) to set a lower limit of 2.2 K on the temperature of the CBR in that wavelength range. This relatively nonrestrictive limit does not conflict with the 3.3-mm result reported here.

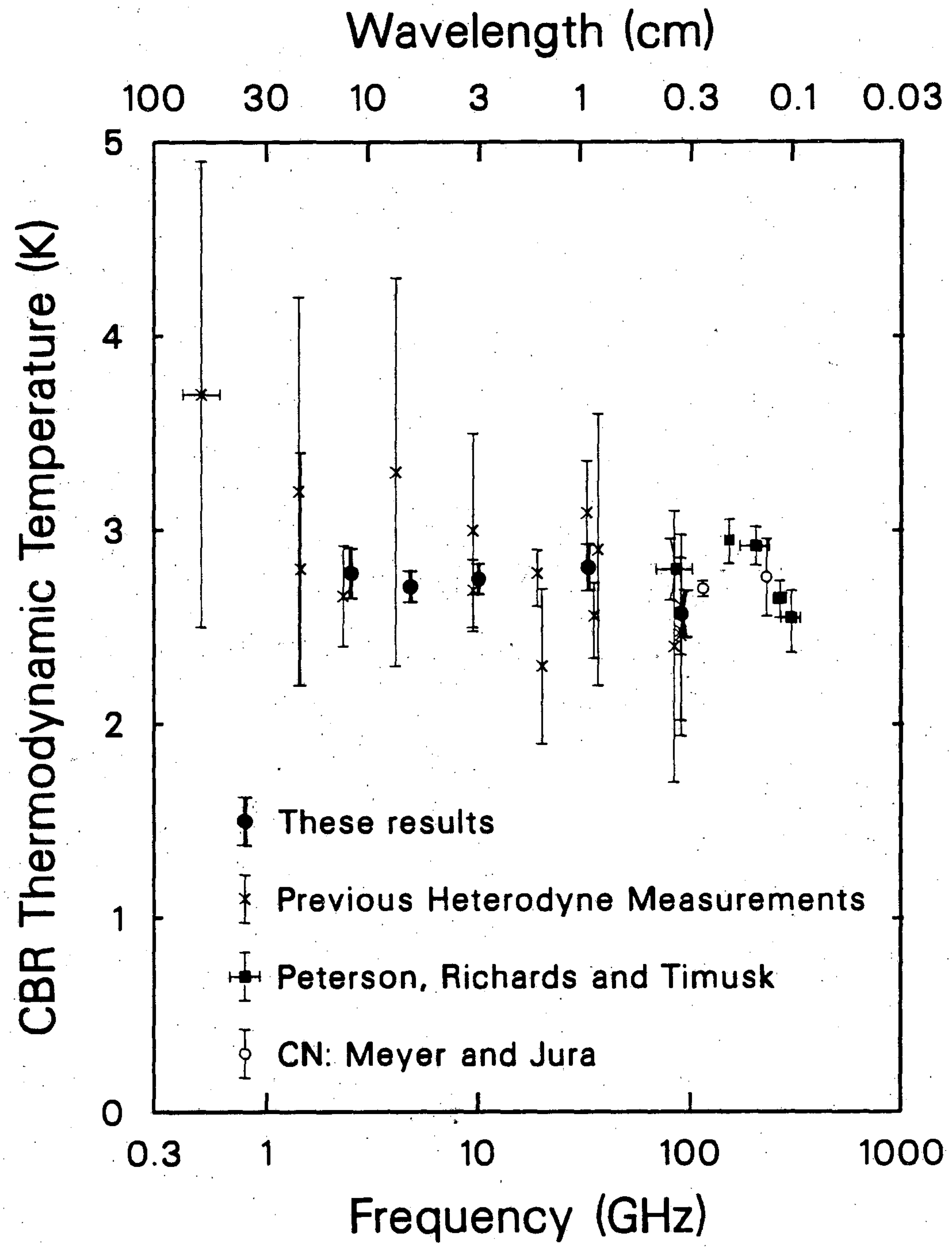

Figure 9.1: Plot of our results together with other measurements of the thermodynamic temperature of the cosmic background radiation

With the sole exception of the Woody and Richards result, all the CBR temperature measurements at wavelengths near 3 mm are compatible with a thermodynamic temperature between about 2.7 and 2.8 K, as is the weighted mean of the measurements from this project at longer wavelengths. The anomalously high and wavelength-dependent temperatures measured by Woody and Richards strongly suggest that some still-undetermined error in the gain calibration of the instrument resulted in systematic overestimates of the measured flux.

9.3 Interpretation

9.3.1 Models for Possible Distortions

Distortions in the CBR spectrum can occur if the matter (particularly the free electrons) and the radiation are out of equilibrium in such a way that there is a net transfer of energy from one to the other, and if photon-producing processes are unable to regenerate a blackbody spectrum. Most mechanisms that could give rise to observable distortions involve energy transfer from the matter to the radiation. The transferred energy can be either thermal, if the matter is heated by some means, or kinetic, if turbulence or bulk motion in the matter is radiatively damped.

The form of the distortion depends on when and how energy was added to the radiation field. Energy injected at very early times ($z \gtrsim z_T$) is efficiently transformed into new photons by thermal bremsstrahlung and radiative Compton scattering (Danese and De Zotti 1982), resulting in a blackbody spectrum with an increased temperature and no measurable distortion. If energy is transferred from the matter to the radiation field at a redshift smaller than $\sim z_T$, the spectrum of the radiation is distorted by a combination of bremsstrahlung, which generates new photons but only at low frequencies, and Compton scattering, which causes energetic electrons to give up some of their energy to photons in the radiation field, increasing the average energy per photon but leaving the photon density unchanged (Sunyaev and Zel'dovich 1970).

It is convenient to express spectral distortions in terms of the Planckian brightness temperature T_B, defined as

$$T_B(T_\nu) = \frac{T_\nu}{\ln(1 + T_\nu/T_A)},$$

or

$$T_B(x) = \frac{xT}{\ln[1 + 1/\eta(x)]}$$

where T is the radiation temperature, $x \equiv h\nu/kT$ is the dimensionless, redshift-independent frequency, and $\eta(x)$ is the photon occupation number [e.g. for a blackbody spectrum, $\eta(x) = (e^x - 1)^{-1}$, $T_B(x) = T$].

At $z < z_T$, Compton scattering provides the primary means of energy transfer between the matter and the radiation field. The rate at which a photon can gain energy through Compton scattering is given by the parameter $\alpha_0(z)$, defined here as

$$\alpha_0(z) = \frac{kT_e(z)}{m_e c^2}\sigma_T n_e(z) c$$

where $T_e(z)$ is the electron temperature at redshift z, $n_e(z)$ is the electron density at z, and σ_T is the Thompson-scattering cross-section. Note that α_0 is simply the product of the ratio of electron kinetic energy to rest mass (which determines how efficiently Compton scattering transfers energy) and the rate at which the photon undergoes Compton scatterings.

The integral of α_0 with respect to time is a measure of the the fractional change in photon energy caused by Compton scattering between some initial time t and the present. This integral, denoted y, is defined as

$$\begin{aligned} y(z) &= -\int_0^{t(z)} \alpha_0 dt \\ &= -\int_0^{z(t)} \alpha_0(z)\frac{dt}{dz}dz \end{aligned}$$

(Zel'dovich and Sunyaev 1969). The value of y is unity at a redshift z_a, which has a value of approximately $3.8 \times 10^4 \hat{\Omega}^{-1/2}$ where $\hat{\Omega} = \Omega(H_0/50)^2$, Ω is the critical density, and H_0 is the Hubble parameter in km/sec/Mpc (Danese and De Zotti 1980). If energy injection occurs at a redshift $z_h \gtrsim z_a$, Compton scattering causes the spectrum to approach a Bose-Einstein distribution with a non-zero chemical potential μ.

Energy injection at redshifts between z_a and z_T gives rise to a blackbody spectrum at long wavelengths (due to bremsstrahlung), a Bose-Einstein spectrum at short wavelengths (due to Compton scattering), and a transition region in between. At the redshift z_a, the photon occupation number η and the brightness temperature $T_B(x)$ are

$$\eta(x) = \frac{1}{\exp[x + \mu(x)] - 1} \tag{9.1}$$

and

$$T_B(x) = T\frac{x}{x + \mu(x)} .$$

The frequency-dependent chemical potential $\mu(x)$ is approximated by the equation

$$\mu(x) = \mu_0 \exp(-2x_1/x) ,$$

where μ_0 is the chemical potential in the Bose-Einstein regime and x_1 is the frequency characterizing the transition from a blackbody to a Bose-Einstein spectrum (Sunyaev and Zel'dovich 1970; Danese and De Zotti 1980). The Bose-Einstein chemical potential μ_0 is proportional to the ratio of the injected energy to the energy previously present in the radiation field:

$$\mu_0 \simeq 1.4\frac{\delta U}{U_0} \tag{9.2}$$

where U_0 is the energy density of the unperturbed radiation field and δU is the energy added to the radiation field (Chan and Jones 1975). The transition frequency x_1 is the minimum frequency at which Compton scattering can efficiently shift bremsstrahlung photons to higher frequencies, computed at the redshift z_a (Jones 1980). The brightness temperature $T_B(x)$ goes through a minimum at $x = 2x_1$. At $x << x_0$ and $x >> \mu_0$, T_B asymptotically approaches T.

The spectrum continues to evolve after z_a, even though Compton scattering can no longer alter it substantially. Danese and De Zotti (1980) have pointed out that bremsstrahlung produces photons in the transition region which partially fill in the hole created by Compton scattering. The expression they derive to account for alterations in η is

$$\eta(x) = e^{-y_B(x)}\overline{\eta} + \frac{1 - e^{-y_B(x)}}{e^x - 1} , \tag{9.3}$$

where $\overline{\eta}$ is the photon occupation number at z_a, derived in equation (9.1), and $y_B(x)$ is the optical depth for free-free absorption looking back to the redshift z_B ($\simeq 1.2 \times 10^4 \hat{\Omega}^{1/2}$), the latest epoch when Compton scattering could effectively remove photons from the transition region. The two terms in equation (9.3) represent the attenuation of the initial spectrum by free-free absorption and the production of bremsstrahlung photons; their main effects are to increase the frequency of the minimum in T_B by a factor of about 2.5 and to reduce the maximum distortion by about a factor of 1.5 (Danese and De Zotti 1978).

If energy injection occurs at a redshift z_h smaller than z_a, Compton scattering may still affect the radiation spectrum even though it cannot establish a Bose-Einstein distribution. The Compton-distorted spectrum is given by the equation (Danese and De Zotti 1978)

$$\bar{\eta}(x,u) \simeq (e^x - 1)^{-1}\left[1 + u\frac{xe^x}{e^x - 1}\left(\frac{x}{\tanh(x/2)} - 4\right)\right] , \tag{9.4}$$

where u is defined by the equation:

$$u = -\int_0^{z_h} \alpha_0(z)\frac{T_e - T_R}{T_R}\frac{dt}{dz}dz ,$$

T_e and T_R being respectively the electron and radiation temperatures (Illarionov and Sunyaev 1974). The value of u is determined by $\delta U/U_0$, the fractional energy added to the CBR:

$$\begin{aligned} \frac{\delta U}{U_0} &= e^{4u} - 1 \\ &\approx 4u \qquad (u << 1) \end{aligned} \tag{9.5}$$

(Sunyaev and Zel'dovich 1980). Compton scattering has the effect of depressing T_B by an amount $2uT_R$ at frequencies $x < 1$ and sharply enhancing it beyond.

Equation (9.4) does not include the effects of bremsstrahlung. At frequencies below $x_B(z_h)$, the universe becomes opaque to free-free absorption and T_B rises from $T_R(1-2u)$ to T_e. The value of $x_B(z_h)$ lies between 5×10^{-2} and 5×10^{-4}, depending upon z_h and $\hat{\Omega}$. Zel'dovich *et al.* (1972) have shown that the amount of the temperature rise is

$$\Delta T = 7.4\,T_R u .$$

When bremsstrahlung is included in the calculation of η, the resulting equation has a form similar to that of equation (9.3):

$$\eta = e^{-y_B(x_e)}\bar{\eta} + \frac{1 - e^{-y_B(x_e)}}{e^{x_e} - 1} , \tag{9.6}$$

but $\bar{\eta}$ now comes from equation (9.4) rather than equation (9.1), and the electron temperature T_e is explicitly used to calculate x_e.

9.3.2 Fits to Observations

Measurements at longer wavelengths confirm the trend in the results near 3 mm. The weighted mean of our measurements at the four longer wavelengths is

$$T_{CBR} = 2.75 \pm 0.05 \text{ K}.$$

The weighted average of previous results at wavelengths longward of 3 mm is

$$T_{CBR} = 2.75 \pm 0.09 \text{ K}.$$

The combined results of past and present measurements (Table 9.3) yield a CBR temperature of 2.72 ± 0.02 K and fit a blackbody spectrum with a χ^2 of 18.7 for 27 degrees of freedom.

As well as checking the results for overall consistency with a blackbody spectrum, one can also analyze the measurements for possible distortions. If our measurements are fitted to a

References	Wavelength (cm)	ν (GHz)	T_{CBR} (K)
Howell & Shakeshaft 1967	73.5	0.41	3.7 ± 1.2
	49.2	0.61	
Penzias & Wilson 1967	49.2	1.415	3.2 ± 1.0
Howell & Shakeshaft 1966	20.7	1.45	2.8 ± 0.6
Otoshi & Stelzreid 1975	13.05	2.30	2.66 ± 0.26
Smoot *et al.* 1985	12.0	2.5	2.78 ± 0.13
Penzias & Wilson 1965	7.35	4.08	3.3 ± 1.0
Smoot *et al.* 1985	6.3	4.75	2.71 ± 0.08
Roll & Wilkinson 1966	3.2	9.38	3.0 ± 0.5
Stokes *et al.* 1967	3.2	9.38	$2.69^{+0.16}_{-0.21}$
Smoot *et al.* 1985	3.0	10.0	2.75 ± 0.08
Stokes *et al.* 1967	1.58	19.0	$2.78^{+0.12}_{-0.17}$
Welch 1984	1.50	20.0	2.3 ± 0.4
Ewing *et al.* 1967	0.924	32.5	3.09 ± 0.26
De Amici *et al.* 1985	0.909	33.0	2.81 ± 0.12
Wilkinson 1967	0.856	35.05	$2.56^{+0.14}_{-0.22}$
Puzanov *et al.* 1968	0.82	36.6	2.9 ± 0.7
Kislyakov *et al.* 1971	0.358	83.8	2.4 ± 0.7
Boynton *et al.* 1968	0.333	90.0	$2.46^{+0.40}_{-0.44}$
Millea *et al.* 1971	0.33	90.4	2.61 ± 0.25
Boynton & Stokes 1974	0.333	90.0	$2.48^{+0.50}_{-0.55}$
This work	0.333	90.0	2.57 ± 0.12
Meyer & Jura 1985	0.264	113.6	2.70 ± 0.04
	0.132	227.3	2.76 ± 0.20
Peterson *et al.* 1985	0.351	85.5	2.80 ± 0.16
	0.198	151.5	$2.95^{+0.11}_{-0.12}$
	0.148	203	2.92 ± 0.10
	0.114	264	$2.65^{+0.09}_{-0.10}$
	0.100	299	$2.55^{+0.14}_{-0.18}$

Table 9.3: Measurements of the Cosmic Background Radiation Temperature

$\hat{\Omega}$	z_h	T_R (K)	u	χ^2
1.0	4×10^4 (z_a)	2.72 ± 0.02	$(+0.4 \pm 3.3) \times 10^{-3}$	18.7
	1×10^4	2.73 ± 0.03	$(+0.9 \pm 4.2) \times 10^{-3}$	18.7
	4×10^3	2.73 ± 0.03	$(+0.5 \pm 6.2) \times 10^{-3}$	18.7
	1×10^3	2.70 ± 0.04	$(-0.6 \pm 1.0) \times 10^{-2}$	18.3
0.1	1×10^5 (z_a)	2.71 ± 0.04	$(-0.3 \pm 1.0) \times 10^{-2}$	18.5
	4×10^4	2.71 ± 0.04	$(-0.3 \pm 1.0) \times 10^{-2}$	18.5
	1×10^4	2.71 ± 0.04	$(-0.4 \pm 1.0) \times 10^{-2}$	18.4
	4×10^3	2.71 ± 0.04	$(-0.5 \pm 1.0) \times 10^{-2}$	18.4
	1×10^3	2.70 ± 0.04	$(-0.6 \pm 1.0) \times 10^{-2}$	18.3
0.01	4×10^5 (z_a)	2.70 ± 0.04	$(-0.6 \pm 1.0) \times 10^{-2}$	18.3
	1×10^5	2.70 ± 0.04	$(-0.6 \pm 1.0) \times 10^{-2}$	18.3
	4×10^4	2.70 ± 0.04	$(-0.6 \pm 1.0) \times 10^{-2}$	18.3
	1×10^4	2.70 ± 0.04	$(-0.6 \pm 1.0) \times 10^{-2}$	18.3
	4×10^3	2.70 ± 0.04	$(-0.6 \pm 1.0) \times 10^{-2}$	18.3
	1×10^3	2.70 ± 0.04	$(-0.6 \pm 1.0) \times 10^{-2}$	18.3

Table 9.4: Best-fit values of T_R and u from all measurements. The quoted errors are 68% confidence levels. The χ^2 is computed for 26 degrees of freedom.

spectrum of the form given by equation (9.1) with bremsstrahlung corrections given by equation (9.3), the best-fit values of T and μ_0 are:

$$\begin{array}{llll} \hat{\Omega} = 1.0 & T = 2.69 \pm 0.10 \text{ K} & \mu_0 = (-3.6 \pm 9.9) \times 10^{-3} & \chi^2 = 2.4 \\ \hat{\Omega} = 0.1 & T = 2.70 \pm 0.07 \text{ K} & \mu_0 = (-1.5 \pm 2.9) \times 10^{-3} & \chi^2 = 2.3 \\ \hat{\Omega} = 0.01 & T = 2.70 \pm 0.07 \text{ K} & \mu_0 = (-1.2 \pm 2.4) \times 10^{-3} & \chi^2 = 2.3 \end{array}$$

for 3 degrees of freedom. When all the CBR measurements in Table 9.3 are used for the calculation, the resulting values are:

$$\begin{array}{llll} \hat{\Omega} = 1.0 & T = 2.72 \pm 0.03 \text{ K} & \mu_0 = (-1.6 \pm 5.7) \times 10^{-3} & \chi^2 = 18.6 \\ \hat{\Omega} = 0.1 & T = 2.72 \pm 0.03 \text{ K} & \mu_0 = (-0.8 \pm 1.8) \times 10^{-3} & \chi^2 = 18.5 \\ \hat{\Omega} = 0.01 & T = 2.71 \pm 0.03 \text{ K} & \mu_0 = (-1.0 \pm 1.4) \times 10^{-3} & \chi^2 = 18.3 \end{array}$$

for 26 degrees of freedom.

Equations (9.4) and (9.6) can be used to derive best-fit values of T_R and u. Because the value of z_h affects the contribution of bremsstrahlung to the low-frequency portion of the spectrum, z_h and $\hat{\Omega}$ must both be specified for the model fit. Table 9.4 lists the best-fit values of T_R and u over a range of redshifts and densities. The values are derived from all the measurements in Table 9.3. The best-fit values of u are consistent with zero at the 1σ level.

9.3.3 Impact on CBR-Production Models

The measured values of μ_0, which are all consistent with zero, can be used in conjunction with equation (9.2) to set upper limits on the energy transferred to the radiation field at redshifts between z_a and z_T. The complete data set yields the 1σ limits:

$$\begin{aligned} \hat{\Omega} &= 1.0 & \tfrac{\delta U}{U_0} &\leq 2.9 \times 10^{-3} \\ \hat{\Omega} &= 0.1 & \tfrac{\delta U}{U_0} &\leq 7.1 \times 10^{-4} \\ \hat{\Omega} &= 0.01 & \tfrac{\delta U}{U_0} &\leq 2.9 \times 10^{-4}\,. \end{aligned}$$

Similarly, equation (9.5) and the measured upper limits on u restrict the energy release that could have occurred at more recent times. The 1σ limit on u, which varies from 4×10^{-3} to 7×10^{-3} depending on the density parameter and the redshift of energy release, sets an upper limit of approximately 3% on the fractional energy transferred to the CBR at redshifts less than z_a.

Upper limits on $\delta U/U_0$ derived from μ_0 and u are summarized in Figure 9.2. Some care must be taken in applying these limits to astrophysical processes, since the energy generated by these processes may not be readily transferred to the CBR. The tight coupling between matter and photons before recombination means that energy liberated during that epoch in the form of photons or energetic charged particles is quickly taken up by the CBR. Limits on CBR distortions therefore yield direct upper bounds on the energy-liberating processes that occur between z_T and recombination, provided the energy is liberated in a form that could couple to the ionized matter (i.e. *not* neutrinos or other non-interacting particles). These can be used to derive limits on: 1. the spectrum of adiabatic density perturbations at $z_a < z < z_T$ (Sunyaev and Zel'dovich 1970), 2. the spectrum of turbulence and vorticity at $z_a < z < z_T$ (Sunyaev and Zel'dovich 1970; Chan and Jones 1976), 3. residual antimatter in the early universe (Stecker and Puget 1972; Sunyaev and Zel'dovich 1970), and 4. energy release by evaporating primordial black holes or unstable exotic particles at $z_a < z < z_T$ (Dolgov and Zel'dovich 1981; Silk and Stebbins 1983).

The situation after recombination is not so simple. Because the unionized matter interacts only very weakly with the radiation, the kinetic energy of its bulk motion does not result in distortions in the CBR spectrum. On the other hand, any significant release of thermal energy by the matter would ionize it once again. If the matter is not strongly clumped, the reionized medium interacts with the radiation as before. At redshifts greater than ~ 8, the timescale on which the matter is cooled by Compton scattering is shorter than the expansion time of the universe (Sunyaev and Zel'dovich 1980), so most of the excess thermal energy is taken up by CBR photons, causing a distortion. In this case, the observational bounds on u limit the thermal energy released between $z \simeq 8$ and $z \simeq 1500$ to less than 3% of the energy in the CBR.

This analysis breaks down if a large fraction of the matter in the universe is highly clumped or bound up in an early generation of stars. In that case, Compton scattering may not be able to transfer the heat efficiently from the matter to the CBR. The form and extent of the resulting distortions depend on the details of the model. One such class of models—the hypothesis that some or all of the CBR is thermal radiation from warm dust produced by Population III stars at $z \gtrsim 10$—has been suggested by Rees (1978), Negroponte *et al.* (1981), Wright (1982), and others to explain the spectral distortion apparently observed by Woody and Richards and to promote galaxy formation. Although the details of such models have to some extent been tailored to fit the Woody-Richards distortion, significant departures from a blackbody curve are almost inevitable because of the spectral characteristics of the carbon or silicate materials that make up the grains. The absence of significant distortions in recent measurements of the CBR spectrum is a heavy blow against such theories: To devise a plausible dust-emission model that gives a flat spectrum over a hundredfold range in wavelength may well prove an impossible task.

9.4 Conclusions

This set of measurements has yielded scientific results that are significant both in them-

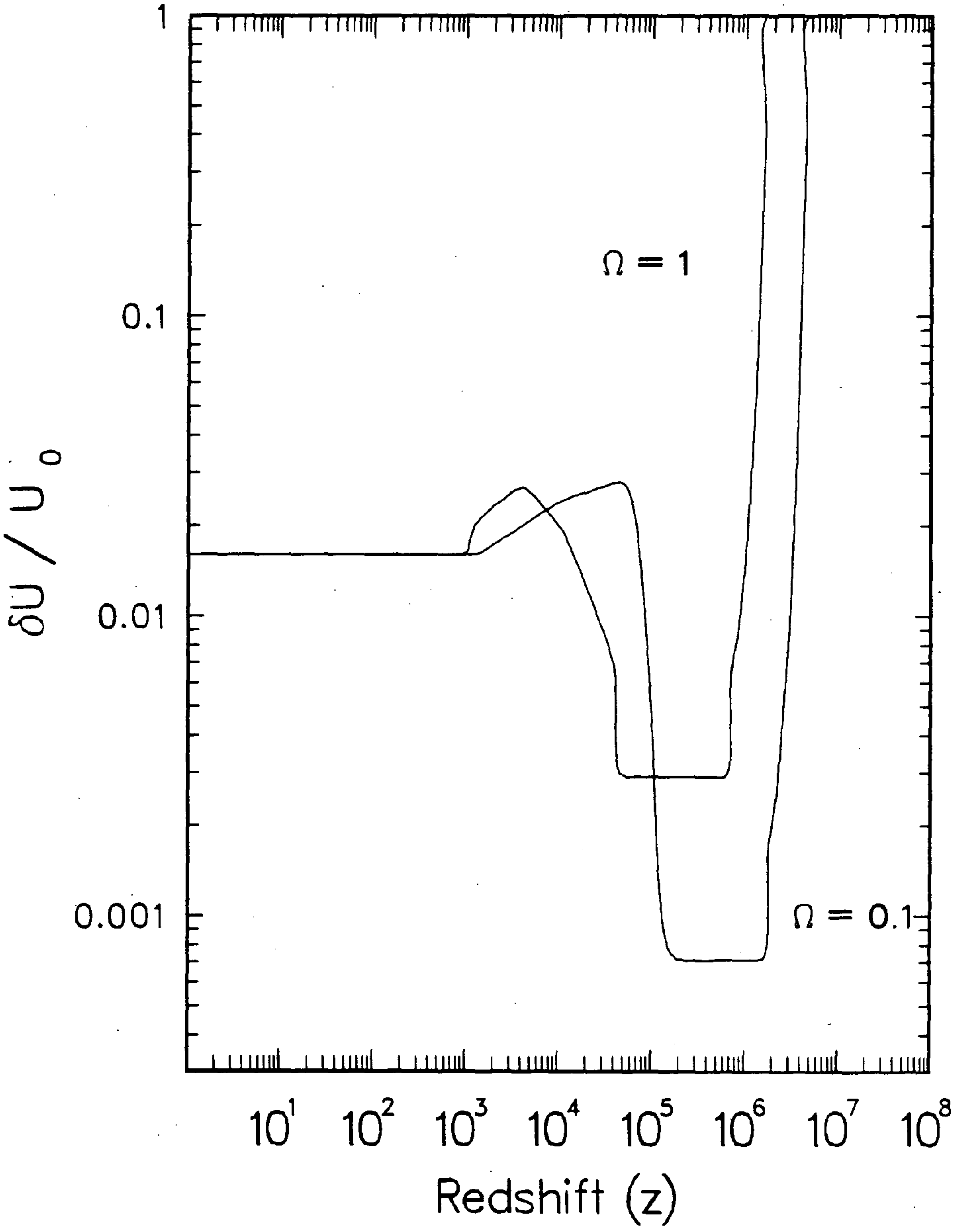

Figure 9.2: Limits on the fractional energy added to the CBR as a function of z_h.

selves and in conjunction with measurements at other wavelengths. The accurate measurement of T_{CBR} with a ground-based radiometer is a useful cross-check on the CBR temperatures obtained from balloon-borne radiometric measurements and spectroscopic observations of interstellar CN molecules. As part of a coordinated program to measure the CBR temperature over a range of wavelengths with a minimum of wavelength-dependent systematic error, these measurements have helped to establish the spectrum of the CBR near the peak and into the Rayleigh-Jeans region. Finally, the simultaneous measurements of atmospheric emission at multiple wavelengths has provided useful information about the microwave emission spectra of atmospheric oxygen (O_2) and water vapor.

The recent measurements by ourselves, by Meyer and Jura, and by Peterson *et al.* indicate that the CBR spectrum is quite well fit by a blackbody spectrum with a temperature of 2.72 ± 0.02. There is no evidence for distortions due to energy injection either before or after z_a, and there is no indication of a distortion of the Woody-Richards type.

The fact that the estimated error in the 3.3-mm measurement is actually 20% smaller than the error in the result by Peterson *et al.* in the same wavelength range indicates that ground-based heterodyne radiometry remains a viable technique for CBR measurements even at such short wavelengths. However, it is clear from the error budgets in Tables 8.2 and 8.3 that the measurement uncertainty would be considerably reduced if the measurement could be performed from an airborne or spaceborne platform. Furthermore, the $\gtrsim$9 K background subtraction required for the analysis of a ground-based measurement introduces a risk that unanticipated errors in the atmospheric subtraction could increase the true measurement error well beyond the estimated value.

For these reasons, the next generation of heterodyne measurements of the CBR temperature at 3 mm might well be made from an airplane or a balloon. Both types of platform have their advantages and their drawbacks: an airplane is more controllable and in many ways more convenient than a balloon, but at airplane altitudes the atmosphere still contributes enough radiation to T_{Zenith} so that zenith scans would probably be necessary. Either type of platform would require an automated radiometer system, a definite complication compared to the ground-based system. If such a system could be made to work, its narrow and well-defined bandwidth and its potential for accuracy would nicely complement the characteristics of bolometric and spectroscopic CBR measurements.

Appendix A

Atmospheric Model

The atmosphere is a warm, partially absorbing medium through which the radiometer must look to see the universe beyond. As such, the atmosphere absorbs a fraction of the incoming radiation and emits radiation of its own. A model of the atmosphere's radiometric properties should be realistic enough to allow one to derive accurate values of $T_{A,atm}$ from zenith scans. To understand the properties that must be modeled, consider the atmosphere first as a planar slab with a constant temperature, and let the antenna have a delta-function gain pattern. The emission from the atmosphere at a zenith angle Z is roughly equal to the product of its mean temperature ($\sim$ 250 K), its zenith opacity ($\sim$ 0.04 at 3800 m on a clear day), and the ratio of the air mass at Z to the zenith air mass [$\approx \sec(Z)$].

This crude estimate serves as a good conceptual model, but it neglects several factors, the most important of which are atmospheric self-absorption ($\sim$ 0.5 K) and the effect of beam spread in the actual antenna. The model also neglects the curvature of the atmosphere and the fact that the temperature and emissivity of the atmosphere are both altitude-dependent. To derive a detailed model of the atmospheric antenna temperature as a function of zenith angle, let us retain the delta-function antenna for the moment. When pointed at a zenith angle Z, the antenna receives radiation at an antenna temperature $T_{Sky}(Z)$ which is made up primarily of thermal radiation from the atmosphere and the CBR itself. As Z increases, atmosphere emission increases while atmospheric attenuation causes the contribution from the CBR to diminish. In general, the presence of clouds and similar phenomena makes T_{Sky} a function of azimuth as well as zenith angle, but under good observing conditions these variations are generally small compared to the dependence on Z.

The value of $T_{Sky}(Z)$ can in principle be computed from the equation:

$$T_{Sky}(Z) = \int_0^\infty T(h)e^{-\tau(h,Z)}\kappa(h)f(h,Z)dh + T_{A,CBR}e^{-\tau(\infty,Z)} \qquad (A.1)$$

where h is the height above the ground, $T(h)$ is the ambient temperature at height h, $f(h,Z)$ is the derivative of column length with respect to height [$\sec(Z)$ in the planar-slab model], $\kappa(h)$ is the specific absorption coefficient of the atmosphere at h, and $\tau(h,Z)$ is the opacity of the atmosphere between height h and the ground at a zenith angle Z:

$$\tau(h,Z) = \int_0^h \kappa(h)f(h,Z)dh\,. \qquad (A.2)$$

Since $\tau(h,Z) << 1$ for all values of Z that are relevant to the model, the exponential terms in equation (A.1) can be expanded in a Taylor series:

$$T_{Sky}(Z) \simeq \int_0^\infty T(h)\kappa(h)f(h,Z)\left[1-\tau(h,Z)+\frac{\tau(h,Z)^2}{2}\right]dh \\ + T_{A,CBR}\left[1-\tau(\infty,Z)+\frac{\tau(\infty,Z)^2}{2}-\frac{\tau(\infty,Z)^3}{6}\right]. \qquad (A.3)$$

Because $\tau(h,Z) \lesssim 5 \times 10^{-2}\sec(Z)$, terms of order $\kappa\tau^3$ and τ^4 have been neglected. This approximation introduces an error of less than 2 mK in $T_{A,atm}$.

To proceed with the model, we must know the height dependence of $\tau(h,Z)$ and $\kappa(h)$. The absorption coefficient is the sum of the coefficients for pressure-broadened lines of oxygen (κ_{O_2}) and water vapor (κ_{H_2O}). Because the lines are pressure broadened, the coefficients are proportional to the ambient pressure as well as to the density of the molecular species. From equations (5.20) and (5.22) of Ulaby *et al.* (1981), one can easily show that

$$\kappa_{H_2O}(h) \sim P(h)\,\rho_{H_2O}(h)\,T(h)^{-2.1},$$

$P(h)$ being the ambient pressure at h and $\rho_{H_2O}(h)$ being the density of water vapor. From equations (5.33) through (5.38) of the same work, one can also show that $\kappa_{O_2}(h)$ has the form:

$$\kappa_{O_2}(h) \sim P(h)^2\,T(h)^{-2.9} \sim P(h)\,\rho_{O_2}(h)\,T(h)^{-1.9}.$$

Thus, both $\kappa_{H_2O}(h)$ and $\kappa_{O_2}(h)$ scale with height approximately as $P(h)\rho(h)T(h)^{-2}$.

The pressure varies nearly exponentially with altitude and has a 7.7-km scale height. The density variation is also approximately exponential; the density scale height for water vapor is 2.2 km while that of oxygen is 9.5 km. (All three scale heights are taken from Ulaby *et al.* [1981].) The scale height for the products $[P(h)\rho_{H_2O}(h)]$ and $[P(h)\rho_{O_2}(h)]$ are therefore 1.7 km and 4.2 km respectively. The relative contributions from oxygen and water are unknown and variable, so the model assumes that $\kappa(h)$ has an effective scale height h_0 with a value between 1.7 and 4.2 km.

The absorption coefficient can thus be modeled as:

$$\kappa(h) \simeq \frac{\tau_0}{\int_0^\infty \left[e^{-h/h_0}/T(h)^2\right]dh}\,\frac{e^{-h/h_0}}{T(h)^2} \\ = \frac{\tau_0}{I_1(\infty,h_0)}\,\frac{e^{-h/h_0}}{T(h)^2}, \qquad (A.4)$$

where τ_0 is the zenith opacity and the integral $I_1(h,h_0)$ is defined by the equation:

$$I_1(h,h_0) \equiv \int_0^h \frac{e^{-h/h_0}}{T(h)^2}dh.$$

The temperature profile used in the atmospheric model is the formula:

$$\begin{aligned} T(h) &= 280 - 6.5h && h \le 9 \\ T(h) &= 222 && 9 < h < 21 \\ T(h) &= 177 + 2.1h && h \ge 21. \end{aligned}$$

The temperature is in Kelvins, and the height h is in kilometers above the ground. The formula is based on the tabulation of the 1962 U. S. Standard Atmosphere (Cole *et al.* 1965) in Chapter 5 of Ulaby *et al.* (1981). The formula has been modified to allow for the fact that the ambient temperature at ground level during our measurements (about 280 K) was 17 K warmer than the temperature of the 1962 Standard Atmosphere at the same elevation.

To determine $\tau(h,Z)$ from equation (A.2), one must know the value of $f(h,Z)$. It is easily shown that for a spherical geometry,

$$f(h,Z)=\frac{1+h/R_0}{[\cos^2(Z)+2h/R_0+(h/R_0)^2]^{1/2}} \; ,$$

R_0 being the radius of the earth. The characteristic value of h is the scale height h_0 which is small compared to R_0, so terms of order $(h/R_0)^2$ may be neglected and the equation may be written in the simpler form:

$$\begin{aligned} f(h,Z) &\simeq \sec(Z)-(h/R_0)\sec(Z)\tan^2(Z) \\ &= f_1(Z)-(h/R_0)f_2(Z) \end{aligned} \tag{A.5}$$

where

$$f_1(Z)=\sec(Z)$$

and

$$f_2(Z)=\sec(Z)\tan^2(Z) \; .$$

Equations (A.2) and (A.5) can be combined to give

$$\tau(h,Z)\simeq f_1(Z)\int_0^h \kappa(h)dh - f_2(Z)\int_0^h \frac{h}{R_0}\kappa(h)dh \, . \tag{A.6}$$

If $I_2(h,h_0)$ is defined as

$$I_2(h,h_0)\equiv\int_0^h \frac{he^{-h/h_0}}{R_0\,T(h)^2}dh \; ,$$

then from equations (A.4) and (A.6), $\tau(h,Z)$ can be written:

$$\tau(h,Z)\simeq\frac{\tau_0}{I_1(\infty,h_0)}[f_1(Z)I_1(h,h_0)-f_2(Z)I_2(h,h_0)] \, . \tag{A.7}$$

Equations (A.4), (A.5), and (A.7) can be substituted into equation (A.3) to yield an expression for $T_{Sky}(Z)$. If one neglects terms of order $(h/R_0)\tau_0{}^2$ and $(h/R_0)\tau_0{}^3$, which contribute less than 1 mK to the final value of $T_{A,atm}$, the resulting expression is

$$\begin{aligned} T_{Sky}(Z) \simeq\ & \tau_0\int_0^\infty \frac{e^{-h/h_0}}{I_1(\infty,h_0)\,T(h)}[f_1(Z)-(h/R_0)f_2(Z)]\,dh \\ & -\tau_0{}^2\int_0^\infty \frac{e^{-h/h_0}I_1(h,h_0)}{I_1(\infty,h_0)^2\,T(h)}f_1(Z)^2\,dh + \tau_0{}^3\int_0^\infty \frac{e^{-h/h_0}I_1(h,h_0)^2}{2I_1(\infty,h_0)^3\,T(h)}f_1(Z)^3\,dh \\ & + T_{A,CBR}\left\{1-\tau_0\left[f_1(Z)-f_2(Z)\frac{I_2(\infty,h_0)}{I_1(\infty,h_0)}\right]+\frac{\tau_0{}^2}{2}f_1(Z)^2-\frac{\tau_0{}^3}{6}f_1(Z)^3\right\} \, . \end{aligned} \tag{A.8}$$

If one groups the terms in equation (A.8) according to their powers of τ_0, one obtains:

$$\begin{aligned}
T_{Sky}(Z) \simeq T_{A,CBR} + \tau_0 \Bigg\{ \Bigg[\Bigg[\int_0^\infty \frac{e^{-h/h_0}}{I_1(\infty,h_0)\,T(h)}\,dh - T_{A,CBR}\Bigg] f_1(Z) \\
- \Bigg[\int_0^\infty \frac{e^{-h/h_0}}{I_1(\infty,h_0)\,T(h)}(h/R_0)\,dh - \frac{I_2(\infty,h_0)}{I_1(\infty,h_0)} T_{A,CBR}\Bigg] f_2(Z) \Bigg\} \\
- \frac{\tau_0{}^2}{2}\Bigg[2\int_0^\infty \frac{e^{-h/h_0} I_1(h,h_0)}{I_1(\infty,h_0)^2\,T(h)}\,dh - T_{A,CBR}\Bigg] f_1(Z)^2 \\
+ \frac{\tau_0{}^3}{6}\Bigg[3\int_0^\infty \frac{e^{-h/h_0} I_1(h,h_0)^2}{I_1(\infty,h_0)^3\,T(h)}\,dh - T_{A,CBR}\Bigg] f_1(Z)^3 \\
= T_{A,CBR} + [T_{11} f_1(Z) - T_{12} f_2(Z)]\tau_0 - T_2 f_1(Z)^2 \frac{\tau_0{}^2}{2} + T_3 f_1(Z)^3 \frac{\tau_0{}^3}{6} ,
\end{aligned}$$

where the temperature T_{11} is the first term enclosed by square brackets, T_{12} is the second, T_2 the third, and T_3 the fourth. The four temperature terms are independent of Z and τ_0. Once calculated, they can be used to determine the value of $T_{Sky}(Z)$ for any Z and τ_0 consistent with the assumptions of the model.

So far, the model has been developed with the assumption of an infinitesimally narrow antenna gain pattern. One can easily generalize it to allow for the effects of beam spread by convolving the normalized gain pattern of the antenna $g(\phi,\chi)$ with the functions $f_i(Z)^n$:

$$A_1(Z) = \int f_1(\psi) g(\phi,\chi)\cos(\chi)d\chi d\phi$$

$$A_2(Z) = \int f_2(\psi) g(\chi,\phi)\cos(\chi)d\chi d\phi$$

$$B(Z) = \int f_1(\psi)^2 g(\chi,\phi)\cos(\chi)d\chi d\phi$$

$$C(Z) = \int f_1(\psi)^3 g(\chi,\phi)\cos(\chi)d\chi d\phi$$

where:

Z = angle between the zenith and the antenna axis,

ψ = angle between the zenith and the integration element,

χ = angle between the antenna axis and the integration element,

ϕ = rotation angle of the integration element around the antenna axis,

and

$\cos(\psi) = \cos(Z)\cos(\chi) + \sin(Z)\sin(\chi)\cos(\phi)$.

An antenna with its axis directed toward Z sees a sky temperature:

$$T_{Sky}(Z) \simeq T_{A,CBR} + [T_{11}A_1(Z) - T_{12}A_2(Z)]\tau_0 - T_2 B(Z)\frac{\tau_0{}^2}{2} + T_3 C(Z)\frac{\tau_0{}^3}{6} .$$

Note that the equation for the radiometric sky temperature has been reduced to a third-order polynomial in τ_0. The coefficients that describe the atmospheric contribution to $T_{Sky}(Z)$ can all be calculated numerically from the atmospheric model and the gain pattern of the antenna; only τ_0 remains unknown.

Define the temperature terms $\mathcal{T}_1(Z)$ through $\mathcal{T}_3(Z)$ as:

$$\begin{aligned}\mathcal{T}_1(Z) &= T_{11}A_1(Z) - T_{12}A_2(Z)\,;\\ \mathcal{T}_2(Z) &= T_2B(Z)\,;\\ \mathcal{T}_3(Z) &= T_3C(Z)\,,\end{aligned}$$

so

$$T_{Sky}(Z) = T_{A,CBR} + \mathcal{T}_1(Z)\tau_0 - \mathcal{T}_2(Z)\frac{{\tau_0}^2}{2} + \mathcal{T}_3(Z)\frac{{\tau_0}^3}{6}\,.$$

Since the atmospheric antenna temperature $T_{A,atm}$ is just the difference between $T_{Sky}(0)$ and $T_{A,CBR}$, it follows that:

$$T_{A,atm} = \mathcal{T}_1(0)\tau_0 - \mathcal{T}_2(0)\frac{{\tau_0}^2}{2} + \mathcal{T}_3(0)\frac{{\tau_0}^3}{6}\,. \tag{A.9}$$

If T_{Sky} is measured at two zenith angles Z_1 and Z_2, the temperature difference is

$$\Delta T_{Sky}(Z_1,Z_2) \simeq \Delta\mathcal{T}_1(Z_1,Z_2)\tau_0 - \Delta\mathcal{T}_2(Z_1,Z_2)\frac{{\tau_0}^2}{2} + \Delta\mathcal{T}_3(Z_1,Z_2)\frac{{\tau_0}^3}{6}\,, \tag{A.10}$$

where $\Delta T_{Sky}(Z_1,Z_2)$ is $T_{Sky}(Z_1) - T_{Sky}(Z_2)$ and the differences $\Delta\mathcal{T}_n(Z_1,Z_2)$ are defined analogously. Let ϵ be defined as:

$$\epsilon(Z_1,Z_2) \equiv \frac{\Delta T_{Sky}(Z_1,Z_2)}{\Delta\mathcal{T}_1(Z_1,Z_2)}\,.$$

Then from equation (A.10), ϵ can be written:

$$\epsilon = \tau_0 - \frac{\Delta\mathcal{T}_2}{\Delta\mathcal{T}_1}\frac{{\tau_0}^2}{2} + \frac{\Delta\mathcal{T}_3}{\Delta\mathcal{T}_1}\frac{{\tau_0}^3}{6}\,. \tag{A.11}$$

(The Z's have been suppressed for compactness.)

The derivation of this equation has been long and tortuous. To regain sight of the physics behind it, consider once more a delta-function antenna viewing a planar-slab atmosphere at a constant temperature T_{atmos}. In this case, equation (A.11) reduces to:

$$\begin{aligned}\frac{\Delta T_{Sky}(Z_1,Z_2)}{T_{atmos} - T_{A,CBR}} &\simeq [\sec(Z_1) - \sec(Z_2)]\,\tau_0\\ &\quad - \left[\sec^2(Z_1) - \sec^2(Z_2)\right]\frac{{\tau_0}^2}{2} + \left[\sec^3(Z_1) - \sec^3(Z_2)\right]\frac{{\tau_0}^3}{6}\,,\end{aligned}$$

as one might expect.

Given equation (A.11) for $\epsilon(\tau_0)$, it is simple to derive the inverse equation:

$$\tau_0 \simeq \epsilon + \frac{1}{2}\frac{\Delta\mathcal{T}_2}{\Delta\mathcal{T}_1}\epsilon^2 + \frac{1}{2}\left[\left(\frac{\Delta\mathcal{T}_2}{\Delta\mathcal{T}_1}\right)^2 - \frac{\Delta\mathcal{T}_3}{3\Delta\mathcal{T}_1}\right]\epsilon^3\,, \tag{A.12}$$

accurate to third order in ϵ. Finally, τ_0 from equation (A.12) is substituted into equation (A.9) to yield an expression for $T_{A,atm}$ in terms of ϵ and the model-temperature terms. With the terms grouped by powers of ϵ, the equation has the form:

$$\begin{aligned}T_{A,atm} &= \mathcal{T}_1(0)\epsilon + \frac{1}{2}\left[\frac{\Delta\mathcal{T}_2}{\Delta\mathcal{T}_1}\mathcal{T}_1(0) - \mathcal{T}_2(0)\right]\epsilon^2\\ &\quad + \frac{1}{2}\left\{\frac{1}{3}\left[\mathcal{T}_3(0) - \frac{\Delta\mathcal{T}_3}{\Delta\mathcal{T}_1}\mathcal{T}_1(0)\right] + \left[\frac{\Delta\mathcal{T}_2}{\Delta\mathcal{T}_1}\mathcal{T}_1(0) - \mathcal{T}_2(0)\right]\frac{\Delta\mathcal{T}_2}{\Delta\mathcal{T}_1}\right\}\epsilon^3\,,\end{aligned}$$

or

$$\begin{aligned} T_{A,atm} &= \hat{\mathcal{T}}_{atmos,1}(Z_1, Z_2)\,\epsilon(Z_1, Z_2) \\ &\quad + \hat{\mathcal{T}}_{atmos,2}(Z_1, Z_2)\,\epsilon(Z_1, Z_2)^2 + \hat{\mathcal{T}}_{atmos,3}(Z_1, Z_2)\,\epsilon(Z_1, Z_2)^3 \,, \end{aligned} \tag{A.13}$$

where:

$$\begin{aligned} \hat{\mathcal{T}}_{atmos,1} &= \mathcal{T}_1(0) \,, \\ \hat{\mathcal{T}}_{atmos,2} &= \frac{1}{2}\left[\frac{\Delta\mathcal{T}_2}{\Delta\mathcal{T}_1}\mathcal{T}_1(0) - \mathcal{T}_2(0)\right] \,, \end{aligned}$$

and

$$\hat{\mathcal{T}}_{atmos,3} = \frac{1}{2}\left\{\frac{1}{3}\left[\mathcal{T}_3(0) - \frac{\Delta\mathcal{T}_3}{\Delta\mathcal{T}_1}\mathcal{T}_1(0)\right] + \left[\frac{\Delta\mathcal{T}_2}{\Delta\mathcal{T}_1}\mathcal{T}_1(0) - \mathcal{T}_2(0)\right]\frac{\Delta\mathcal{T}_2}{\Delta\mathcal{T}_1}\right\} .$$

If four zenith angles Z_1 through Z_4 are used to determine $T_{A,atm}$, the preceeding derivation is easily adapted. Let

$$\Delta T_{Sky} = \frac{1}{2}[T_{Sky}(Z_1) + T_{Sky}(Z_3) - T_{Sky}(Z_2) - T_{Sky}(Z_4)] \,,$$

let

$$\Delta\mathcal{T}_n = \frac{1}{2}[\mathcal{T}_n(Z_1) + \mathcal{T}_n(Z_3) - \mathcal{T}_n(Z_2) - \mathcal{T}_n(Z_4)] \,,$$

and let

$$\epsilon \equiv \frac{\Delta T_{Sky}}{\Delta\mathcal{T}_1}$$

as before. Equations (A.11) through (A.13) remain valid and can be used to derive $T_{A,atm}$ from ϵ.

Appendix B

Components Used in the Radiometer Front End

Component	**Manufacturer and Model**
Antennas (2)	Peterson Instruments, 90-GHz scalar feed horn
Attenuator, 8 dB, coaxial	Mecca, Model 660-8-1
Circulator, 3-port	Alpha/TRG, Model W164
Detector diode	Aertech, Model D10
Dicke switch (latching circulator)	Electromagnetic Sciences, Inc., Model 409D-13
Gunn diode oscillator	Central Microwave Co., Model CMF1210AE
IF amplifier	Miteq, Model AM-3A-000110
Mixer/Preamplifier	Alpha/TRG, Model W9600
Mode Transition, TE_{10} rectangular to TE_{11} circular	Alpha/TRG, Model W884
Mode Transition, TE_{10} rectangular to TE_{11} circular	Baytron Co., Model 3R-69/C
Termination, waveguide	Baytron Co., Model 3R-50

Appendix C

Radiometric Beam-Separation Measurements

At White Mountain, we measured the orientations of the two antenna faces with a precision clinometer and used the resulting values to compute the opening angle between the axes of the antennas. After our return from White Mountain, the question arose as whether the antenna faces were truly perpendicular to the beam centers, so the opening angle was remeasured radiometrically in May 1984.

A 90.1-GHz microwave transmitter, consisting of a temperature-stabilized Gunn oscillator broadcasting through a corrugated horn antenna, was mounted on a raised portion of the roof of Building 50 at the Lawrence Berkeley Laboratory. The radiometer and its bearing mounts were removed from the cart and placed on a table approximately 2.5 meters below and 7.5 meters distant from the transmitter.

The 100-Hz oscillator that normally operated the Dicke switch was used to modulate the power transmitted by the Gunn oscillator and the Dicke switch was latched in one state. In this configuration, the radiometer was sensitive only to radiation whose power varied in phase with the 100-Hz oscillator, and the switch allowed only one of the two antennas to pass radiation on to the mixer. To further reduce the modulated signal entering the mixer by way of the second antenna, the antenna was covered by a layer of microwave absorber. An extra 8 dB of attenuation between the IF amplifier and the detector diode reduced the amount of noise power reaching the detector.

The antennas on the transmitter and the radiometer were aligned in altitude and azimuth until the radiometer response was maximized. The broadcast power was then increased to raise the voltage at the detector diode to approximately -13 mV (near the limit of the detector's linear range) and the gain setting of the lockin amplifier was adjusted to put the signal on scale.

The radiometer was then rotated in altitude through a series of zenith angles to map out the skirts of the gain pattern over a range from 5° to 11° on either side of the peak. The output voltage was measured at increments of approximately 1°, and a clinometer measured the orientation of a reference surface on the radiometer at each position.

When the measurements of the first antenna were completed, the Dicke switch was latched in its other setting and the procedure was repeated on the other antenna. Finally, the transmitter was turned off and the measurements were repeated once more to verify that the output voltage was position-independent.

To determine the beam center of an antenna, curves were fitted to the measurements of each skirt. The symmetry of the skirts was evaluated as a function of the point of reflection, and the reflection point giving rise to the greatest symmetry was chosen as the beam center. (Although the procedure was performed numerically, it is analogous to plotting the curves on tracing paper, folding the paper down the middle so that the curves overlap, and shifting the fold point until the curves are most nearly superimposed.) This procedure yielded the angles of both beam centers relative to the reference surface; the sum of the two angles was the opening angle.

Two measurements made in this way yielded beam separations of 59°.46 and 59°.47. Asymmetric structure in the response pattern of one antenna limited the accuracy of these measurements to ±0°.07 (4 arcminutes). The beam separation measured with the clinometer on the same date was 59°.50, consistent with the radiometric result. The uncertainty in the measured beam separation is therefore taken to be ±0°.07.

Acknowledgements

First and foremost, I would like to thank Valeria Evans for her unstinting support during the course of this project. Good times and bad, she's kept me going. I would also like to thank her for figures 3.5 and 5.1, which add a bit of class to the thesis if I do say so myself. While on the subject of families, let me also thank Valeria's family and mine, who provided encouragement and only rarely asked me if I was ever going to finish.

Many people from Berkeley and elsewhere have contributed to this project. George Smoot has guided me in my development as a scientist, both by his advice and by his example. He has played a major role in all phases of this project, from conception to completion. I also owe a lot to Scott Friedman, Giovanni De Amici, and Steve Levin for all the work they have done to make the project a success and for the companionship they have provided. Thanks as well to Jerry Epstein and Phil Lubin, for their various contributions and for the intellectual stimulation that they have both provided. Phil in particular has provided invaluable advice and assistance on the subject of 90 GHz radiometers and their component parts.

When a complicated piece of equipment has had to be designed and built, from scratch, by yesterday if not sooner, Hal Dougherty has come through time and again. Hal and Armi Meuti have also taught me the rudiments of machining technique, a useful set of skills when the inevitable crises occur. John Gibson never fails to amaze me with his electronic magic. Not only does John build circuits to perform incredible tasks, he actually makes them work. I thank John as well for all the time he spent with us at White Mountain keeping recalcitrant data-recording systems in working order. Jon Aymon has been a good friend and a great help over the years. Not only did he teach me most of what I know about programming, he valiantly stepped in when we were shorthanded at White Mountain. Robby Smits and John Taylor have made many useful suggestions about the design and construction of the cold load; their contributions are appreciated.

Linda Kelley, Bruce Grossan, Mark Griffith, Alan Benner, Lynne Deutsche, and Philip Melese have all lent their hands and minds to the experiment at one time or another. It is refreshing to observe the eager, energetic undergraduates approach research for the first time, and to see what cynics it makes of them.

Janice Gates, Nancy Gusack, and Faye Mitschang have managed to keep the office running even in the craziest of times. I thank them for their help.

Thanks to Reno Mandolesi, Bruce Partridge, and Giorgio Sironi, Gigi Danese, and Gianfranco De Zotti for their parts in the collaboration. Together, we have accomplished more than any of us could have done on our own.

A special thanks to the staff of the White Mountain Research Station for all the help and support—logistical, financial, and moral—that they provided. In particular, thanks to the crew for all the work they put in and for all the odd requests that they managed to satisfy somehow. If I have to be stuck somewhere at high altitude for weeks on end, make it the Barcroft Hilton.

Jack Welch, Mary Brunn, Tap Lum, Dave Williams, and numerous other people in the U. C. Berkeley Astronomy Department and the Radio Astronomy Laboratory have aided me both in my research project and in my educational progress. I appreciate the help that they have given me.

The Lawrence Berkeley Laboratory has provided our research group with numerous technical resources as well as financial support. Equally important to me is the unique opportunity it has given me to view of the way that physics on the cutting edge is done. Buford Price and the staff of the U. C. Berkeley Space Sciences Laboratory have provided financial and administrative support for this project throughout its development.

This thesis has been typeset with the TeX text-processing system. The availability of TeX at LBL is largely due to the work of Edgar Whipple, who installed, maintained, and lobbied for it on the Physics Division computer system. If it weren't for Edgar, I might have had to use UNIX TROFF, or worse yet, a typewriter.

Finally, I would like to express my appreciation for the pioneering work done in this field by Dave Wilkinson and his colleagues. They established a benchmark against which we could judge our work.

This work has been supported by the National Science Foundation, the Department of Energy, and the White Mountain Research Station of the University of California.

References

Alpher, R. A., Bethe, H., and Gamow G. 1948, *Phys. Rev.,* **73,** 803.

Alpher, R. A., and Herman, R. C. 1950, *Rev. Mod. Phys.,* **22,** 153.

Blair, A. G., Beery, J. G., Edeskuty, F., Hiebert, R. D., Shipley, J. P., and Williamson, K. D. 1971, *Phys. Rev. Letters,* **27,** 1154.

Boynton, P. E., Stokes, R. A., and Wilkinson, D. T. 1968, *Phys. Rev. Letters,* **21,** 462.

Boynton, P. E., and Stokes, R. A. 1974, *Nature,* **247,** 528.

Brandenberger, R. H. 1985, *Rev. Mod. Phys.,* **57,** 1.

Brickwedde, F. G., van Dijk, H., Durieux, M., Clement, J. R., and Logan, J. K. 1960, *Journal of Research of the National Bureau of Standards,* **64A,** 1.

Chan, K. L., and Jones, B. J. T. 1975, *Ap. J.,* **195,** 1.

Chan, K. L., and Jones, B. J. T. 1976, *Ap. J.,* **200,** 461.

Cole, A., Court, A., and Kantor, A. 1965, in *Handbook of Geophysics and Space Environment,* ed. S. L. Valley (New York: McGraw-Hill).

Corey, B. E. 1978, Ph. D. thesis, Princeton Univ.

Corey, B. E., and Wilkinson, D. T. 1976, *Bull. Am. Astron. Soc.,* **8,** 351.

Costales, J. B., Smoot, G. F., Witebsky, C., De Amici, G., and Friedman, S. D. 1985, *Radio Sci.,* submitted.

Danese, L., and De Zotti, G. 1978, *Astr. Ap.,* **68,** 157.

Danese, L., and De Zotti, G. 1980, *Astr. Ap.,* **84,** 364.

Danese, L., and De Zotti, G. 1982, *Astr. Ap.,* **107,** 39.

Davis, M., and Peebles, P. J. 1983, *Ann. Rev. Astr. Ap.,* **21,** 109.

De Amici, G., Smoot, G. F., Friedman, S. D., and Witebsky, C. 1985, *Ap. J.,* submitted.

De Amici, G., Witebsky, C., Smoot, G. F., and Friedman, S. D. 1984, *Phys. Rev. D,* **29**, 2673.

Dicke, R. H., Peebles, P. J., Roll, P. G., and Wilkinson, D. T., 1965, *Ap. J.,* **142**, 414.

Dolgov, A. D., and Zel'dovich, Ya. B. 1981, *Rev. Mod. Phys.,* **53**, 1.

Epstein, G. L. 1983, Ph. D. thesis, University of California, Berkeley. UCLBL Report 17118.

Ewing, M. S., Burke, B. F., and Staelin, D. H. 1967, *Phys. Rev. Letters,* **19**, 1251.

Field, G. B., and Hitchcock, J. L. 1966, *Phys. Rev. Letters,* **16**, 817.

Fixen, D. J., Cheng, E. S., and Wilkinson, D. T. 1983, *Phys. Rev. Letters,* **50**, 620.

Friedman, S. D. 1984, Ph. D. thesis, University of California, Berkeley. UCLBL Report 17279.

Friedman, S. D., Smoot, G. F., De Amici, G., and Witebsky, C. 1984, *Phys. Rev. D,* **29**, 2677.

Gamow, G. 1946, *Phys. Rev.,* **70**, 572.

Gamow, G. 1949, *Rev. Mod. Phys.,* **21**, 367.

Georgi, H., Ginsparg, P., and Glashow, S. L. 1983, *Nature,* **306**, 765.

Gorenstein, M. V., and Smoot, G. F. 1981, *Ap. J.,* **244**, 361.

Houck, J. R., and Harwit, M. O. 1969, *Ap. J. (Letters),* **157**, L45.

Howell, T. F., and Shakeshaft, J. R. 1966, *Nature,* **210**, 1318.

Howell, T. F., and Shakeshaft, J. R. 1967, *Nature,* **216**, 753.

Hoyle, F., and Tayler, R. J. 1964, *Nature,* **203**, 1108.

Hubble, E. P. 1925, *Annual Reports of the Mount Wilson Observatory, 1923-1924,* **48**, 139.

Hubble, E. P. 1929, *Proc. Nat. Acad. Sci.,* **15**, 168.

Illarionov, A. F., and Sunyaev, R. A. 1974, *Astron. Zh.,* **51**, 1162 (1975, *Soviet Astron.,* **18**, 691).

Jansen, M. A., Bednarczyk, S. M., Gulkis, S., Marlin, H., and Smoot, G. F. 1979, *IEEE Trans.,* **AP-27**, 551.

Jones, B. J. T. 1980, *Physica Scripta,* **21**, 732.

Kellner, J. 1957, *J. App. Phys.,* **28**, 426.

Kislyakov, A. G., Chernyshev, V. I., Lebskii, Yu. V., Mal'tsev, V. A., and Serov, N. V. 1971, *Astron. Zh.,* **48**, 39 (1971, *Sov. Astron.,* **15**, 29).

Kraus, J. D. 1966, *Radio Astronomy* (New York: McGraw-Hill).

Liebe 1981, *Radio Sci.,* **16**, 1183.

Liebe 1985, private communication.

Lightman, A. P. 1981, *Ap. J.,* **244,** 392.

Lorrain, P., and Corson, D. R. 1970, *Electromagnetic Fields and Waves* (San Francisco: Freeman) § 12.5.

Lubin, P., Epstein, G., and Smoot, G. 1983, *Phys. Rev. Letters,* **50,** 616.

Lubin, P., Melese, P., and Smoot, G. 1983, *Ap. J. (Letters),* **273,** L51.

Mandolesi, N., Calzolari, P., Cortiglioni, S., and Morigi, G. 1984, *Phys. Rev. D,* **29,** 2680.

McKellar, A. 1941, *Publ. Dominion Astrophys. Obs.,* **7,** 251.

Meyer, D. M., and Jura, M. 1984, *Ap. J. (Letters),* **276,** L1.

Meyer, D. M., and Jura, M. 1985, *Ap. J.,* in press.

Millea, M. F., McColl, M., Pederson, R. J., and Vernon, F. L. 1971, *Phys. Rev. Letters,* **26,** 919.

Muehlner, D., and Weiss, R. 1970, *Phys. Rev. Lett.,* **24,** 742.

Muehlner, D., and Weiss, R. 1973a, *Phys. Rev. D,* **7,** 326.

Muehlner, D., and Weiss, R. 1973b, *Phys. Rev. Letters,* **30,** 757.

Negroponte, J., Rowan-Robinson, M., and Silk, J. 1981, *Ap. J.,* **248,** 38.

Nyquist, H. 1928, *Phys. Rev.,* **32,** 113.

Otoshi, T. Y., and Stelzreid, C. T. 1975, *IEEE Trans.,* **IM-24,** 174.

Partridge 1980, *Physica Scripta,* **21,** 624.

Partridge, R. B., Cannon, J., Foster, R., Johnson, C., Rubinstein, E., and Rudolph, A. 1984, *Phys. Rev. D,* **29,** 2683.

Peebles, P. J. 1966, *Phys Rev. Letters,* **16,** 410.

Penzias, A. A., and Wilson, R. W. 1965, *Ap. J.,* **142,** 420.

Penzias, A. A., and Wilson, R. W. 1967, *A. J.,* **72,** 315.

Peterson, J. B., Richards, P. L., and Timusk, T. 1985, *Phys. Rev. Letters,* submitted.

Puzanov, V. I., Salomonovich, A. E., and Stankevich, K. S. 1967, *Astron. Zh.,* **44,** 1129 (1968, *Sov. Astron.* **11,** 905).

Rees, M. J. 1978, *Nature,* **275,** 35.

Roll, P. G., and Wilkinson, D. T. 1966, *Phys. Rev. Letters,* **16,** 405.

Shivanandan, K., Houck, J. R., and Harwit, M. O. 1968, *Phys. Rev. Letters,* **21,** 1460.

Silk, J., and Stebbins, A. 1983, *Ap. J.,* **269,** 1.

Sironi, G., Inzani, P., and Ferrari, A. *Phys. Rev. D,* 1984, **29,** 2686.

Smoot, G. 1980, *Physica Scripta,* **21,** 619.

Smoot, G. *et al.* 1983, *Phys. Rev. Letters,* **51,** 1099.

Smoot, G. *et al.* 1985, *Ap. J. (Letters),* **291,** L23.

Smoot, G., De Amici, G., Levin, S., and Witebsky, C. 1985, *Nuovo Cimento B, Proceedings of the Third Rome Meeting on Astrophysics* **87**, in press.

Smoot, G. F., Gorenstein, M. V., and Muller, R. A. 1978, *Phys. Rev. Letters,* **39,** 898.

Stecker, F. D., and Puget, J. L. 1972, *Ap. J.,* **178,** 57.

Stokes, R. A., Partridge, R. B., and Wilkinson, D. T. 1967, *Phys. Rev. Letters,* **19,** 1199.

Sunyaev, R. A., and Zel'dovich, Ya. B. 1970, *Ap. Space Sci.,* **7,** 20.

Sunyaev, R. A., and Zel'dovich, Ya. B. 1980, *Ann. Rev. Astr. Ap.,* **18,** 537.

Thaddeus, P. 1972, *Ann. Rev. Astr. Ap.,* **10,** 305.

Thaddeus, P., and Clauser, J. F. 1966, *Phys. Rev. Letters,* **16,** 819.

Ulaby, F., Moore, R., and Fung, A. 1981, *Microwave Remote Sensing,* Vol. **1,** *Microwave Remote Sensing Fundamentals and Radiometry* (Reading: Addison-Wesley).

Uson, J. M., and Wilkinson, D. T. 1984, *Ap J.,* **283,** 471.

Waters, R. B. 1976, in *Methods of Experimental Physics,* Vol. **12B,** *Radio Telescopes,* ed. M. L. Meeks (New York: Academic Press) pp. 142–176.

Weinberg, S. 1972, *Gravitation and Cosmology* (New York: Wiley).

Weinberg, S. 1977, *The First Three Minutes* (New York: Basic), § 4.

Weiss, R. 1980, *Ann. Rev. Astr. Ap.,* **18,** 489.

Welch 1984, private communication.

Welch, W. J., Keachie, S., Thornton, D. D., and Wrixon, G. 1967, *Phys. Rev. Letters,* **18,** 1068.

Wilkinson, D. T. 1967, *Phys. Rev. Letters,* **19,** 1195.

Woody, D. P., and Richards, P. L. 1979, *Phys. Rev. Letters,* **42,** 925.

Woody, D. P., and Richards, P. L. 1981, *Ap. J.,* **248,** 18.

Wright, E. L. 1982, *Ap. J.,* **255,** 401.

Zel'dovich, Ya. B., and Sunyaev, R. A. 1969, *Ap. Space Sci.,* **4,** 301.

Zel'dovich, Ya. B., Illarionov, A. F., and Sunyaev, R. A. 1972, *Zh. E. T. F.*, **62,** 1217 (*Soviet Phys. JETP,* **35**, 643).